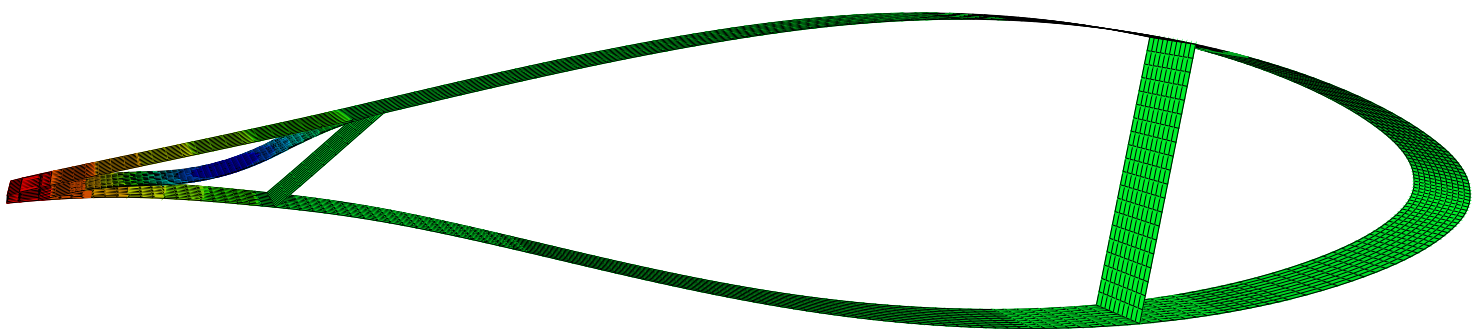


Design of a blade section featuring passive load alleviation capabilities resulting from variable stiffness morphing structures

WITH A FOCUS ON LARGE, MODERN WIND TURBINES.

Wolf D.K. Cavens

May 19th 2015



**Design of a blade section featuring passive load
alleviation capabilities resulting from variable
stiffness morphing structures**
With a focus on large, modern wind turbines.

MASTER OF SCIENCE THESIS

For obtaining the degree of Master of Science in Engineering Wind
Energy at Technical University of Denmark and in Aerospace
Engineering at Delft University of Technology.

Wolf D.K. Cavens

May 19th 2015

European Wind Energy Master - EWEM
DUWIND - Delft University of Technology
Risø - Denmark Technical University



Risø DTU



Copyright © Wolf D.K. Cavens
All rights reserved.

EUROPEAN WIND ENERGY MASTER - EWEM
OF
ROTOR DESIGN TRACK

The undersigned hereby certify that they have read and recommend to the European Wind Energy Master - EWEM for acceptance a thesis entitled “**Design of a blade section featuring passive load alleviation capabilities resulting from variable stiffness morphing structures**” by **Wolf D.K. Cavens** in partial fulfillment of the requirements for the degree of **Master of Science**.

Dated: May 19th 2015

Supervisor:

Dr. Andres Arrieta of ETH Zürich

Supervisor:

Dr. Néstor Ramos García of DTU

Supervisor:

Dr. Ir. Roeland de Breuker of TU Delft

Reader:

Prof. Dr. Gerard J.W. van Bussel of TU Delft

Summary

The main objective of this MSc thesis project is to investigate the load alleviation potential of a variable stiffness bi-stable morphing blade section under extreme gust conditions by designing such a blade section.

This project builds on the work of Arrieta et al. [1] and Kuder et al. [2] and is based on the DU 93-W-210 airfoil. The bi-stable element design by Kuder et al. [2] was carried over.

The aerodynamic codes XFOIL, Q³UIC and RFOIL were compared and validated with wind tunnel data and more advanced Computational Fluid Dynamics results. The aeroelastic Abaqus model by Kuder et al. [2] was modified in order to accommodate for this project.

The effects of an extreme operating gust were studied and quantified. Especially at cutout conditions, the impact of a gust was found to be profound. Furthermore, dynamic stall effects during a gust were found to be significant at high angle of attack. It was demonstrated with a parametric study that trailing edge flaps can alleviate a significant amount of the load increase due to a gust.

A morphing trailing edge mechanism was presented. This mechanism consists of a morphing trailing edge flap which is restrained from rotation by a bi-stable plate. Upon reaching a critical flap hinge moment, the bi-stable snaps from the stiff to the flexible state which allows the trailing edge flap to morph passively and hence alleviate load. The flap hinge moment behaviour of small flaps was found desirable for passive morphing and originates from boundary layer separation. A locally compressible profile skin was found to be required in order to achieve load alleviation. Therefore, a corrugated skin was implemented on the suction side of the profile near the trailing edge.

Two morphing blade sections were presented, one with a large flap (20.59% chord) and one with a small flap (13.19% chord). The effectiveness of the bi-stable restraining mechanism was demonstrated. The small and large flap exhibit relatively similar amounts of load alleviation which indicates that the small flap is more efficient. The instantaneous lift reduction is around 7% at rated conditions and 17% at cutout conditions. This means that trailing edge flaps are less effective at high angle of attack in separated flow conditions. However, the amount of alleviated load increases after snap-through with increasing wind speed.

Finally, the dynamic response of an instantaneously morphing flap was addressed.

It can be concluded that passive load alleviation was achieved. One of the critical elements for this load alleviation was the implementation of a corrugated skin.

It is deemed that the presented designs can be optimised further to achieve even more load

alleviation. However, this study indicates that there is a potential for a morphing passive load alleviation mechanism which reduces the impact of extreme gusts and potentially allows for a reduction in blade mass which in turn can induce a reduction in wind energy cost.

Acknowledgements

I wish to thank the following persons;

My supervisors Dr. Arrieta, Dr. García and Dr. Ir. de Breuker for their guidance and support. Dr. Arrieta in special for giving me the opportunity to work as a visiting student at ETH Zürich.

Dr. Garcia in special for letting me use the aerodynamic codes Q³UIC and Q³UIC_AERO.

Izabela Kuder for the aeroelastic model and her advice regarding Python scripting for Abaqus.

Dr. Grasso from ECN for supplying a copy of the aerodynamic code RFOIL.

Ir. Timmer for providing valuable and unpublished airfoil data for DU airfoils.

Iva Hrogovan for the conformal airfoil mapping tool although it did not use it in the end.

Finally, I would like to thank the IDEA League for the financial support.

Delft, The Netherlands
May 19th 2015

Wolf D.K. Cavens

Contents

Summary	v
Acknowledgements	vii
List of Figures	xi
List of Tables	xiii
Acronyms	xv
1 Introduction	1
Nomenclature	1
2 Literature review	3
2.1 Motivation	3
2.2 Morphing airfoils	3
2.2.1 Active morphing airfoils	4
2.2.2 Passive morphing airfoils	5
2.3 Morphing airfoils with multi-stable elements	5
2.3.1 Active morphing airfoils with multi-stable elements	6
2.3.2 Passive morphing airfoils with multi-stable elements	7
2.4 Analysis and Conclusion	8
3 Project plan	11
3.1 Research question, aims and objectives	11
3.2 Approach	14
4 Selection of reference airfoil	17
4.1 Requirements	17
4.2 Reference airfoil	18

5	Validation of XFOIL, Q3UIC and RFOIL	21
5.1	Pressure distributions	21
5.2	Lift and drag polars	23
5.2.1	Comparison with wind tunnel data	23
5.2.2	Comparison with CFD results	26
5.3	Justification	27
6	Aeroelastic model	29
6.1	Working procedure	29
6.1.1	Bi-stable plate script	30
6.1.2	XFOIL script	30
6.1.3	Aeroelastic script	30
6.2	Validation	31
6.3	Modifications	31
6.3.1	Bi-stable plate script modifications	31
6.3.2	XFOIL script modifications	31
6.3.3	Aeroelastic script modifications	32
7	Conditions for load alleviation	33
7.1	Reference wind turbine	33
7.2	Extreme operating gust	34
7.3	Blade Element Momentum method	36
7.4	Viscosity, compressibility and roughness effects	38
7.5	Flow conditions and loads	40
8	Parametric morphing study	45
8.1	Assumptions and constraints	45
8.2	Morphing mechanism	46
8.3	Parametric study	49
8.4	Dynamic stall	52
8.5	Control mechanism	56
9	Design of morphing airfoil	59
9.1	Bi-stable element	59
9.2	Corrugated composite laminates	61
9.2.1	Substitute stiffness matrix	61
9.2.2	Implementation	65
9.2.3	Design considerations	67
9.3	Morphing potential study	68
9.3.1	Design restrictions and approach	69
9.3.2	Final morphing flap designs	69
9.3.3	Steady response of morphing flap	70
9.3.4	Unsteady response of morphing flap	81

10 Conclusion	83
11 Recommendations	87
References	89
A Reference airfoil coordinates	95

List of Figures

2.1	Conflicting requirements for morphing structures. [3]	4
2.2	Concepts with bi-stable elements.	6
2.3	Helicopter rotor blade airfoil concept with morphing trailing edge. [4]	7
2.4	Prototype compliant airfoil with bi-stable elements in test rig.	8
2.5	Results presented by Kuder et al. [2].	9
4.1	Reference airfoil and corresponding airfoil series.	18
5.1	Pressure distributions of clean DU 93-W-210 airfoil.	23
5.2	Pressure distributions of DU 93-W-210 airfoil with zigzag tape at suction side.	24
5.3	XFOIL and Q ³ UIC and RFOIL lift and drag of DU 93-W-210 airfoil.	25
5.4	Effect of Reynolds number on performance of DU 93-W-210 airfoil. [5, p. 4]	26
5.5	CFD lift and drag of DU 93-W-210 airfoil. [6, p. 58]	27
6.1	Aeroelastic model diagram.	29
7.1	Illustration of the Siemens SWT-6.0-154 reference wind turbine. [7, p. 7]	34
7.2	EOG wind speed history.	36
7.3	Velocities at the rotor plane. [8, Lecture 'Control']	36
7.4	Local loads on a blade section. [8, Lecture 2]	38
7.5	Weighted average of wind tunnel lift and drag of DU 93-W-210 airfoil.	40
7.6	Extreme operating gust AOA history.	42
7.7	Loads generation during an EOG of a blade tip section for various conditions.	43
7.8	Loads generation of a blade tip section for various conditions.	43
8.1	Wind turbine blade cross section. [9, p. 5]	46
8.2	Simplified morphing mechanism.	48

8.3	Morphing mechanism FBDs.	49
8.4	Normalised flap hinge moment coefficient for various flaps.	49
8.5	Flap hinge moment in function of relative velocity and AOA.	49
8.6	Reference airfoil with various trailing edge flaps.	50
8.7	Lift and drag coefficient correction factors	51
8.8	Effect of flaps on lift and drag polars.	51
8.9	Effect of TE flap on loads generation of a blade tip section.	52
8.10	Dynamic stall. [10, p. 63]	53
8.11	Static lift coefficient and separation function	54
8.12	Dynamic lift coefficient.	55
8.13	Loads generation during an EOG of a blade tip section for various conditions. . .	56
9.1	Bi-stable plate designs by Kuder et al. [2, p. 3]	60
9.2	Corrugated composite skin test specimen. [11, p. 119]	61
9.3	Unit cell definition. [11, p. 10-11]	63
9.4	Axis system for corrugation according to Winkler. [11, p. 13]	66
9.5	Segmented skin by Thill et al. [12, p. 6]	68
9.6	Small flap design.	70
9.7	Large flap design.	70
9.8	Small flap before and after snap-through.	71
9.9	Large flap before and after snap-through.	72
9.10	Small flap deflection.	72
9.11	Large flap deflection.	73
9.12	Pressure distributions of morphed airfoils.	73
9.13	Overlay of morphed and undeformed airfoil with large flap.	75
9.14	Overlay of morphed and undeformed airfoil with small flap.	75
9.15	Trailing edge displacement in function of velocity.	78
9.16	Approximate flap angle in function of velocity.	78
9.17	Lift coefficient in function of velocity.	79
9.18	Drag coefficient in function of velocity.	79
9.19	Simplified representation of trailing edge deflection.	80
9.20	Buckling of bi-stable element due to TE geometry and stiffness.	80
9.21	Lift response of morphing flap.	81

List of Tables

7.1	Parameters from the Siemens SWT-6.0-154 reference wind turbine.	34
7.2	Local Reynolds and Mach numbers for various cases from BEM calculations (rounded values).	39
7.3	Flow conditions with and without EOG (rounded values).	42
7.4	Change in flow conditions and loads as a result of an EOG (rounded values). . .	42
8.1	Normalised flap hinge moment for various flaps and flow conditions.	50
8.2	Effect of flaps on lift and drag coefficients in gust conditions.	52
8.3	Effect of flaps on the normal force and torque generated by a blade section in gust conditions.	52
8.4	Change in loads as a result of an EOG (rounded values).	56
9.1	Geometric parameters of bi-stable plate designs. [2, p. 3]	60
9.2	Laminate properties.	65
9.3	Layup of airfoil skin.	65
9.4	Corrugation compression test results.	67
9.5	Morphing flap properties.	70
9.6	Morphing velocity.	71
9.7	Effect of morphing flaps on lift and drag coefficients and corrugation in gust conditions.	74
9.8	Trailing edge deflection as a result of velocity change.	76
9.9	Lift coefficient change before and during snap-through. (rounded values)	77
A.1	DU-93-W-210 airfoil coordinates.	96

Acronyms

AOA	Angle of attack
BEM	Blade Element Momentum
CFD	Computational Fluid Dynamics
CTLP	Classical theory of laminated plates
EOG	Extreme operating gust
FBD	Free body diagram
FEA	Finite element analysis
MFC	Macro-fibre composite
PZT	Piezoelectric
SMA	Shape memory alloy
TRL	Technology readiness level

Chapter 1

Introduction

Nowadays, one of the main drivers behind the research and development of wind turbines is energy cost reduction in order to make wind energy more competitive amongst other methods of energy production. This has driven the exorbitant increase in wind turbine size as higher wind speeds, and thus power generation potential, come at greater heights.

However, this increase in wind turbine size and especially in blade size has resulted in more loads and thus stresses. This increase in size and loads comes with an increasing need for load control in order to protect the structure from damage and control the power output.

Research has demonstrated that there is a considerable potential in load control by (locally) changing the blade profile. Currently, there are a lot of developments in the field of so-called smart rotors. A control systems monitors certain parameters and when necessary, activates some sort of actuator to adjust the blades of these rotors in order to reduce loads, load fluctuations or control power output.

Morphing structures show great promise for smart rotor concepts due to their adaptive shape, load bearing capability and aerodynamic efficiency and hence why there is a lot of ongoing research in this area.

However, besides actively controlled morphing concepts, there exist passively controlled morphing concepts for load alleviation on wind turbine blades. Though, these concepts are far less studied compared to their active variant. Passive morphing presents some potential benefits compared to active morphing such as the lack of power loss due to control systems and actuators as well as reduced weight, complexity and cost.

Among the various morphing concepts, this research focuses on passive morphing through the use of variable stiffness bi-stable composites. This morphing concept is relatively new and pioneered by Arrieta et al. [1] and Kuder et al. [2] and presents some opportunities for the alleviation of the loads associated with rare, extreme atmospheric conditions such as gusts.

It has been demonstrated by Arrieta et al. [1] and Kuder et al. [2] that it is possible to incorporate bi-stable, variable stiffness composite elements in a selectively compliant airfoil to allow passive morphing. As it is proven for the airfoil stiffness to change by incorporating variable stiffness bi-stable elements, one of the remaining challenges in the design of a blade section with passive load alleviation capabilities is the morphing to a specific shape which generates a lower aerodynamic resultant.

This research project focuses on the implementation of these bi-stable, variable stiffness com-

posite elements in a wind turbine specific, selectively compliant airfoil. The morphing into a shape that is aerodynamically less favourable for lift generation is of particular interest. Finally, some optimized airfoil designs with integrated bi-stable elements are presented. The morphing processes is analysed as well as the load alleviation that comes with the morphed airfoil. The outcomes of this research project could then be used as a basis for the design of a morphing wind turbine blade which features passive load alleviation through the use of bi-stable composite elements.

First the literature review is considered in Chapter 2 in order to get a firm understanding of research in the field of morphing airfoils in general and of the work on which this project builds in specific.

In Chapter 3 the project planning is addressed. Starting from the research question, the research objective and work packages for the project are defined. The literature review actually compromises the first two tasks that are defined in this Chapter.

In Chapter 4, requirements for a reference airfoil are outlined after which the selected reference airfoil and a corresponding airfoil series are introduced.

Chapter 5 introduces the aerodynamic code XFOIL [13] and its potential alternatives Q³UIC [14] and RFOIL [15]. XFOIL, Q³UIC and RFOIL results for the reference airfoil are compared with wind tunnel test data and more advanced Computational Fluid Dynamics code results for validation and justification purposes.

The working procedure of the aeroelastic model by Kuder et al. [2] as well as the modifications to this model in the scope of this study are outlined in Chapter 6.

The flow conditions and aerodynamic loads associated with an extreme operating gust are determined in Chapter 7.

In Chapter 8, a simplified morphing trailing edge mechanism is presented. The potential of a passive morphing mechanism is addressed. Furthermore, the potential effect of trailing edge flaps on blade loads during an extreme operating gust is examined by means of a parametric study.

The design of the airfoil section which passively alleviates load through morphing with the use of variable stiffness bi-stable elements is treated in Chapter 9. Corrugated composite laminates are introduced in this chapter as well.

Chapter 10 summarizes the main findings of this study.

Some recommendations for future research in the field of this study are presented in Chapter 11.

Literature review

2.1 Motivation

As described in Chapter 3 in more detail, the objective of this MSc thesis project is to investigate the potential of passive load alleviation under extreme, rare atmospheric conditions on wind turbine blades through the use of variable stiffness bi-stable composites by designing an airfoil representable for modern wind turbine blades that features passive load alleviation capabilities by selective compliance morphing through the use of the aforementioned bi-stable elements.

In order to get a firm understanding of the research in the field of morphing airfoils in general and of the morphing concept on which this project builds in specific, this literature review is carried out.

A narrow-down, funnel approach is adopted. First, the broad research field of morphing airfoils is considered in Section 2.2. This field is divided in actively controlled (Section 2.2.1) and passively controlled (Section 2.2.2) morphing airfoils. In Section 2.3, the more specific research field of morphing airfoils which use multi-stable elements is considered. Again, this field is divided in actively controlled (Section 2.3.1) and passively controlled (Section 2.3.2) variants. Special attention is addressed to the passive load alleviation concept as presented by Arrieta et al. [1] and Kuder et al. [2] since the project builds on this concept.

One of the main challenges for the proposed research is to obtain passive load alleviation through a reduction in aerodynamic lift as a result of morphing. Therefore, this literature review mainly focuses on the aerodynamic aspects of morphing airfoil concepts. However, when deemed to be relevant, structural and actuation aspects are treated in order to accumulate potential strategies and best-practices, identify pitfalls and find useful methodology.

2.2 Morphing airfoils

Compliant mechanisms are, according to Lachenal et al. [16], monolithic structures that rely on elastic deformation for the transmission of motion and/or force, they can be considered as mechanisms without joints nor hinges.

According to Schultz and Hyer [17], morphing structures are structures that change shape

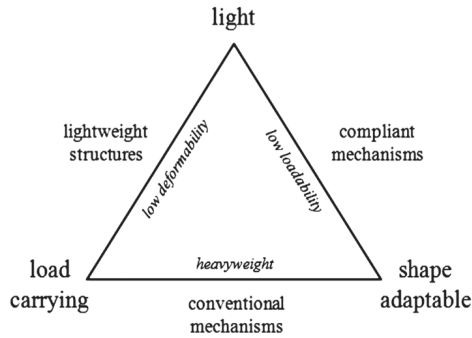


Figure 2.1: *Conflicting requirements for morphing structures. [3]*

or state in order to change their operating characteristics or as a response to changes in the environment.

Lachenal et al. [16] identified one of the main issues associated with morphing structures as the apparent contradiction in the requirements for these structures; they should be stiff in order to carry load, however, their structure should be compliant in order to keep actuator forces low. This is illustrated by the diagram in Figure 2.1.

Barbarino et al. [18] stated that originating from the conflicting requirements for morphing structures, several flexible skin types such as composite corrugated panels, elastomeric matrix composites and morphing core sandwich composites have been developed. These skins are soft to allow for shape changes whilst still being stiff enough to carry aerodynamic loads.

Thill et al. [19] reviewed morphing concepts for aircraft with a focus on morphing skins and identified the biggest current design problem to be the combination of stiffness and flexibility into one structure. It was concluded that anisotropic and variable stiffness structures offer the potential to combine compliance and stiffness. However, it was noted that the level of maturity of morphing skins is low.

2.2.1 Active morphing airfoils

Most of the research in the field of morphing focusses on active morphing, this means that the morphing is controlled by a system with actuators of some sort. However, according to Barbarino et al. [18], many of the developed concepts still have a very low Technology Readiness Level (TRL) and have weight penalties associated with the morphing capabilities due to a lack of integrated design and the presence of a control system with actuators.

Additionally to a compliant structure, actuators are required to enforce the shape deformation in order to obtain an actively morphing structure. Various actuator types such as shape memory alloys (SMA, Barbarino et al. [20]), electromagnetic actuators (Daynes et al. [21]), electromechanical actuators (Kota et al. [22]), piezoelectric actuators (PZT, Bilgen et al. [23]) and macro-fibre composite actuators (MFC, Arrieta et al. [24]) exist and are currently subject to research.

Barbarino et al. [18] stated that airfoil morphing and camber morphing in specific is the dominant research topic for subsonic aerodynamic applications when compared to other morphing methods such as planform and out-of-plane morphing. Camber morphing can be achieved locally by means of leading or trailing edge flaps, however, it can also be accomplished globally along the entire chord of the airfoil.

Barbarino et al. [20] used SMAs to actuate a morphing trailing edge of an aircraft wing. This

morphing trailing edge introduced a gradual camber change towards the trailing edge resulting in a higher aerodynamic efficiency compared to a trailing edge flap which introduces a sudden camber change.

Kota et al. [22] presented a FlexSys variable geometry adaptive compliant trailing edge flap for endurance aircraft. Prototype wind tunnel testing revealed the benefit in terms of drag reduction of this morphing concept compared to conventional trailing edge flaps.

Very recently, NASA [25] tested an adaptive compliant trailing edge (ACTE) flap. An airplane's conventional aluminium flaps were replaced with advanced shape-changing assemblies that form seamless bendable surfaces which deflect up to 20 degrees.

Raither et al. [26] used electro-bonded laminates (EBL) to obtain skins with variable stiffness and presented a concept for a camber morphing airfoil which enabled a reduction in actuation energy of up to 97% due to the variable stiffness skin which proves the potential of variable stiffness structures.

According to Lachenal et al. [16], research in the wind turbine community in the field of morphing airfoils focuses mainly on trailing edge flaps because of their potentially high aerodynamic efficiency, simple construction and low weight.

Wiratama [27] investigated the potential of active trailing edge flaps as a means of enhancing energy capture capabilities and concluded that they offer a significant potential for increased energy production when wind turbine blades are considered.

Andersen [28] made a similar conclusion and stated that the load alleviation potential of varying trailing edge geometry on wind turbine blades is substantial.

Castaignet et al. [29] demonstrated the load alleviation capability of a small active trailing edge flaps with a full-scale test on a Vestas V27 wind turbine by achieving an average flapwise blade root load reduction of 14%.

2.2.2 Passive morphing airfoils

Bottasso et al. [30] developed a wind turbine blade with passive bend-twist-to-feather coupling by exploiting the orthotropic properties of composite materials to mitigate loads induced by wind fluctuations. In combination with active individual pitch control this passive-active concept showed significant potential for load reductions while limiting actuator duty cycle.

Lambie [31] investigated a wind turbine airfoil with self-adaptive camber for load alleviation. The actuation of the trailing edge flap was done passively via a kinematic coupling with the leading edge flap.

Selig et al. [32] presented a morphing segmented wind turbine blade concept which features passive pitch control. However, this concept is deemed to be less relevant for the proposed research since it is only applicable to downstream turbines.

These concepts illustrate the potential of passive control systems as an alternative for actively controlled systems.

2.3 Morphing airfoils with multi-stable elements

According to Schultz and Hyer. [17], bi-stable or multi-stable structures are good candidates to be used as morphing structures because of their ability to remain in natural equilibrium after a shape change occurs.

Sections 2.3.1 and 2.3.2 discuss the presented concepts in more detail as they are deemed to be more relevant for the proposed research.

2.3.1 Active morphing airfoils with multi-stable elements

Diaconu et al. [33] explored three morphing airfoil concepts which used bi-stable elements in order to identify composite lay-ups and geometries that offer multiple stable states. They made use of thin-walled carbon fibre composites with a non-symmetric lay-up as bi-stable elements. Bi-stability in these composites was achieved by inducing residual stresses through thermal curing. Analysis was carried out with non linear finite element structural analysis in Abaqus [34]. No experimental tests were conducted in order to validate the simulation. Simple load cases were used to investigate the bi-stable behaviour of the morphing airfoil concepts. Aerodynamic loading was not considered.

The first concept is an airfoil with a flap-like morphing trailing edge, see Figure 2.2a. The most aft part of the trailing edge consists of bi-stable plates. These plates are connected through a rubber connector to allow for relative movement of the upper and lower panels. Snapping or snap-through is the rapid change of one stable state to the other. Snapping occurs when a critical vertical actuation load is applied at the middle of the trailing edge. A total flap rotation of around 10° is achieved, however, it is expected that the loading capability might be smaller compared to a typical airfoil. Hence the link with Figure 2.1 on page 4 on the conflicting requirements regarding compliance and load carrying capability.

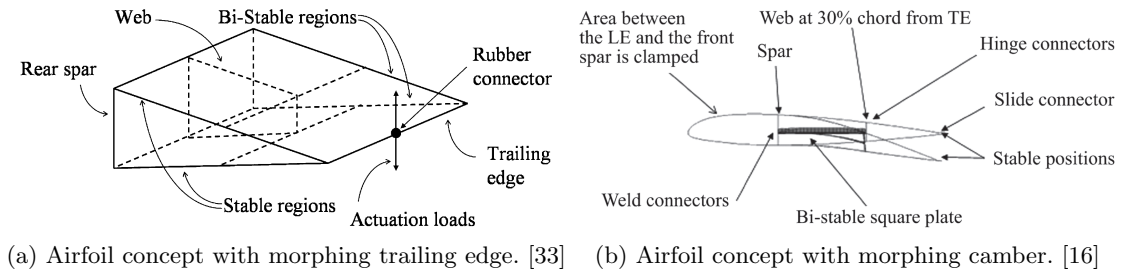


Figure 2.2: Concepts with bi-stable elements.

The second concept by Diaconu et al. [33] is an airfoil with morphing camber, see Figure 2.2b. A square bi-stable plate is positioned horizontally in the airfoil along its chord. The forward edge of the bi-stable plate is considered to be clamped to the front spar. The aft edge of the bi-stable plate is hinged to a vertical web. This web is hinged to the airfoil surfaces to allow for relative movement of the airfoil skins under actuation. The airfoil surface is discontinuous at the trailing edge in order to allow for the skins to slide over each other when changing between stable states. When the bi-stable plate is actuated, it snaps from one stable state to the other, altering camber and morphing the airfoil. Snap-through can also be enforced by enforcing a critical vertical displacement at the trailing edge. Again, it is unsure whether this concept features sufficient load carrying capability.

A third concept by Diaconu et al. [33], an airfoil with morphing chord was also studied, however, it was found to be less relevant for the proposed research and is not treated in this literature review.

Daynes et al. [21] presented an airfoil with an active morphing trailing edge for a helicopter rotor blade which proved the possibility of using bi-stable composites as aerodynamic surfaces, see Figure 2.3. This concept with a relatively high TRL, comprises multiple bi-stable square elements which are positioned horizontally in the trailing edge. Upon activation of an electromagnetic actuator, this concept can rapidly deflect the trailing edge by 10° . Hence the advantage of the bi-stable elements is that the actuator is only needed to change the state

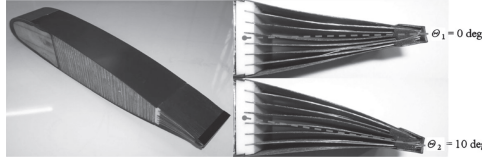


Figure 2.3: Helicopter rotor blade airfoil concept with morphing trailing edge. [4]

of the bi-stable elements and thus energy consumption is minimized. Full scale wind tunnel experiments showed a significant change in lift coefficient as well as load carrying ability of at speeds up to 60 m/s.

Bilgen et al. [23] presented an active morphing wing which used bi-stable elements and surface bonded piezoelectric actuators. Wind tunnel tests showed the stiffness was sufficient to carry aerodynamic loads passively in both stable states, i.e. without the contribution of actuators. Furthermore, a resonating control strategy that achieved dynamic forward and reverse snap-through was presented.

From the presented concepts it is apparent that active airfoil morphing by using bi-stable composites is feasible and presents some potential benefits.

Diaconu et al. [33] noted that the bi-stability properties of these concepts are highly affected by temperature and moisture absorption. Bi-stability properties increase with decreasing temperature. However, these properties diminish with moisture absorption and they can even be lost in case of extremely high temperatures. Achieving bi-stability through pre-stressing during manufacturing could mitigate these problems related to environmental factors.

2.3.2 Passive morphing airfoils with multi-stable elements

Arrieta et al. [1] presented a concept for passive aerodynamic load alleviation on an airfoil level. The novel concept makes use of variable stiffness bi-stable composite elements. These composite elements exhibit stiffness variability arising from the different properties associated with each equilibrium configuration. The airfoil structure is selectively compliant to allow for morphing. In the stiff state, the airfoil is assumed to be rigid. Upon reaching a critical load, the bi-stable elements snap-through and change from the stiff state to the flexible state. This state is called flexible because of its reduced stiffness, hence the structure exhibits variable stiffness. The structure is tailored for snap-through to occur at a set, critical load associated with rare, extreme atmospheric conditions. This passive change in stiffness allows the compliant structure to morph and potentially, alleviate load. Morphing can be allocated to the reduced structural stiffness in combination with the relatively high aerodynamic loading on the airfoil which forces the airfoil to morph into a shape which ideally is less favourable for lift generation. Hence aerodynamic load can be passively alleviated through morphing due to the sudden change in structural stiffness origination from the snap-through of the integrated bi-stable elements.

It must be noted that morphing in the concept by Arrieta et al. [1] occurs upon reaching a limiting load and serves as an extreme case safety feature as opposed to most active load alleviation concepts where the aim is to reduce load fluctuations and hence the system operates continuously.

The research was continued and Kuder et al. [2] carried out a parametric study to optimise the positioning of these bi-stable elements within a symmetric NACA (National Advisory Committee for Aeronautics) 0012 airfoil. An experimentally validated model that made use of Python [35] scripting and the commercial Abaqus Finite Element Analysis (FEA) code was

used for this optimisation process. Following from the parametric study, a prototype configuration with two bi-stable elements was selected and manufactured see Figure 2.4. This prototype was tested on a test rig to validate the numerical predictions of the structural stiffness response. The experimental results showed a stiffness ratio between the stiff and flexible mode of 2.47:1, hence stiffness variability was achieved. Furthermore, the numerical predictions showed good agreement with the experimental results, thereby validating the numerical procedure.

Next, a weak aeroelastic coupling was integrated in the model with the aid of the open-source XFOIL airfoil aerodynamics code. An iterative process involving XFOIL and Abaqus calculated the airfoil deformation and the associated pressure distributions until specified convergence criteria (change in trailing edge deflection for one iteration) were met. Upon convergence, the morphed airfoil shape and its corresponding pressure distributions and aerodynamic coefficients were presented. See Figure 2.5a for the consecutive deformation stages of the prototype airfoil as modelled for an aerodynamic pressure corresponding to 35 m/s and an angle of attack (AOA) of 8° . First the most forward bi-stable element snaps-through, see Figure 2.5a(a) Hereafter, the second bi-stable elements buckles (no snap-through), see Figure 2.5a(b) and Figure 2.5a(c).

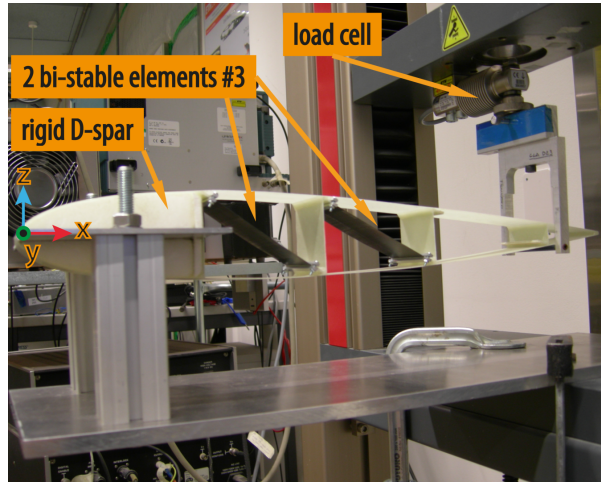


Figure 2.4: Prototype compliant airfoil with bi-stable elements in test rig.

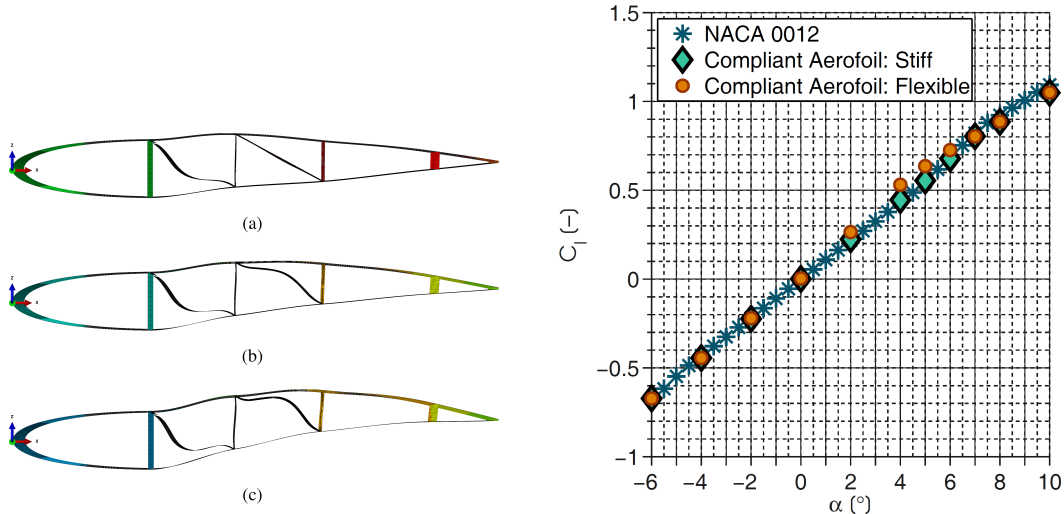
Kuder et al. [2] concluded that stiffness variability and passive airfoil morphing were achieved. Furthermore, the modelling procedure was validated. However, the lift curve for the compliant airfoil did not depict the anticipated reduction in lift, see Figure 2.5b, and hence aerodynamic load alleviation was not achieved.

2.4 Analysis and Conclusion

The topic of morphing was introduced and a selection of work from various morphing categories was reviewed. It has been pointed out that these fields of research are extremely broad and diverse and that currently a lot of options are considered on a conceptual level. The potential of morphing in terms of load control and alleviation was clearly identified. However, it was also found that the majority of the presented concepts has a low TRL.

The research presented in this Chapter has been selected and presented with the proposed research in mind. For example, the variable stiffness camber morphing concept by Raither et al. [26] shows similarities with the concept presented by Arrieta et al. [1].

Based on the presented work, bi-stable elements were found to present a well balanced solution



(a) Consecutive deformation stages of the prototype (b) Comparison of lift coefficients of the compliant airfoil in the stiff mode. (c) Comparison of lift coefficients of the compliant prototype airfoil. [2]

Figure 2.5: Results presented by Kuder et al. [2].

for morphing applications because of their combination of light weight, load carrying potential and shape adaptability.

The research builds upon the work of Arrieta et al. [1] and Kuder et al. [2] and is carried out under supervision of Dr. Arrieta.

It can be concluded that Arrieta et al. [1] and Kuder et al. [2] successfully integrated variable stiffness bi-stable components in a selectively compliant airfoil that features stiffness variability which in turn allows for passive morphing. However, in the final paragraph of the previous Section, it was identified that aerodynamic load alleviation was not achieved. Hence the critical point of the concept was identified as the aerodynamic efficiency in terms of lift reduction through shape adaptation.

Hence the next logical step in order to identify the load alleviation potential of this concept is the development of an airfoil that features, additionally to stiffness variability through integration of bi-stable elements, passive load alleviation capabilities through a reduction in the lift coefficient as a result of morphing. This airfoil design is wind turbine-oriented and therefore it is expected that some strategies and concepts by others, especially in the field of shape adaptation, might be adopted in the design of this airfoil.

Chapter 3

Project plan

This Chapter presents the MSc thesis project and the associated planning in more detail. It serves as an important guideline and backbone over the course of the project.

3.1 Research question, aims and objectives

From the work presented in Chapter 2, it is clear that a lot of research has been carried out and is going on in the field of morphing airfoils.

However, as stated before, passive load alleviation through morphing by utilising bi-stable variable stiffness composite elements is relatively new and is currently pioneered by Arrieta et al. [1] and Kuder et al. [2] at the Swiss Federal Institute of Technology Zürich (ETHZ). The research builds upon the work of Arrieta et al. and is partially conducted at ETHZ at the Compliant Systems Group. Dr. Arrieta is Team Leader of this Group and is one of the supervisors of the MSc thesis project together with Dr. García from the Denmark Technical University (DTU) and Dr. Ir. de Breuker from the Delft University of Technology (TU Delft).

As mentioned in Section 2.4, the innovation and exercise of this research project lies in implementing this novel morphing technique on wind turbine airfoils in order to obtain passive aerodynamic load alleviation.

This results in the following research question for this MSc thesis project;

How can variable stiffness bi-stable composites be exploited to passively alleviate aerodynamic loads induced by rare, extreme atmospheric conditions on wind turbine blades by selective compliance morphing airfoils?

The main research objective can then be defined as follows;

Investigate the potential of passive load alleviation under extreme, rare atmospheric conditions on wind turbine blades through the use of variable stiffness bi-stable composites by designing a

blade section representable for modern wind turbine blades that features passive load alleviation capabilities by selective compliance morphing through the use of the aforementioned bi-stable elements.

Under the important assumption that the codes and models developed by Arrieta et al. [1] and Kuder et al. [2] are largely carried over, this objective can be reached by answering the following questions;

- What research has been carried out so far?
 - What research has been done at the Compliant Structures Group at ETHZ?
 - What research has been done by others if a broader research field is considered?
- Which airfoil can be used as a reference airfoil?
 - Is this airfoil representable for modern wind turbine blades?
 - Is this airfoil part of an airfoil group with various thicknesses?
- How do aerodynamics codes perform when the reference airfoil is considered?
 - How accurate are the models and in which flow conditions?
 - Can they be validated with experimental results?
- Is the aeroelastic model developed by Arrieta et al. [1] and Kuder et al. [2] suitable for the proposed research?
 - Why or why not?
 - Are some extensions required? Which?
- When should load alleviation on a wind turbine blade, ideally, occur?
 - Under which aerodynamic conditions such as wind speed, AOA and Reynolds number?
 - How much load should be alleviated?
- How should the selected airfoil ideally morph in order to passively alleviate load?
 - Under which, reasoned, constraints?
 - How can this morphing be specified in terms of tip deflection, camber change etc?
- Is there a type of morphing that is achievable through the use of bi-stable elements that approximates (one of) the defined ideal morphing state(s)?
- How should the bi-stable elements be integrated on an airfoil level in order to approximate this morphing behaviour when subject to the specified aerodynamic conditions?
 - Which type of bi-stable elements should be used?
 - Where should these elements be located and how should they be integrated?
- What is the load alleviation potential for this technology?

- Under which conditions and for which, idealised, design?
- What would be the possible impact on blade loads when this technology would be integrated in a modern wind turbine?
- What dynamic effects can be expected in extreme load cases and during morphing?
- Which additional considerations need to be addressed in further research?

The research question presented above can then be distilled into the following tasks;

1. Study and gain understanding of the work done to-date by Arrieta et al. at ETHZ
2. Study literature to get an insight of the work done in the fields of morphing airfoils and load alleviation on airfoils
3. Select a reference airfoil which is representable for modern wind turbines
4. Familiarize with aerodynamics codes and validate them for the reference airfoil
5. Familiarize with Abaqus
6. Familiarize with the aeroelastic tool developed by Arrieta et al. [1] and Kuder et al. [2] and modify if required
7. Determine aerodynamic conditions at which morphing should occur
8. Establish ideal type of morphing for the reference airfoil, under certain reasoned constraints
9. Investigate what type of morphing, closest to ideal, is achievable
10. Design a blade section with internal structure that exhibits the desired load alleviation through morphing at specified atmospheric conditions
11. Assess the load alleviation potential of the morphing blade section design by comparing with a non-adaptive blade section
12. Address the most dominant dynamic effects and assess their impact
13. Document and present results and make recommendations for further research

It must be noted that no experimental testing is planned to be conducted for validation of the Abaqus code, however, some experimental tests were carried out by Kuder et al. [2] and are considered in Section 2.3.2 and 6.2.

This research is anticipated to contribute towards the possible implementation of this novel passive load alleviation technique on wind turbine blades. The expected impact of the implementation of this morphing concept is a reduction in material stresses and increased structural life. Possibly, turbines designed with this morphing blades have higher average annual energy production since the blades can be up-scaled because the weight penalties associated with rare, extreme load cases are reduced. This in turn might result in a reduction in wind energy cost and hence a reduction in green electricity price making it more competitive with grey electricity and making it more appealing to the general public.

3.2 Approach

As mentioned before, the concept on which the research builds has been developed by Arrieta et al. [1] and Kuder et al. [2]

The characteristics of variable stiffness bi-stable elements are exploited in the design of a compliant airfoil with a selective deformation mode which allows the airfoil to passively morph into a lower lift generating shape.

Special attention is given to the notion that wind turbine airfoils often operate with rough, 'dirty' blades due to accumulated dirt, dust and insects on the blade surface. The adoption of a 'weighted approach' as presented by Zhu et al. [36] is considered.

It must be mentioned that whenever possible, models developed by Arrieta et al. [1] and Kuder et al. [2] are carried over. If modifications are required, these are carried out after a discussion with the creator of the model.

The design of the proposed morphing airfoil is done with use of the 2D airfoil aerodynamics open-source code XFOIL and the commercial FEA code Abaqus.

XFOIL models the pressure distribution over a given profile for specified aerodynamic conditions and requires inputs such as AOA, Reynolds number, Mach number and optionally, boundary layer transition points for the pressure and suction side of the profile. Furthermore, the airfoil profile needs to be specified by means of 2D coordinates. XFOIL results consist of lift, drag and pressure distribution data for each specified case.

Abaqus models deformations and stresses of structures under load and requires a meshed airfoil structure with specified material properties, this includes the integrated bi-stable elements. A load case can be specified by interpolating the pressure distribution from XFOIL onto the profile. Abaqus results include deformations and material stresses.

Now the aeroelastic tool is considered for a specified compliant airfoil with integrated bi-stable elements. First, XFOIL calculates the pressure distribution of the airfoil. Hereafter, XFOIL results are post processed and fed into Abaqus. Kuder et al. [2] used Python scripting for this post processing step. This processed aerodynamic data is fed into Abaqus together with the meshed airfoil geometry with specific material properties and dimensions, including the bi-stable elements. Abaqus simulates and then outputs stresses and deformations of the modelled airfoil. The deformed shape is then fed back to XFOIL in order to determine the aerodynamic pressure distribution of the deformed profile. This new pressure distribution is then again fed back into Abaqus. This iterative process continues until a defined convergence criterion (trailing edge vertical displacement per iterative step) is reached. At this point, the flow around the morphed airfoil is assumed to be quasi-stable and the airfoil is assumed not to deform any more under the specified aerodynamic conditions. In a final XFOIL run, the lift and drag curves as well as the pressure distributions for the morphed airfoil are calculated.

Now the aerodynamic data of the morphed airfoil can be compared with the initial, non-deformed airfoil to assess the amount of alleviated load. A Blade Element Momentum (BEM) method [37] approach in MATLAB [38] is used to analyse and compare the loading on a wind turbine blade section with a morphing airfoil with a conventional airfoil.

The XFOIL code is validated for the reference airfoil by comparing the results with experimental wind tunnel data. As mentioned earlier, the Abaqus model is not validated in the scope of this project, however, Kuder et al. [2] compared the results of this model with experimental test data.

The final and most relevant outcomes are the reductions in aerodynamic resultant (mainly lift) of the morphed airfoil compared to the non-adaptive airfoil. These aerodynamic resultants can then be translated towards loads for a wind turbine blade. Ultimately, the goal is to reduce the

blade loading in extreme cases, this can be addressed by comparing the loads generated by the individual blade sections.

This is relevant since a reduction in these loads allows for a lighter structure and/or up scaling of the wind turbine blade which in turn could decrease the cost of wind energy.

Selection of reference airfoil

In order to determine the load alleviation potential of this novel morphing method, the morphing section which is designed should be representable for modern wind turbine blades as stated in the research objective in Section 3.1. Therefore the design of this morphing section is based on an existing airfoil, which is addressed as the reference airfoil. In order to select an appropriate reference airfoil, some requirements are specified in Section 4.1. The selected reference airfoil is presented in Section 4.2.

4.1 Requirements

Please note that the reference airfoil is chosen to be located in the mid-span to outboard blade sections since the largest load alleviation potential is anticipated in the more outboard sections. This because the more outboard sections of the blade cover more rotor area and hence generate more power compared to the inboard blade sections. Also, the more outboard sections have a large contribution to the blade root bending moment since they have a large moment arm and hence are a large contributor to critical loads originating from gusts.

Bergami [39] acknowledged this statement and simulated adaptive trailing edge flaps for active load alleviation on the NREL 5 MW virtual wind turbine on the outer sections the blades, from 77% till 97% span. Through the use of these flaps, a blade root flapwise lifetime fatigue damage equivalent load reduction of 15% was predicted.

Furthermore, Wolff at al. [40] designed an optimal deformable trailing edge for an outboard wind turbine blade airfoil of 18% thickness (thickness over chord, t/c) for active load control. In 2004, Van Rooij and Timmer [41, slide 6] stated that the thickness of an airfoil in the outboard sections is between 15% and 18% and that the airfoil thickness in the mid span sections is around 25%.

These references support the selected approach and give an indication of typical airfoil thicknesses.

The requirements for the reference airfoil can be stated as follows;

1. The airfoil is representable for modern wind turbine blades

2. The airfoil has a thickness between 15% and 25% (mid-span to outboard blade sections)
3. The airfoil is part of a series with various thicknesses
4. The airfoil is relatively insensitive to roughness since wind turbine blades often operate in foiled conditions
5. The airfoil profile is publicly available, the corresponding airfoil series preferably as well
6. The airfoil profile is specified numerically with a satisfactory refinement for aerodynamic simulations
7. High quality wind tunnel test data of the airfoil is available for validation purposes

4.2 Reference airfoil

The DU (Delft University) 93-W-210 airfoil, see Figure 4.1a, was chosen as reference airfoil since it fulfils all requirements stated in the previous Section, see the list on the next page. The first two numbers after DU stand for the year in which the airfoil was designed, the following two stand for the thickness of the airfoil in percentage of the chord. The airfoil features a blunt trailing edge since it is difficult to manufacture a sharp trailing edge and thus it is beneficial to use an airfoil with optimised performance for a blunt trailing edge. The airfoil coordinates are given in Appendix A.

Please note that no trade-off has been performed and hence possibly other airfoils also comply with the presented requirements. It is was not the goal to select the airfoil best suited for morphing since the goal is to determine the load alleviation potential by means of a reference airfoil which can be found in current blade designs. This implies that the morphing method should not only work for the selected reference airfoil, but for a variety of airfoils. Ideally, the morphing method is applicable to a wide range of airfoils from various airfoil series.

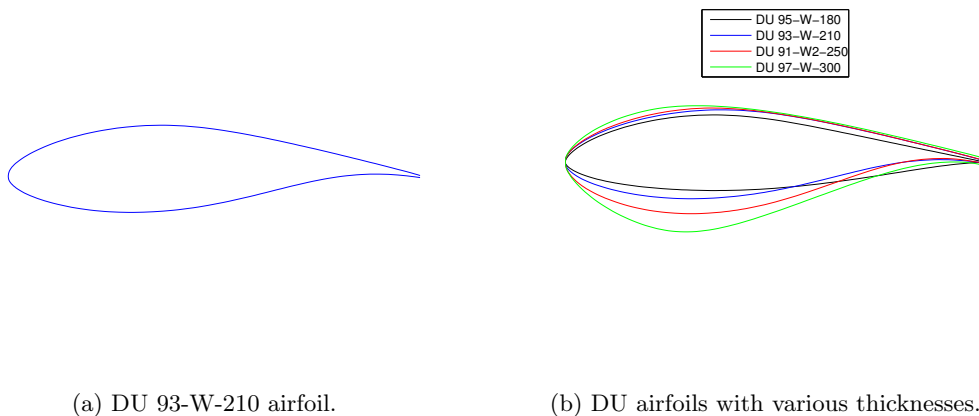


Figure 4.1: Reference airfoil and corresponding airfoil series.

The selected reference airfoil complies with the requirements stated in the previous Section since;

1. DU airfoils are widely used in modern wind turbine blades, by Siemens Wind Power, REpower and Suzlon for example [41, slide 30]. Furthermore, the reference airfoil is used in the NREL 5 MW virtual wind turbine [42]
2. The reference airfoil thickness is 21% (explanation in the next paragraph)
3. The corresponding airfoil series comprises profiles in thicknesses of 18% up to 30%, see Figure 4.1b
4. The primary design driver of the reference airfoil and corresponding airfoil series was low sensitivity to roughness according to van Rooij and Timmer [5, p. 11]
5. The reference airfoil and corresponding airfoil series are publicly available
6. The reference airfoil and corresponding airfoil series profiles are specified by 200 non-uniformly distributed 2D points
7. Experimental wind tunnel data of the reference airfoil and corresponding airfoil series was kindly provided by Ir. Timmer from TU Delft

More recent DU airfoils such as the DU 00-W-212 [41, slide 30] (21% thickness) and DU 08-W-180-6.5 [43] (18% thickness) also exist. However, these airfoils are not public (DU 08) or the associated wind tunnel test data is not public (DU 00). Wolff et al. [40] conducted a study to design an optimal deformable trailing edge for the latter more recent DU airfoil. Similarly, Troldborg [44] presented an optimised design for a deformable trailing edge for the Risø-B1-18 (18% thickness) wind turbine airfoil. This work is used as reference material when Task 8 as described in Section 3.1 is addressed.

From the presented references, the obvious choice would be to select an outboard wind turbine airfoil with a thickness of about 18%. However, a 21% profile was chosen to anticipate on the predicted trend of increasing airfoil thicknesses, also in outboard sections, for large wind turbine blades (such as the 10-20 MW offshore wind turbine design INNWIND.EU project) as stated by Grasso and Ceyhan [43]. This choice is justified further in Chapter 6 of the recently published DTU International Energy Report 2014 where Madsen et al. [45, p. 35] state the following;

"A key element in the new rotor design philosophy is the use of new high lift and relative thicker airfoils that allows for the design of more slender rotor blades, as illustrated in Figure 9. The power producing lift force is proportional to the blade width, also called the chord length of the airfoils, and the lift coefficient. If the lift coefficient is increased by designing new airfoils or adding vortex generators to existing airfoils for delayed flow separation (stall), then the chord length can be reduced by the same fraction without compromising the total lift force. The absolute thickness of the blade must however remain the same to be able to carry the same lift force, thus these new airfoils must have a higher relative thickness."

It must be noted that it is expected that the morphing strategy is slightly different for every airfoil series. Furthermore, it is expected that a particular benefit of the selected airfoil series is the aft-loading as a result of the 'S-tail' which is present in the profiles as stated by van Rooij and Timmer [41, slide 9]. Hence it is anticipated that variable trailing edge geometry has more influence on the overall lift on DU airfoils compared to less aft-loaded airfoils. Hence the efficiency of for example a deformable trailing edge for load alleviation is expected to be larger for DU airfoils compared to less aft-loaded airfoils.

Validation of XFOIL, Q³UIC and RFOIL

As mentioned earlier, Kuder et al. [2] made use of XFOIL to determine the airfoil aerodynamic performance. However, it was decided to compare multiple 2D aerodynamic codes. Q³UIC and RFOIL were found to be potential alternatives for XFOIL and are considered in this Chapter. Q³UIC is a 2D or quasi-3D unsteady viscous–inviscid interactive code developed at DTU by Dr. García and is not open-source nor freely available such as XFOIL. Dr. García kindly provided a student version of Q³UIC which could be used for this project under certain conditions.

According to Timmer and van Rooij [5, p. 11], RFOIL is a modified version of XFOIL. The modifications were done in order to ameliorate lift predictions around stall and to include the effects of rotation. Furthermore, RFOIL was used to design thick inboard DU airfoils. Dr. Grasso from the Energy research Centre of the Netherlands (ECN) kindly provided a free, limited version of RFOIL which could be used for this project under certain conditions.

In order to reduce the number of figures and provide an easy comparison, plots in this Chapter include XFOIL as well as Q³UIC and RFOIL results.

The coordinates from the reference airfoil were preprocessed with MATLAB in order to create files suitable as inputs for XFOIL, Q³UIC and RFOIL.

According to the wind tunnel data which was kindly provided by Ir. Nando W.A. Timmer [46], the reference airfoil measurements were obtained in the Low-Speed Low-Turbulence (LST) Wind Tunnel at the Faculty of Aerospace Engineering of TU Delft with a model with a chord of 0.60 m. Measurements for a clean profile and a profile with a zigzag tape at 5% chord on the suction side were performed at a Reynolds number of 3.0e6 and a Mach number of 0.22. Llorente et al. [47] state that the LST Wind Tunnel has a turbulence intensity level of 0.07% at 75 m/s which corresponds to the Mach number at which the measurements were obtained, therefore a turbulence intensity level of 0.07%, a Mach number of 0.2 and a Reynolds number of 3.0e6 are used for the XFOIL, Q³UIC and RFOIL calculations in this Chapter.

5.1 Pressure distributions

In this Section, the pressure distributions from XFOIL, Q³UIC and RFOIL are compared with the experimental pressure distributions from wind tunnel tests.

Figure 5.1 on page 23 displays the pressure distributions of the reference airfoil as calculated

by XFOIL, Q³UIC and RFOIL for a clean profile. The pressure distribution of the reference airfoil in the wind tunnel is plotted in black.

Figure 5.2 on page 24 displays the pressure distributions of the reference airfoil as calculated by XFOIL, Q³UIC and RFOIL for a profile with forced boundary layer transition at 5% chord on the suction side of the profile. No pressure distribution wind tunnel data was available for a profile with forced transition. Hence the pressure distribution from the clean profile in the wind tunnel is plotted again as a reference.

In the wind tunnel the boundary layer was tripped with a 0.39 mm thick zigzag tape. This boundary layer tripping simulates the effect of roughness on the airfoil surface and hence gives an indication of the airfoil performance in foiled conditions. In XFOIL, Q³UIC and RFOIL this boundary layer tripping was specified by forcing boundary layer transition at 5% chord on the suction side of the profile.

Four cases were considered; a low lift case (0° AOA), a near operating point case (4° AOA), a near stall case (8° AOA) and a post stall case (12° AOA).

The pressure distributions for the low lift case can be seen in Figure 5.1a and 5.2a. There is only a minor difference between the clean and tripped case for both XFOIL, Q³UIC and RFOIL. XFOIL and RFOIL display a sudden drop in local negative pressure coefficient at around 50% chord. According to Katz [48, p. 496-497] this is due to a laminar separation bubble. This laminar separation bubble occurs since the laminar flow is not able to follow the airfoil's suction side. If the Reynolds number is sufficiently high, the boundary layer reattaches aft of the laminar separation bubble and the boundary layer becomes turbulent. The sharp drop of the negative pressure coefficient occurs behind the bubble. Furthermore, XFOIL and RFOIL show slightly more loading near the trailing edge. Although, overall, the results for XFOIL, Q³UIC and RFOIL are very similar.

The pressure distributions for the near operating point case can be seen in Figure 5.1b and 5.2b. Please note that the wind tunnel pressure distribution is for a slightly larger AOA of 4.12°. Here, there is a clear difference in lift between the clean and tripped case for both XFOIL, Q³UIC and RFOIL. Again, XFOIL and RFOIL display a more distinct laminar separation bubble and more loading near the trailing edge. Also, a slight pressure peak can be observed in the XFOIL and RFOIL results near the leading edge. The results for XFOIL, Q³UIC and RFOIL show very good agreement.

The pressure distributions for the near stall case can be seen in Figure 5.1c and 5.2c. Please note that the results for the clean profile are for an AOA of 8.1°, this is due to Q³UIC which does not give full control over the AOA. Furthermore, the AOA of the wind tunnel data is slightly higher at 8.22°. Contrary to the XFOIL and RFOIL results, there is a clear reduction in lift between the clean and tripped case for Q³UIC results. Furthermore, Q³UIC predicts slightly more lift on the first half of the chord compared to XFOIL and RFOIL. The results for XFOIL, Q³UIC and RFOIL show relatively good agreement.

The pressure distributions for the post stall case can be seen in Figure 5.1d and 5.2d. Please note that the results for the clean profile are for an AOA of 12.025°. Again, the AOA of the wind tunnel data is slightly higher at 12.21°. In this case, there is a significant difference between the wind tunnel results and those of the models. All codes roughly over predict lift on the forward half of the chord and under predict lift on the aft half of the profile. There is little difference between the clean and tripped case for XFOIL, Q³UIC and RFOIL results. This is since boundary layer transition occurs naturally at high AOA and hence the impact of forced boundary layer transition is minimal. It can be observed that RFOIL results match the wind tunnel results best. However, the results for XFOIL and Q³UIC still show relatively good agreement.

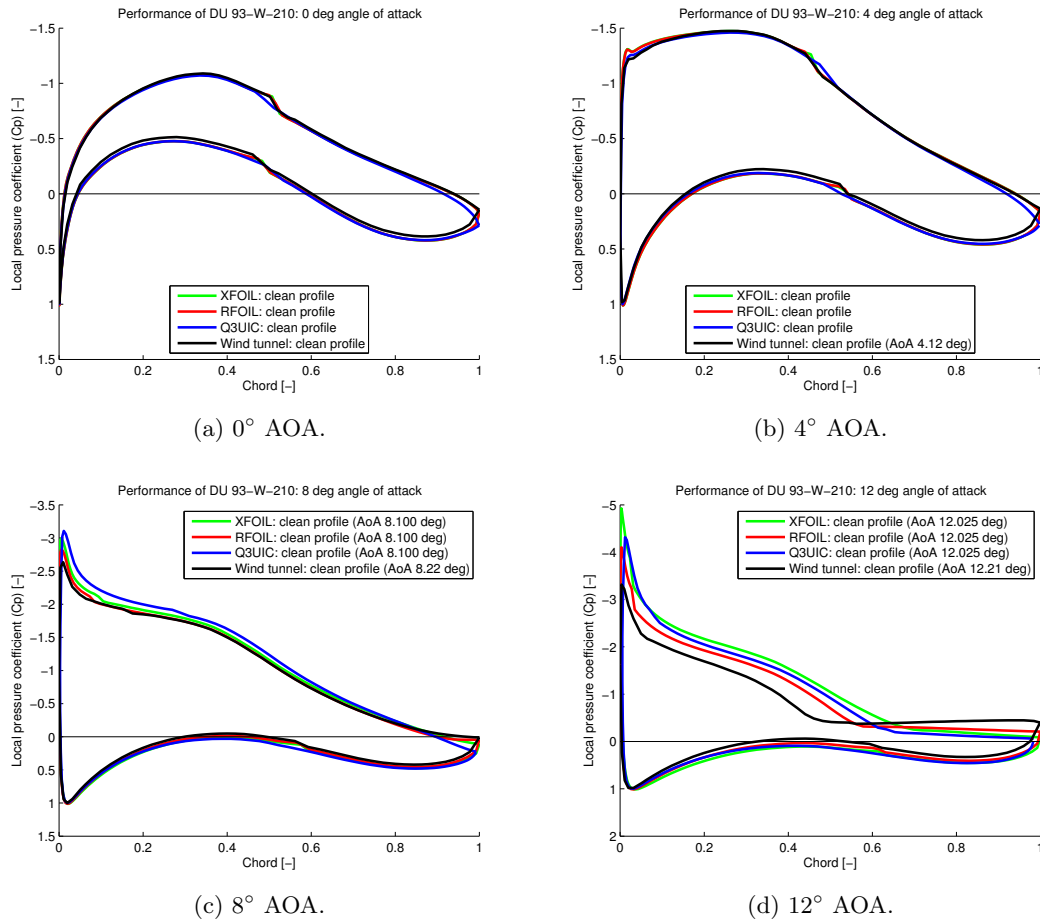


Figure 5.1: Pressure distributions of clean DU 93-W-210 airfoil.

5.2 Lift and drag polars

In this Section, the lift and drag polars from XFOIL, Q³UIC and RFOIL are compared with experimental polars from wind tunnel tests as well as with polars from more advanced Computational Fluid Dynamics (CFD) codes.

5.2.1 Comparison with wind tunnel data

Figure 5.3 on page 25 displays the lift and drag of the reference airfoil as calculated by XFOIL, Q³UIC and RFOIL. Wind tunnel data is again plotted in black whereas the dotted lines represent the difference of XFOIL, Q³UIC and RFOIL relative to the wind tunnel data. This wind tunnel data was obtained with slightly different settings for the measurement software compared to the data for the pressure distributions, however, the deviation in lift and drag compared to the other data amounts to less than 1% according to Ir. Timmer. Again, the clean profile as well as the profile with zigzag tape is considered. Please note that the ranges of AOA were different for the wind tunnel data of the clean profile compared to the profile with zigzag tape. Hence, the ranges of AOA for XFOIL, Q³UIC and RFOIL have been adapted to the wind tunnel data. The lift curve for the clean profile can be seen in Figure 5.3a. In the pre stall

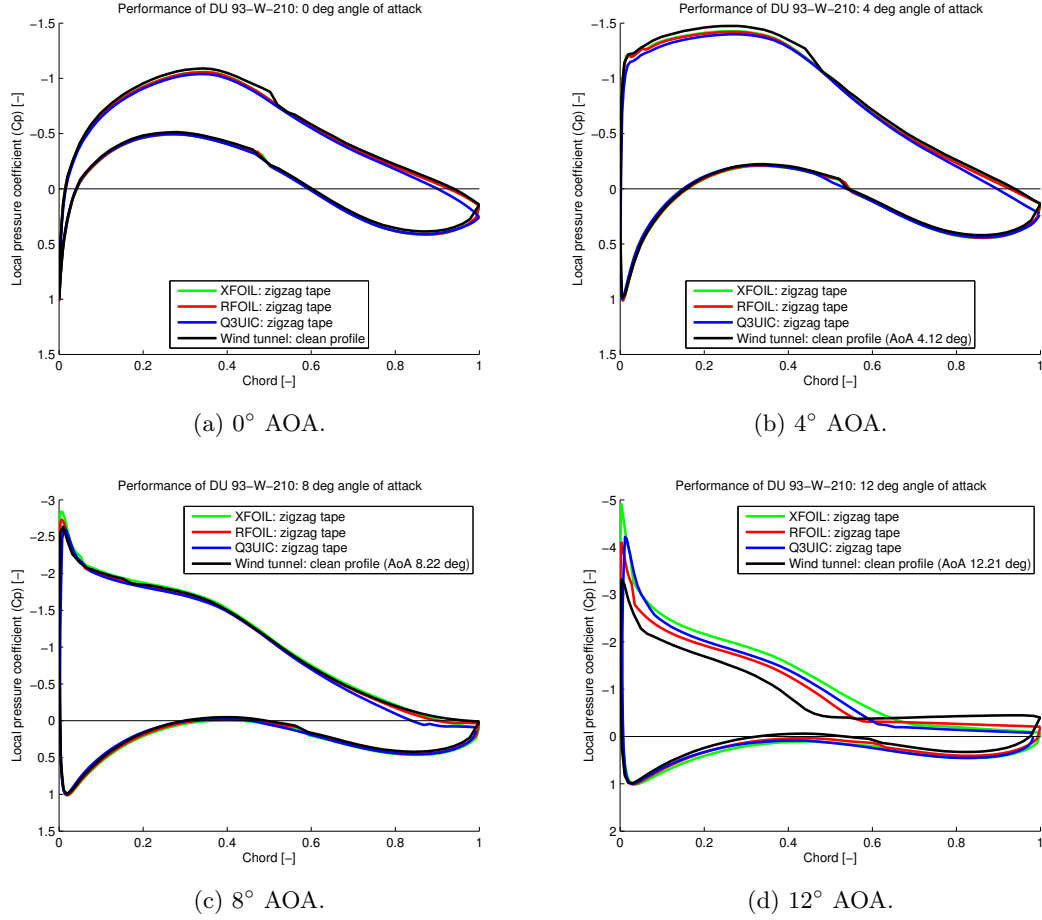


Figure 5.2: Pressure distributions of DU 93-W-210 airfoil with zigzag tape at suction side.

region, all codes show very good agreement with the wind tunnel data. However, the deviation of Q³UIC and RFOIL from the wind tunnel data is slightly smaller compared to XFOIL. Also in the near stall and post stall region, Q³UIC and RFOIL show better agreement with the wind tunnel data compared to XFOIL. However, all codes over predict lift after stall.

The drag curve for the clean profile can be seen in Figure 5.3b. In the pre stall region, all codes show very good agreement with the wind tunnel data. In the near stall and post stall region, RFOIL shows better agreement with the wind tunnel data compared to XFOIL and Q³UIC. At AOA above 15°, Q³UIC performs better compared to XFOIL. All codes under predict drag in the near stall and post stall region.

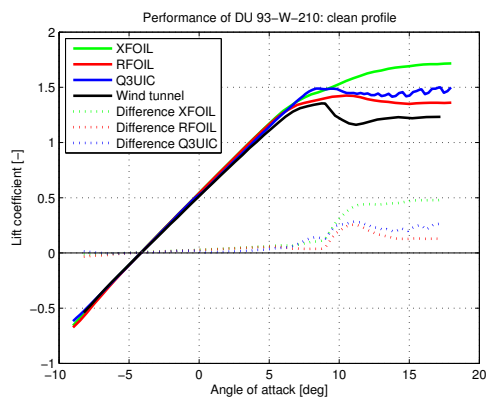
The lift curve for the profile with zigzag tape can be seen in Figure 5.3c. In the pre stall region, all codes show good agreement with the wind tunnel data. Q³UIC performs best in this region. Also in the near stall and post stall region, Q³UIC shows better agreement with the wind tunnel data compared to XFOIL and RFOIL. Again, all codes over predict lift after stall.

The drag curve for the profile with zigzag tape can be seen in Figure 5.3d. RFOIL shows relatively good agreement with the wind tunnel data. XFOIL performs better compared to Q³UIC since it shows slightly better agreement with the wind tunnel data. All codes under predict drag across the entire range of AOA.

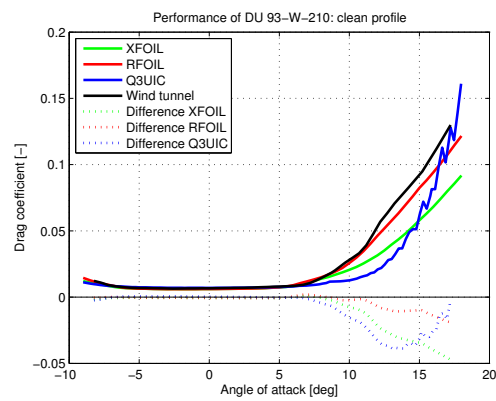
In general, one can conclude that RFOIL shows best agreement with the wind tunnel data compared to XFOIL and Q³UIC for both lift and drag.

When lift is considered, one can conclude that Q³UIC generally tends to give better results compared to XFOIL. However, lift is over predicted for the profile with zigzag tape and in the region near and after stall by all codes.

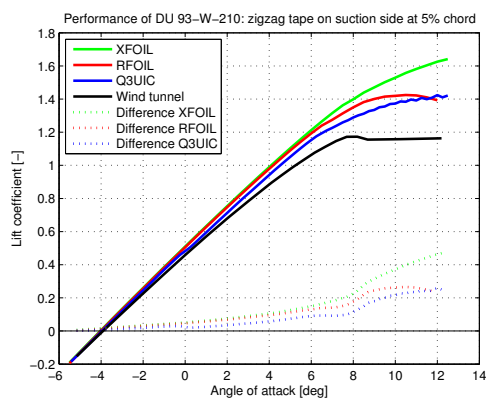
When drag is considered, XFOIL has the tendency to perform better compared to Q³UIC. However, drag is generally under predicted by all codes.



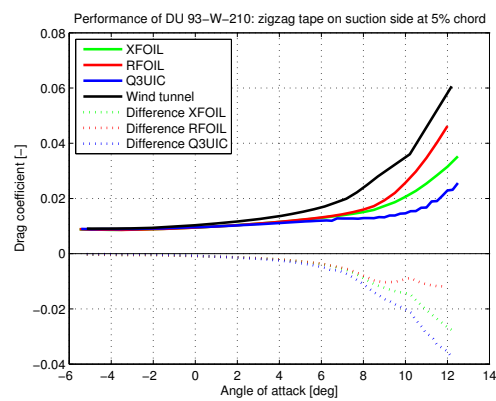
(a) Lift of clean profile.



(b) Drag of clean profile.



(c) Lift of profile with zigzag tape on suction side at 5% chord.



(d) Drag of profile with zigzag tape on suction side at 5% chord.

Figure 5.3: XFOIL and Q³UIC and RFOIL lift and drag of DU 93-W-210 airfoil.

5.2.2 Comparison with CFD results

Bertagnolio et al. [6] presented CFD results for the reference airfoil (clean profile DU 93-W-210) and compared them with wind tunnel test data from 1993 from the LST Wind Tunnel at TU Delft, see Figure 5.5 on page 27. Please note that in this case the Reynolds number is $1.0e6$. Based on variable Reynolds number wind tunnel tests by Timmer and van Rooij [5, p. 4], see Figure 5.4 on page 26, it is anticipated that at a Reynolds number of $1.0e6$ the maximum lift coefficient is slightly higher and the maximum lift over drag ratio is significantly lower compared to a Reynolds number of $3.0e6$. For the profile with forced boundary layer transition by means of a zigzag tape, the influence of Reynolds number in this range was found to be negligible. The CFD codes are the two-dimensional Navier-Stokes solver EllipSys2D and the three-dimensional version EllipSys3D. Bertagnolio et al. [6] investigated the Influence of three-dimensional transition models. Influence of turbulence modelling in the form of Reynolds-Averaged Navier-Stokes (RANS) equations and of Detached Eddy Simulation (DES) model was studied as well. The presented results serve as an indication of what is possible with more advanced CFD codes and serve as a comparison to the solvers XFOIL, Q³UIC and RFOIL presented earlier in this Chapter.

When lift is considered, see Figure 5.5a, it is apparent that the CFD results are not better compared to those of XFOIL, Q³UIC and RFOIL when the pre stall region is considered. In this region, the lift is generally under predicted by CFD. In the stall and post stall region, lift is over predicted by CFD, albeit to a lesser extent compared to XFOIL, Q³UIC and RFOIL. When drag is considered, see Figure 5.5b, it is apparent the the CFD results are significantly better compared to those of XFOIL, Q³UIC and RFOIL across the entire range of AOA and show very good agreement with the wind tunnel data.

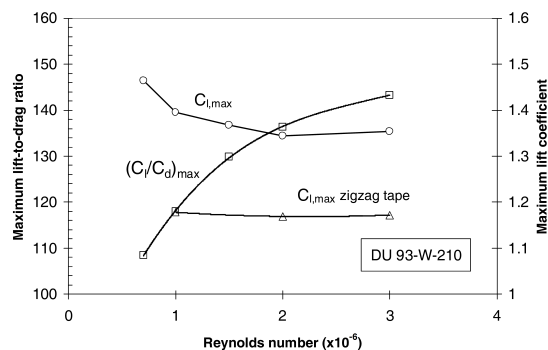


Figure 5.4: Effect of Reynolds number on performance of DU 93-W-210 airfoil. [5, p. 4]

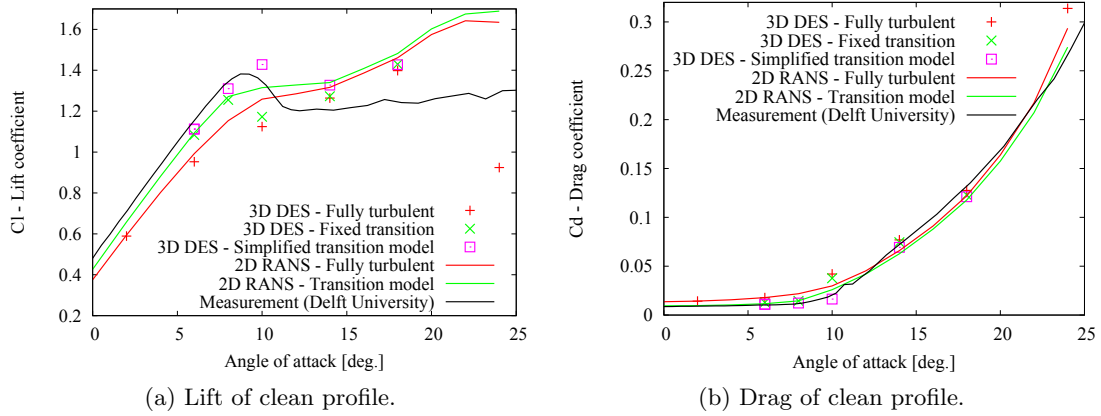


Figure 5.5: CFD lift and drag of DU 93-W-210 airfoil. [6, p. 58]

5.3 Justification

Based on the presented results and the conclusions made earlier, it is deemed to be justified to use either of the codes XFOIL, Q³UIC or RFOIL for the aerodynamic calculations of this project. This because the most dominant load on the blade is lift. Drag has only a small contribution to the resultant force. Hence load alleviation mainly focusses on lift and therefore accurate lift predictions are desired and thus usage of either of the three codes is justified.

Since the limited version of RFOIL does not support batch mode and cannot be interfaced with, it is not suitable for the aeroelastic analysis. However, RFOIL is used in other parts of the project.

Finally, it was decided not to change the aerodynamic code of the aeroelastic tool by Kuder et al. [2] and continue using XFOIL since the time required to implement Q³UIC could not be justified by the marginally better predictions when lift is considered. However, also Q³UIC is used in other parts of the project.

Aeroelastic model

As presented in Section 2.3.2, Kuder et al. [2] developed a model which simulates the static aeroelastic response of a selectively compliant airfoil with integrated variable stiffness bi-stable elements. Section 6.1 briefly addresses the working procedure of this model, Section 6.2 addresses the validation of the model and Section 6.3 presents a short overview of the modifications which were made to the model for this project.

6.1 Working procedure

The working procedure of the aeroelastic model by Kuder et al. [2] was briefly discussed in Section 2.3.2. Not every step of the working procedure is discussed in detail in this Section, only the most important steps are covered. As mentioned in Section 2.3.2, the aeroelastic model consists of several Python scripts for the commercial software Abaqus, this means the Graphical User Interface is not needed in order to create a model and specify and run a simulation. The three most important scripts and their main steps are discussed in the following Sections. A general diagram of the aeroelastic model is presented in Figure 6.1. The working procedure steps include the modifications to the model which are discussed in more detail in Section 6.3.

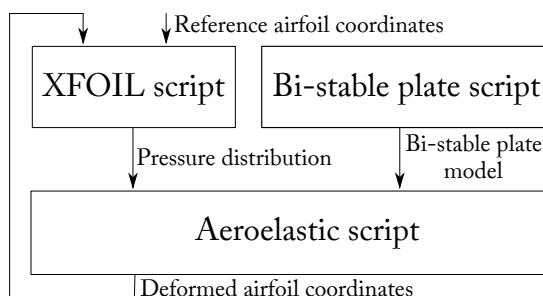


Figure 6.1: Aeroelastic model diagram.

6.1.1 Bi-stable plate script

The 'bi-stable plate script' creates the bi-stable plate model with an unsymmetrical lay-up which obtains bi-stable properties through residual stresses after thermal curing. This model is imported in the aeroelastic script. More information on the bi-stable plate can be found in Section 9.1.

First, the geometry of the plate, location, rotation angle, material properties and lay-up are specified. It must be noted that this plate can not be translated or rotated once imported in the airfoil model, hence the correct rotation angle and location of this plate must be specified during the creation of the plate, i.e. in the script. For the exact layup and material properties, see Section 9.1. Next, the curing process of the laminate is simulated by applying a temperature difference of 59 K. The cool-down shape of the plate is obtained after removal of the temperature difference. Hereby a residual stress field is created which induces the bi-stable properties of the plate. Finally, the model is saved manually so it can be imported in the airfoil model.

6.1.2 XFOIL script

In the first iteration of the 'aeroelastic script' (see the following Section) the 'XFOIL script' imports the coordinates of a specified airfoil, in this case those of the DU 93-W-210 airfoil. The script then sends commands to XFOIL which calculates the aerodynamic pressure distribution for this profile for conditions specified in the aeroelastic script. This pressure distribution is then loaded by the aeroelastic script.

In the following iterations of the aeroelastic script, the XFOIL script calculates the aerodynamic pressure distribution of the deformed airfoil shape which is obtained from the aeroelastic script. In the final iteration of the aeroelastic script, the aerodynamic performance of the deformed profile is saved.

6.1.3 Aeroelastic script

The aeroelastic script is the main script and the backbone of the aeroelastic model. This script creates the airfoil model with integrated variable stiffness bi-stable elements. The initial, undeformed airfoil shape is generated based on the coordinates of the specified airfoil. The aerodynamic conditions and airfoil chord length as well as the material lay-up, layer thickness and material properties are specified. Furthermore, the location of the webs and the bi-stable plate are specified.

In the first iteration of the script, the bi-stable plate angle and location are calculated, this information is manually transferred to the bi-stable plate script in order to generate the desired bi-stable plate model. Also, the flanges to which the bi-stable plate attaches are generated. The bi-stable plate model including stress field is imported into the model by means of an 'InitialState', this is explained in more detail in Section 6.3.3. This plate is coupled to the flanges so the model behaves as an integrated assembly. The appropriate (composite) materials are applied to the flanges and the airfoil skin and webs. The part in front of the trailing edge of the airfoil is clamped and thus assumed to be infinitely stiff. Next, the pressure distribution is imported from the XFOIL script and interpolated onto the model. Optionally, a corrugated skin is specified at a defined location, more details in Section 6.3.3 and Section 9.2. Now the model is complete and the deformation of the profile under the aerodynamic pressure is computed.

In the second iteration of the script, the deformed profile is fed into the XFOIL script which

calculates the new pressure distribution for the deformed profile. This new pressure distribution is applied to the deformed profile and the second deformed profile is computed. This iterative process continues until a specified trailing edge displacement convergence criteria (a displacement of less than 0.2 mm in one iteration of the aeroelastic script) is met.

The final deformed shape and its corresponding aerodynamic performance are computed and saved so the aerodynamic efficiency of the profile in terms of load alleviation by passive morphing can be assessed. Please note that no dynamic effects are treated and hence this is a static aeroelastic analysis.

6.2 Validation

As mentioned in Section 2.3.2, the model was partially validated by Kuder et al. [2] with experimental results regarding the structural response. Hence only the model's structural response was validated. The next logical validation step would be a wind tunnel test of the model. Hereby, the aerodynamic response of the model could be validated as well. Unfortunately, there was no room for a wind tunnel test in the time frame of this project.

6.3 Modifications

Some modifications were made to the model of Kuder et al. [2]. Trivial modifications were made in order to allow for a thicker, different airfoil profile to be used. However, some more fundamental modifications were made, these are briefly presented in the following sections.

6.3.1 Bi-stable plate script modifications

The only modification to the bi-stable plate script is the addition of a translation and rotation step which allows for the positioning of the plate according to the values specified by the aeroelastic script. Hereby the implementation of the bi-stable plate model in the airfoil model is made easier and positioning iterations and manual measurements are no longer required. Hence, the bi-stable plate model used in this project is identical to the model developed by Kuder et al. [2].

6.3.2 XFOIL script modifications

The XFOIL script was modified in order to include the reference airfoil. As mentioned in Section 3.2, a weighted average approach is suggested. In order to reduce computational time and increase robustness, it is opted not to perform two XFOIL calculations and an averaging step for each iteration of the aeroelastic script. Instead, the pressure distribution is calculated for a profile with forced boundary layer transition at 5% of the chord at the suction side. Hence no weighted average approach is adopted. However, since the weight for data with forced boundary layer transition normally is 75% it is considered an improvement over the unmodified XFOIL script which uses free boundary layer transition. This is a conservative measure since the blade should be able to passively alleviated load, also when the blades are dirty and thus boundary layer transition is forced. Furthermore, it must be noted that the effect of a weighted average approach decreases with an increasing AOA, since the transition point in the case of

free transition moves forward. Hence at high AOA, forced boundary layer transition has no effect since free boundary layer transition already occurs further upstream over the profile.

6.3.3 Aeroelastic script modifications

Some lines in the aeroelastic script were added for the calculation of the required bi-stable plate rotation and translation based on the web positions and for the creation of two flanges of equal length.

Abaqus version 6.13-2 showed issues with importing of the stress field of the bi-stable plate model. Kuder suggested to use a so-called 'InitialState' to import the bi-stable plate with internal stress field. Therefore, the aeroelastic script was modified in order to import the bi-stable with the aforementioned method. It must be noted that with this import method only one bi-stable plate can be imported into a model. No issues were experienced with this import method for Abaqus version 6.13-2 and 6.14-1.

For the addition of the corrugated skin, a so-called 'GeneralStiffnessSection' was specified. Hereby a material's linear structural response can be specified with an **ABD** matrix. In Section 9.2.1 this **ABD** matrix is explained in more detail. An additional axis system was defined in order to specify the material direction of the corrugated skin.

Conditions for load alleviation

In order to design a wind turbine blade section which passively alleviates load, it is important to know the conditions at which load alleviation should occur to ensure that load alleviation occurs at the desired conditions and thus protects the structure from damage. However, it is important that load alleviation does not occur at conditions below the threshold in order not to compromise energy production. In this Chapter, these conditions are determined. Furthermore, the change in loading during these conditions is quantified.

In Section 7.1, a modern reference wind turbine is presented. Section 7.2 addresses the change in flow conditions during an extreme operating gust. The Blade Element Momentum theory is introduced in Section 7.3. The effects of viscosity, compressibility and roughness are treated in Section 7.4. Finally, the conditions at which load alleviation should occur as well as the accompanied changes in loading are presented in Section 7.5.

7.1 Reference wind turbine

In order to assess the load alleviation potential of the morphing method by Arrieta et al. [1] as presented in Section 2.3.2, the loads on a blade section need to be calculated so a comparison can be made between a conventional blade section and one which features passive load alleviation through morphing. In order to calculate these blade loads, some wind turbine parameters are required. These parameters such as the AOA α and the relative velocity V_{rel} determine the flow conditions at the blade section. As mentioned in Section 4.2, the focus of this study lies on large modern wind turbine blades. Therefore, one of the most recent and largest wind turbines, the Siemens SWT-6.0-154 offshore wind turbine, see Figure 7.1, was chosen as a reference. The parameters from this reference wind turbine are used in calculations regarding flow conditions and blade loads and are summarized in Table 7.1 .

Chord length distribution data was not published. A slender blade with a chord of 1 m was assumed for this project. Fortunately, the chord length is non-critical when it comes to assessing the load alleviation potential and is deemed to have a minimal effect on the outcome of this study since the blade loads scale linearly with the chord length. The only considerable impact of the chord length in this study originates from the Reynolds number which is influenced by the local chord length. Viscosity effects are treated in more detail in Section 7.4.

According to the Siemens product brochure [7, p. 7], the power output of this wind turbine is controlled by means of pitch regulation. It is assumed that the rotational speed is constant at 11 rpm at wind speeds above rated. The upper limit of the rated wind speed interval, 14 m/s, is used during all calculation. In order to avoid over complication of this initial study, a homogeneous flow field is assumed. This means that wind shear and rotor tilt (6° [49] for reference wind turbine) are not taken into account.

Parameter	Value
Hub height z_{hub}	102 [m] [50]
Rotor diameter D	154 [m] [49]
Number of blades N_{blades}	3 [-] [49]
Rated wind speed V_{rated}	(12-)14 [m/s] [49]
Cut-out wind speed V_{cutout}	25 [m/s] [49]
Rotational speed ω	5-11 [rpm] [49]
IEC class (see Section 7.2)	IA [7, p. 7]

Table 7.1: Parameters from the Siemens SWT-6.0-154 reference wind turbine.



Figure 7.1: Illustration of the Siemens SWT-6.0-154 reference wind turbine. [7, p. 7]

7.2 Extreme operating gust

In order to specify a load case that is relevant when wind turbine blades are considered, the International Electrotechnical Commission (IEC) 61400-1:2005 wind turbine design requirement standard [51] was studied. This standard defines some extreme wind conditions such as wind shear events, peak wind speeds and rapid changes in wind speed and direction. It is believed that one of the most dominant extreme wind conditions for the structural requirements of a wind turbine blade is the extreme operating gust (EOG). An EOG is a gust which occurs whilst

the wind turbine is operating and thus generating power. Therefore the EOG as specified by this standard is chosen as a reference condition. The conditions at which load should alleviation should occur are determined in Section 7.5.

The hub height gust magnitude V_{gust} is given by the following expression; [51, p. 26]

$$V_{gust} = \min \left(1.35(V_{e1} - V_{hub}); 3.3 \left(\frac{\sigma_1}{1 + 0.1 \frac{D}{\lambda_1}} \right) \right) \quad (7.1)$$

The rotor diameter D was defined in the previous Section. The wind speed at hub height V_{hub} is selected later in this Section. The longitudinal turbulence scale parameter λ_1 is defined as 42 m when the hub height z exceeds 60 m [51, p. 23]. The longitudinal turbulence standard deviation σ_1 is given by; [51, p. 24]

$$\sigma_1 = I_{ref}(0.75V_{hub} + b) \quad (7.2)$$

Where b is 5.6 m/s [51, p. 24]. The expected value of turbulence intensity at 15 m/s, I_{ref} is 0.16 for a wind turbine of class A which is the category for higher turbulence characteristics [51, p. 22]. The extreme wind speed $V_{e1}(z)$ with a recurrence period of 1 year is given by; [51, p. 25]

$$V_{e1}(z) = 0.8V_{e50}(z) \quad (7.3)$$

Where the extreme wind speed $V_{e50}(z)$ with a recurrence period of 50 years is given by; [51, p. 25]

$$V_{e50}(z) = 1.4V_{ref} \left(\frac{z}{z_{hub}} \right)^{0.11} \quad (7.4)$$

In this case the height z at which the EOG is calculated is set equal to the hub height z_{hub} since the flow field is assumed to be homogeneous. The reference wind speed average over 10 min V_{ref} is 50 m/s for wind turbines of class I [51, p. 22].

The EOG wind speed history for a wind speed of 14 m/s at hub height (rated wind speed of reference turbine) and 25 m/s (cut-out wind speed of reference turbine) can be seen in Figure 7.2. The maximum wind speeds during the EOG (18.60 m/s and 31.95 m/s respectively) are used for the calculation of the flow conditions and gust loads in Section 7.5

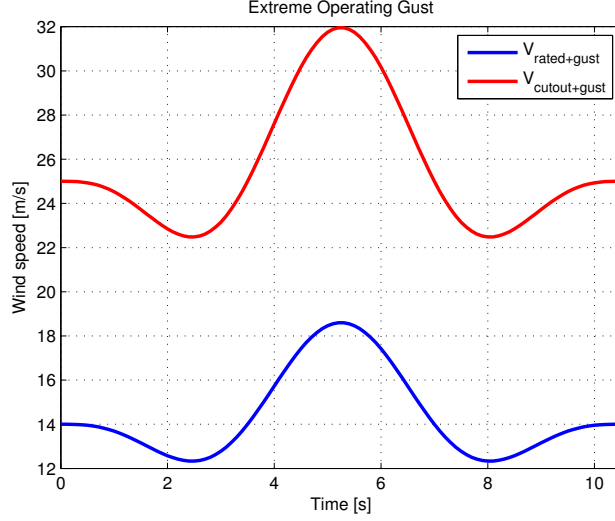


Figure 7.2: EOG wind speed history.

7.3 Blade Element Momentum method

A Blade Element Momentum (BEM) method is used for the determination of the flow conditions and the loads on a reference blade section of a pitch controlled wind turbine. This Section summarizes the procedure of the BEM method by Hansen [37] which was used for this study.

1. The axial induction factor a and tangential induction factor a' , see Figure 7.3, are initialised. Both are set equal to zero.
2. The flow angle ϕ , see Figure 7.3, is calculated with the following equation;

$$\tan(\phi) = \frac{(1 - a)V_0}{(1 + a')\omega r} \quad (7.5)$$

Where ω is the rotational speed, r is the spanwise location of the reference section and V_0 is the wind speed normal to the rotor plane.

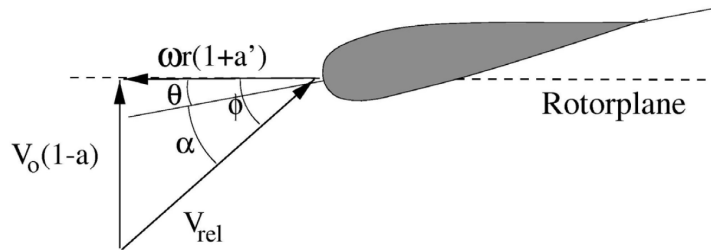


Figure 7.3: Velocities at the rotor plane. [8, Lecture 'Control']

3. The local AOA α is computed with the following equation;

$$\alpha = \phi - \theta \quad (7.6)$$

Where θ is the pitch angle of the rotor blade.

4. Lift coefficient C_l and drag coefficient C_d are determined from wind tunnel data through interpolation for the exact AOA.
5. The normal force coefficient C_n and tangential force coefficient C_t are computed with the following equations;

$$C_n = C_l \cos(\phi) + C_d \sin(\phi) \quad (7.7)$$

$$C_t = C_l \sin(\phi) - C_d \cos(\phi) \quad (7.8)$$

6. Taking into account the Prandtl tip loss factor, the induction factors a and a' are calculated with the following equations;

$$a = \frac{1}{\frac{4F \sin(\phi)^2}{\sigma C_n} + 1} \quad (7.9)$$

$$a' = \frac{1}{\frac{4F \sin(\phi) \cos(\phi)}{\sigma C_t} - 1} \quad (7.10)$$

Where the local solidity σ is defined by the following equation;

$$\sigma = \frac{c(r)B}{2\pi r} \quad (7.11)$$

And the Prandtl tip loss factor F is defined by the following equation;

$$F = \frac{2}{\pi} \cos^{-1}(e^{-f}) \quad (7.12)$$

Where f is defined by the following equation;

$$f = \frac{B(R-r)}{2r \sin(\phi)} \quad (7.13)$$

7. If the induction a and a' factors have changed more than a specified tolerance (0.000001), the procedure is repeated with the new induction factors from step 2 onwards. If the induction factors have changed less than this tolerance, step 8 can be performed.
8. The aerodynamic resultant force R on the blade, see Figure 7.4, can be decomposed in a component normal to the rotor plane p_N and a component parallel to the rotor plane p_T . These loads can be calculated with the following equations;

$$p_N = C_n \frac{1}{2} \rho V_{rel}^2 c \quad (7.14)$$

$$p_T = C_t \frac{1}{2} \rho V_{rel}^2 c \quad (7.15)$$

Where c is the local chord length, ρ is the air density. The relative velocity V_{rel} experienced by the blade section is defined by the following equation;

$$V_{rel} = \frac{V_0(1-a)}{\sin(\phi)} \quad (7.16)$$

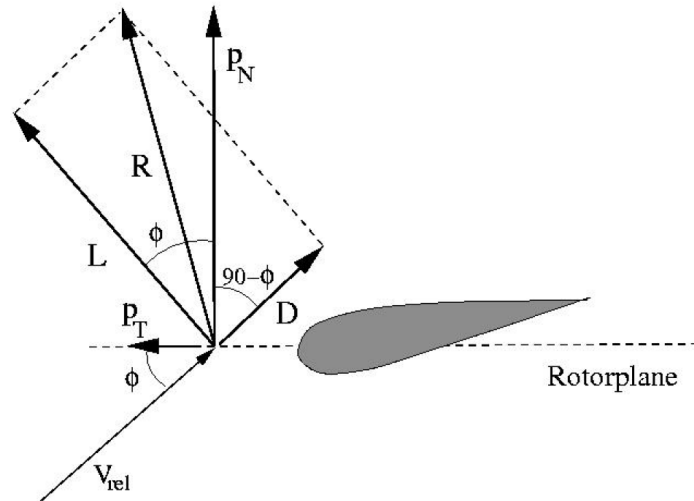


Figure 7.4: Local loads on a blade section. [8, Lecture 2]

Then the normal force and torque generated by the blade section are determined with the following equations;

$$F_N = p_N dr \quad (7.17)$$

$$T = r p_T dr \quad (7.18)$$

Where dr is the width of the blade section and r is the distance between the blade root and the middle of the blade section.

With the presented BEM method, the dominant flow conditions (the AOA and relative velocity) and the dominant loads generated by a blade section (the normal force and the torque) can be determined. In Section 7.5, these flow conditions and loads are calculated and presented.

7.4 Viscosity, compressibility and roughness effects

This Section deals with three effects, namely viscosity, compressibility and roughness, which have to be taken into account during the aerodynamic analysis of wind turbine blade sections. The tip sections of modern wind turbine blades achieve relatively high speeds. Therefore it is important to look at viscosity and compressibility effects since these can have a significant impact on the aerodynamic performance.

Viscosity effects are governed by the Reynolds number Re which is defined as follows; [52]

$$Re = \frac{\rho V L}{\mu} \quad (7.19)$$

According to McLean [53, p. 63], the Reynolds number determines ... *how "fast," relative to the flow velocity, momentum will be diffused in the cross-stream direction by viscosity or turbulence and thus how thick the boundary layer will grow relative to the dimensions of the*

body. As Reynolds number increases, the diffusion of momentum becomes relatively slower, and the boundary layer will be thinner...

Compressibility effects are governed by the Mach number M which is defined as follows; [54]

$$M = \frac{V}{c_{air}} \quad (7.20)$$

Where V is the mean velocity over the profile which is equal to the relative velocity V_{rel} in this case. Furthermore, ρ is the air density, μ is the dynamic viscosity and L is the chord length which is equal to chord length c in this case. c_{air} is the speed of sound in air.

From the BEM results which are presented in Section 7.5 in Table 7.3 on page 42, it is found that V_{rel} is around 80 m/s. The dynamic viscosity and speed of sound of air at 15°C, 1.81e-5 kg/(m·s) [52] and 340.3 m/s [54] respectively, are used. An air density of 1.225 kg/m³ and chord length of 1 m are assumed.

Table 7.2 summarizes the Reynolds and Mach numbers for 4 cases which are introduced and explained in detail in Section 7.5.

V_0 [m/s]	Re [-]	M [-]
14.00 (V_{rated})	5.31e6	0.230
18.60 ($V_{rated+gust}$)	5.37e6	0.233
25.00 (V_{cutout})	5.49e6	0.238
31.95 ($V_{cutout+gust}$)	5.65e6	0.245

Table 7.2: Local Reynolds and Mach numbers for various cases from BEM calculations (rounded values).

The wind tunnel data presented in Section 5.2.1 was obtained at a Reynolds number of 3.0e6 and a Mach number of 0.22. This means that the blade section operates at a Reynolds number which is higher than the Reynolds number at which the wind tunnel data was obtained. The effect on the aerodynamic performance of the Reynolds number can be seen Figure 5.4 on page 26. It is assumed that the difference in aerodynamic performance for a Reynolds number of 3.0e6 compared to the Reynolds numbers in Table 7.2 is small. Furthermore, it can be observed that the difference in Mach number is small and hence a minimal performance difference is expected for a Mach number of 0.22 compared to the Mach numbers in Table 7.2. Therefore it is concluded that the wind tunnel data is appropriate for use in BEM calculations when viscosity and compressibility effects are considered.

However, as mentioned in Section 3.2, wind turbine blades often have a build up of dirt which causes the blade surface to become rough and can trigger early laminar to turbulent transition of the boundary layer. This transition has a detrimental effect on the aerodynamic performance and hence affect power production. Zhu et al. [36] acknowledged the effects of roughness on wind turbine blades which causes early laminar to turbulent transition and introduced a weighted average approach. This approach is adopted in this study. Effectively, this means that the aerodynamic performance is determined by a weighted average of the performance of a clean profile and that of a profile with forced boundary layer transition. The weighting factors by Zhu et al. [36], 25% and 75% for clean profile performance and forced boundary layer transition performance respectively, are carried over. It is anticipated that by using this weighted average approach, more realistic aerodynamic results are obtained.

Fortunately, as can be seen in Figure 5.3 on page 25, wind tunnel data of the reference airfoil is also available with forced boundary layer transition by means of a trip wire at 5% chord on the

suction sided which simulates the effect of surface roughness. The weighted average of the lift and drag coefficients of the reference airfoil can be seen in Figure 8.8 for wind tunnel as well as RFOIL data.

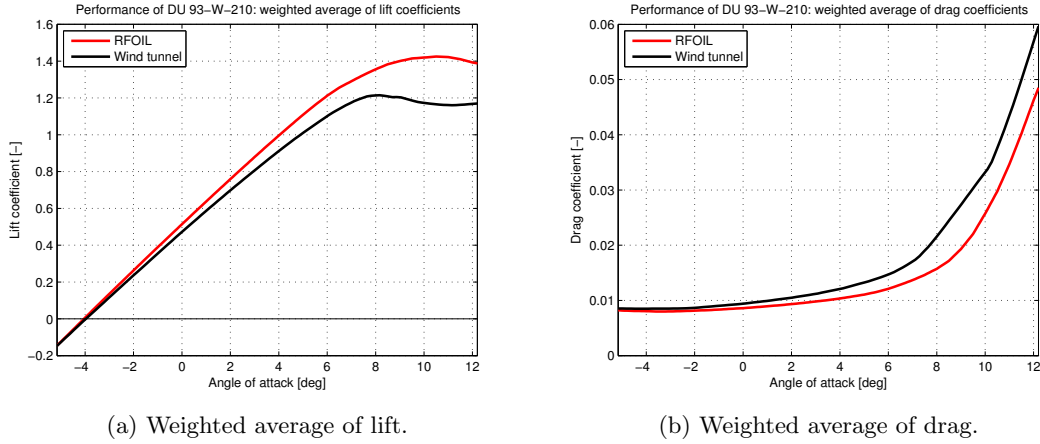


Figure 7.5: Weighted average of wind tunnel lift and drag of DU 93-W-210 airfoil.

7.5 Flow conditions and loads

In Section 7.2, the EOG was identified as a critical load case at which load alleviation should occur in order to protect the blade structure from high loads. In this Section, the main flow conditions (AOA and relative velocity) and the main loads generated by a wind turbine blade section (normal force and torque) are evaluated for the case of an EOG. The effect of this gust is calculated for the two ends of the rated power wind speed envelope. Effectively, this means the effect is determined for a gust which occurs at rated wind speed and for a gust which occurs at cutout wind speed. This corresponds to the wind speed values presented in Figure 7.2 on page 36 and in Table 7.2.

The results of this Section are based on the assumption that the power generated by an outboard blade section of a pitch regulated wind turbine which operates at constant rotational speed above rated wind speed is linearly dependant on the total power output of the wind turbine at wind speeds above rated. Effectively, this means that the torque generation of an outboard blade section is constant for the wind speed envelope ranging from rated wind speed to cutout wind speed. Furthermore, it is important to keep in mind that the results presented in this study are for a discrete outboard section which is located at 10 m from the tip of the blade and hence not for a complete wind turbine blade.

Before the impact of the EOG is determined, the pitch angles at V_{rated} and V_{cutout} are calculated with a BEM method code based on the Equations presented in Section 7.3. It is assumed that when the wind speed reaches V_{rated} , the wind turbine extracts the maximum amount of power from the flow, this amount is called the rated power. As the wind speeds increases between V_{rated} and V_{cutout} , the blades are pitched to keep the power output constant. Hence the torque generated by a blade section is constant at wind speed above V_{rated} since the reference wind turbine is assumed to operate at constant rotational speeds at wind speeds above V_{rated} .

The pitch angle at V_{rated} is determined by calculating the torque generated by a wind turbine blade section for a wide range of pitch angles, see the blue curve in Figure 7.8a on page 43. The

pitch angle at V_{rated} is the pitch angle at which the maximum torque is generated, see the blue circle in Figure 7.8a. The normal force at V_{rated} is represented by the blue curve and the blue circle in Figure 7.8b, the latter is the operating point at V_{rated} .

The pitch angle at V_{cutout} is determined in a similar fashion. The torque generated by a wind turbine blade section at is calculated for a wide range of pitch angles, see the the red curve in Figure 7.8a. The pitch angle at which the same torque is generated as at the operating point at V_{rated} is the pitch angle at V_{cutout} . Hence the 'equal power - equal torque' condition was applied, the black dotted line in Figure 7.8a represents the 'rated power torque level'. The normal force at V_{cutout} is represented by the red curve and the red circle in Figure 7.8b, the latter is the operating point at V_{cutout} .

Since the flow conditions (Table 7.1 on page 34) and loads (Figure 7.8) during wind turbine operating conditions at V_{rated} and V_{cutout} are known, the effect of the EOG can be calculated. It must be noted that the effect of an EOG is determined under the assumption that the flow conditions can be treated as quasi-steady. Hence unsteady aerodynamic effects are not taken into account. An unsteady aerodynamic effect called dynamic stall is addressed in Section 8.4.

The effect of an EOG is determined by performing the same BEM method calculations with a constant pitch angle and an increased wind speed, see Table 7.3 for the specific values. The impact on the generated torque is depicted in Figure 7.8a by the blue asterisk for an EOG at V_{rated} and the red asterisk for an EOG at V_{cutout} . Similarly, in Figure 7.8b, the effect on the normal force is depicted.

Table 7.4 summarizes the change in flow conditions and loads generated by a blade section as a result of an EOG at V_{rated} and V_{cutout} . From Figure 7.8 and Table 7.4, it is clear that the highest absolute as well as relative increase in blade loads as a result of an EOG occur at V_{cutout} . However, the normal force which is generated during an EOG at V_{cutout} is still smaller compared to the normal force generated at V_{rated} .

The decrease in normal force as a result of an EOG at V_{rated} can be explained with the help of Figure 7.3 on page 36 and Figure 7.4 on page 38. It must be stressed that the change in conditions and loads is assessed at the point at which the wind speed due to a gust achieves a maximum. A gust has two principal effects; an increase in V_{rel} and an increase in flow angle. Looking at Figure 7.4, this results in a rotation of the lift vector towards the rotor plane. A secondary effect of the change in flow angle is a change in AOA. At V_{rated} the blade section is operating at a high AOA, very close to the maximal lift. An increase in AOA from 7.64° to 11.31° results in a reduction in lift coefficient because of stall effects. The combined effect of a reduction in lift coefficient and a rotation of the lift vector are the main causes for a reduction in the normal force as a result of an EOG at V_{rated} . It is important to recall that dynamic effects are not taken into account. The increase in torque can be prescribed to the rotation of the lift vector towards the rotor plane, hereby, the tangential force P_T is increased which results in an increase in generated torque.

In the case of an EOG at V_{cutout} , the effect on the loads is more significant since the increase in flow angle and thus in AOA results in an increase in lift coefficient because the blades operate at a small AOA, see Table 7.3.

It can be concluded that the impact on the loads generated by a wind turbine blade section by an EOG increases with increasing wind speed.

Especially the torque generated by a blade section tends to increase considerably at high wind speeds as a result of an EOG. This sudden increase might induce harmful edgewise vibrations which can induce unwanted load fluctuations in other wind turbine components such as the generator, besides the blade itself.

The normal force generated by a blade section seems less critical since it appears

that it never exceeds the normal force generated during operating conditions at V_{rated} . However, the significant increase in normal force as a result of an EOG at high wind speeds can still induced harmful flapwise vibrations.

V_0 [m/s]	V_{rel} [m/s]	α [deg]	θ [deg]	ϕ [deg]
14.00 (V_{rated})	78.39	7.64	1.45	9.09
18.60 ($V_{rated+gust}$)	79.34	11.31	1.45	12.76
25.00 (V_{cutout})	81.11	0.75	16.94	17.69
31.95 ($V_{cutout+gust}$)	83.52	5.18	16.94	22.12

Table 7.3: Flow conditions with and without EOG (rounded values).

ΔV_0 [m/s]	ΔV_{rel} [m/s]	$\Delta \alpha$ [deg]	ΔT [%]	ΔF_N [%]
4.60 (32.84 %) ($V_{rated+gust}$)	0.94 (1.20 %)	3.67	25.49	-2.15 (0.71)
6.95 (27.81 %) ($V_{cutout+gust}$)	2.41 (2.97 %)	4.43	147.58	89.64

Table 7.4: Change in flow conditions and loads as a result of an EOG (rounded values).

The time response of the loads during an EOG can be seen in Figure 7.7. Please note that a quasi-steady scenario is assumed and no dynamics effects are taken into account.

In Table 7.4, the value between brackets for normal force at $V_{rated+gust}$ is the maximum value it attains during a gust, since the maximum is not attained at the maximum velocity because of stall effects, see Figure 7.7b. It is clear that the airfoil is operating near maximum thrust and the normal force can not exceed its value when dynamic effects are not taken into account. Section 8.4 gives an impression of the effect of dynamic stall.

With the effect of an EOG on the flow conditions and blade loads known, the morphing mechanism and the governing parameter for triggering the snap-through are addressed in Section 8.2.

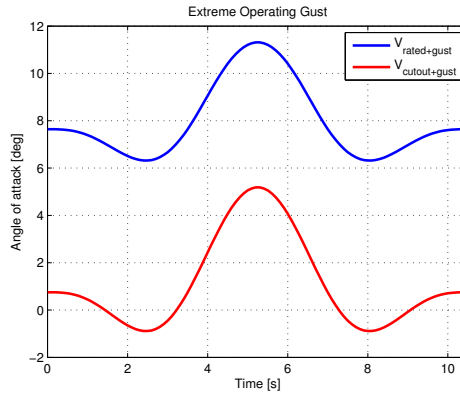
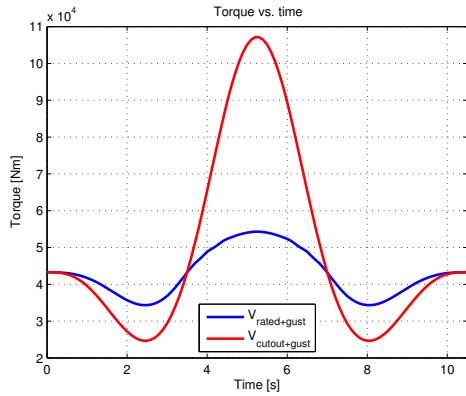
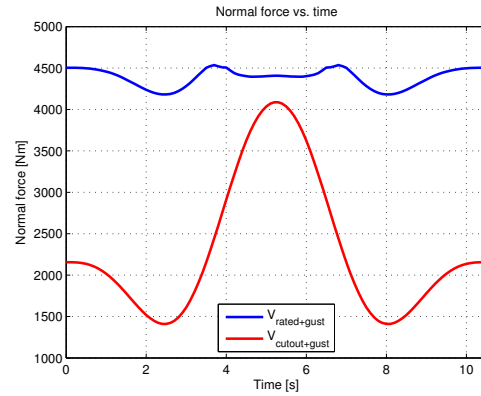


Figure 7.6: Extreme operating gust AOA history.

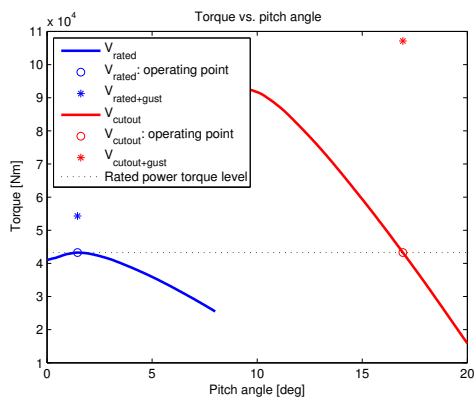


(a) Torque generation during an EOG.

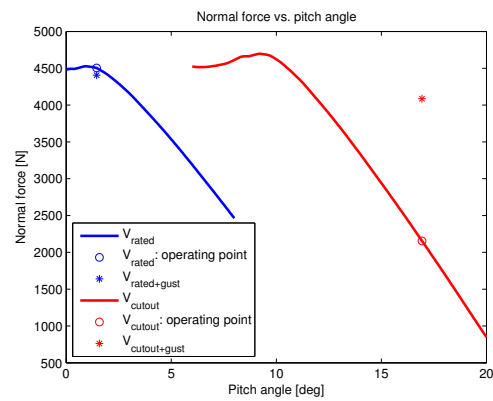


(b) Normal force generation during an EOG.

Figure 7.7: Loads generation during an EOG of a blade tip section for various conditions.



(a) Torque generation.



(b) Normal force generation.

Figure 7.8: Loads generation of a blade tip section for various conditions.

Parametric morphing study

The goal of this Chapter is to get an insight in the working principle of the morphing mechanism and to set up a realistic design envelope so a reasoned design can be made.

The assumptions and constraints are outlined in Section 8.1. A simplified morphing mechanism is introduced in Section 8.2. In Section 8.3, a parameteric study which gives an impression of the impact of a morphing profile is presented. The effects of dynamic stall and its possible implications are treated in Section 8.4. The focus of this study does not lie on the control mechanism which restores the bi-stable plate to the stiff state after load alleviation has occurred and hence is not treated extensively. Though, several control mechanism options are introduced in Section 8.5.

8.1 Assumptions and constraints

As presented in Chapter 2, several different types of morphing exist. Therefore it is important to define which type of morphing is adopted in the design of the morphing section. In Section 2.2.1, it was identified that trailing edge flaps have a significant potential for load alleviation on wind turbines blades. In the same Section, it was also shown that a lot of research has been carried out and is going on in the field of trailing edge flaps.

For this study it was therefore chosen to focus on morphing trailing edge flaps and thus limit the design freedom. An additional benefit of trailing edge flaps is the limited interference with the main load carrying structure of the wind turbine blade which is generally located in the mid to front part of the airfoil as can be seen in Figure 8.1.

The following constraints and assumptions are defined in order to keep the design as simple as possible for this initial study. Therefore, the JEEP (Just Enough Essential Parts) principle is adopted in search of a maximal effect with a minimal number of additional components.

Preferably, only one bi-stable element shall be integrated in the blade section. The trailing edge flap shall be as small as possible in order to minimize its impact on the structural layout and structural performance. Additionally, Troldborg [44] concluded that shorter trailing edge flaps are more efficient in changing the lift coefficient compared to longer trailing edge flaps. Also the trailing edge deflection angle shall be kept as small as possible in order to minimize the strain on the structure. Hence the goal is to design a structure that is able to passively alleviate load

with a morphing trailing edge flap which is as small and simple as possible.

It is assumed that the structural performance of the wind turbine blade is not affected by incorporating a morphing trailing edge flap with a length of 10-30% of the chord. As stated in Section 6.1.3, the part in front of the morphing trailing edge flap is clamped in the model and thus assumed to be infinitely stiff compared to the trailing edge. Thus deformations by aerodynamic loading on the blade section, except for the morphing trailing edge, are not taken into account.

The parametric study in Section 8.3 takes these assumptions and constraints into account, however, it does not focus on the manufacturability of the structure and hence assumes an ideal morphing scenario.

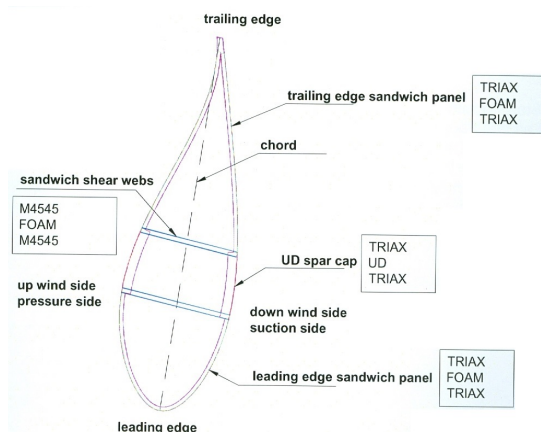


Figure 8.1: Wind turbine blade cross section. [9, p. 5]

8.2 Morphing mechanism

In order to make a well-founded design of an airfoil with a morphing trailing edge which uses bi-stable elements in order to passively alleviate load, it is important that one understands the morphing mechanism. This morphing mechanism can be simplified in order to grasp the working principle.

In essence, the morphing trailing edge can be treated as a hinged trailing edge flap which is restrained from rotating by the bi-stable plate and the top skin, see Figure 8.2. Figure 8.3 presents the corresponding free body diagram (FBD) for the simplified mechanism and a FBD for a mechanism in which the corrugated skin is taken into account.

The flap is assumed to hinge freely around a hinge point on the pressure side of the profile and the lower skin of the flap is assumed to be rigid. The lift on the flap generates a moment around the flap hinge which would induce an upward rotation of the flap if it was unrestrained. However, the bi-stable plate is connected to the lower skin of the flap and is loaded in compression when lift is generated by the flap. The compressive force on the bi-stable plate increases when the flap hinge moment increases. The flap hinge moment effectively is a measure for the 'triggering parameter' which dictates when the bi-stable plate snaps and the trailing edge effective stiffness is reduced which allows for passive morphing and deflection of the trailing edge in order to alleviate load. When a gust occurs, the AOA as well as the relative velocity increase, see Table 7.4 on page 42. This has an impact on the flap hinge moment which is determined with

the following Equation:

$$M_{flaphinge} = \frac{1}{2}\rho V_{rel}^2 c^2 C_m \quad (8.1)$$

Where C_m is the flap hinge moment coefficient which is dependant on the AOA. Figure 8.4 on page 49 shows the normalised flap hinge moment coefficients of three trailing edge flaps with a length of 10%, 20% and 30% of the chord for a range of AOA. These coefficients were obtained with RFOIL. RFOIL was used for the aerodynamic analysis since it was found in Section 5.2.1 that RFOIL gives the results closest to those of wind tunnel tests of the reference airfoil, see Figure 8.8 on page 51 for a comparison. It must be noted that these coefficients hold for an airfoil with forced boundary layer transition at 5% chord on the suction side, a Reynolds number of $3.0e6$ and a Mach number of 0.22.

It can be observed that the flap hinge moment coefficient is relatively constant at AOA under 8° and increases strongly when this angle is exceeded. The increase in flap hinge moment with AOA can be explained with the wind tunnel pressure distributions presented in Figure 5.2 on page 24. The pressure distribution for the final 20% of the chord is of particular interest. Under the assumption that skin friction drag does not contribute significantly to the flap hinge moment, it can be stated that the pressure distribution induces the flap hinge moment.

Starting with an AOA of 0° , see Figure 5.2a, it can be observed that the aft part of the pressure side of the airfoil experiences a positive pressure. This means that this side of the airfoil locally experiences a downward lift or downforce.

At an AOA of 4° , see Figure 5.2b, the pressure distribution of the final 20% of the chord is relatively similar. Hence, the flap hinge moment is expected to stay relatively constant.

However, at an AOA of 8° , see Figure 5.2c, the pressure distribution near the trailing edge starts to change. It can be observed that the suction side now experiences a small negative pressure whilst the pressure distribution on the pressure side is relatively unchanged. This change is induced by boundary layer separation, hence the flow is not attached near the trailing edge. The increase in lift from the suction side induces an increase in flap hinge moment.

At a high AOA of 12° , see Figure 5.2d, flow separation occurs further upstream. According to Katz [48, p. 509] the pressure stays constant in the region starting behind the separation point and ending at the trailing edge, which can be clearly seen in Figure 5.2d. It can be observed that this area experiences more negative pressure and thus lift. Hence it can be stated that the flap hinge moment increased even more.

In short, it can be concluded that boundary layer separation induces a constant negative pressure at the suction side downstream from the point of separation which in turn induces an increase in flap hinge moment.

It can be observed from Figure 8.4 that larger flaps are less efficient in triggering snap through in terms of relative increase in flap hinge moment. This can be regarded as favourable when the flap size and its impact on the blade design is considered. However, it can also be considered unfavourable when a lot of load needs to be alleviated as it seems that the triggering mechanism becomes less effective for larger flaps which can potentially alleviate more load.

If the compressive force on the bi-stable plate resulting from the flap hinge moment exceeds a critical value, the plate snaps which reduces its stiffness, allowing the plate to be compressed which results in a counter-clockwise rotation of the flap. This reduces the lift on the flap and thus the flap hinge moment and results in a new equilibrium situation with a deflected flap. In this process, the top skin of the flap, which is labelled '(Corrugated skin)' in Figure 8.2, is deforming. This can be either a deflection or a compression of this part of the skin which allows the trailing edge to deform. In Section 9.2, the option of a corrugated skin is addressed further, hence the label in Figure 8.2.

The normalised flap hinge moments (from RFOIL) for a flap with a length of 10% and 20% of the chord when the increase in relative velocity and AOA due to an extreme operating gust are considered are summarized in Table 8.1. The flap hinge moments are normalised against the flap hinge moment at rated wind speed. The corresponding flow conditions can be seen in Table 7.3 on page 42. The weighted average approach, see Section 7.4 has been taken into account by using the weighted averages of the flap hinge moment coefficients of a clean profile and of a profile with forced boundary layer transition.

For a similar DU profile (DU08-W180-6.5), Wolff et al. [40] found that the optimum length for a morphing trailing edge is between 15% and 20% of the chord. A flap of 30% chord was not considered since the flap hinge moment behaviour, see Figure 8.4, was found to be less desirable for passive morphing compared to the smaller flaps.

From Table 8.1 it can be observed that the minimal trigger parameter or flap hinge moment difference as a result of an EOG is around 10% whereas the maximal difference is around 50%. For the two cases, the flap hinge moment is always higher at gust conditions compared to normal conditions. This shows that there is a potential for a passive morphing mechanism which is triggered by the flap hinge moment. Whether this difference in flap hinge moment may occur from inertial effects due to blade vibrations induced by for example blade-tower interaction is not known and must be addressed in further studies.

The morphing behaviour can be fine-tuned by changing the internal layout of the morphing trailing edge flap. For example, snap-through and thus morphing at a lower flap hinge moment can be achieved by reducing the angle of the bi-stable plate with the lower skin of the flap, by reducing the stiffness of the bi-stable plate, by placing the application point more forward or by using less distributed elements along the blade span. The opposite measures can be taken to achieve morphing at a higher flap hinge moment.

This behaviour of the flap hinge moment is also visualised in Figure 8.5 which represents the flap hinge moment in function of AOA and relative velocity. The domain is bounded by the four conditions presented in Table 8.1. Again, it can be observed that there is a potential for a passive morphing mechanism. **With help of this 'trigger parameter map', a threshold flap hinge moment can be selected at which snap-through and hence load alleviation should occur. This threshold is preferable set as low as possible in order to protect the structure maximally and as high as necessary in order not to compromise power production by alleviating load during normal operating conditions.**

The presented mechanism is simplified in order to make it comprehensive, however, the aeroelastic model which was introduced in Chapter 6 takes into account a more complex interaction which is more realistic. In Chapter 9 this morphing mechanism is recreated and analysed with the aeroelastic model.

The next Section looks at the potential effect of a morphing trailing edge.

V_0 [m/s]	Flap hinge moment for flap of 0.1c [%]	Flap hinge moment for flap of 0.2c [%]
14.00 (V_{rated})	100.00	100.00
18.60 ($V_{rated+gust}$)	151.13	135.93
25.00 (V_{cutout})	107.95	109.45
31.95 ($V_{cutout+gust}$)	118.44	122.37

Table 8.1: Normalised flap hinge moment for various flaps and flow conditions.

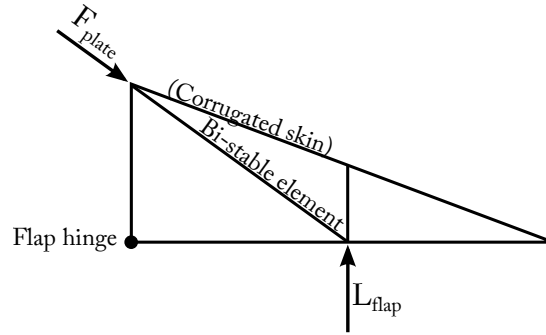


Figure 8.2: Simplified morphing mechanism.

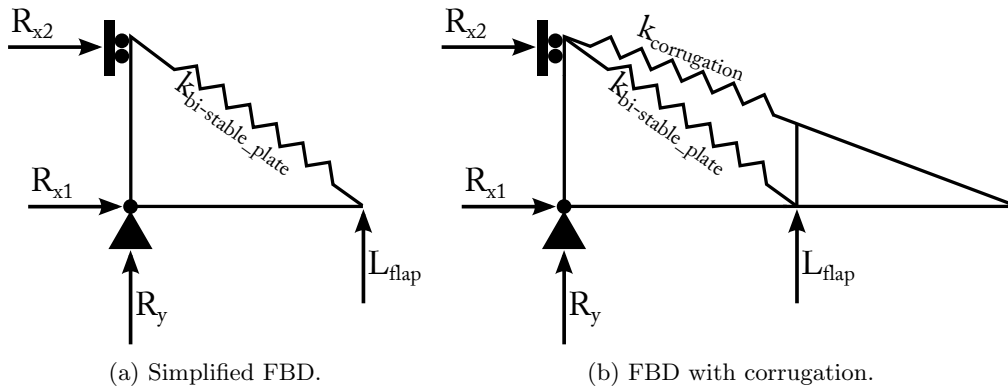


Figure 8.3: Morphing mechanism FBDs.

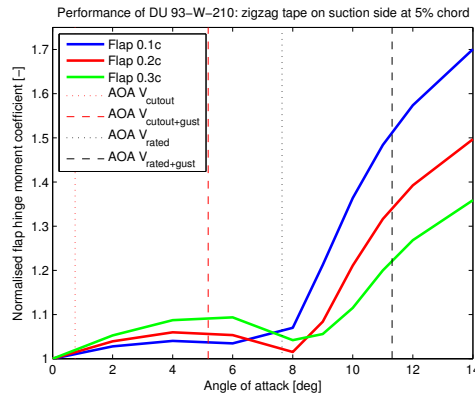


Figure 8.4: Normalised flap hinge moment coefficient for various flaps.

8.3 Parametric study

A simple parametric study with RFOIL was conducted in order to determine the potential impact of morphing flaps on the aerodynamic performance of the reference airfoil. The flaps were simulated by adding a linear ramp to the airfoil profile. Only linear flaps were considered as these were found to be most effective for lift reduction in a study by Troldborg et al. [44]. The two parameters that define the flap are the flap length f_l and the flap angle δ . Two options were selected for both parameters. Similarly to the previous Section, the flap length was either

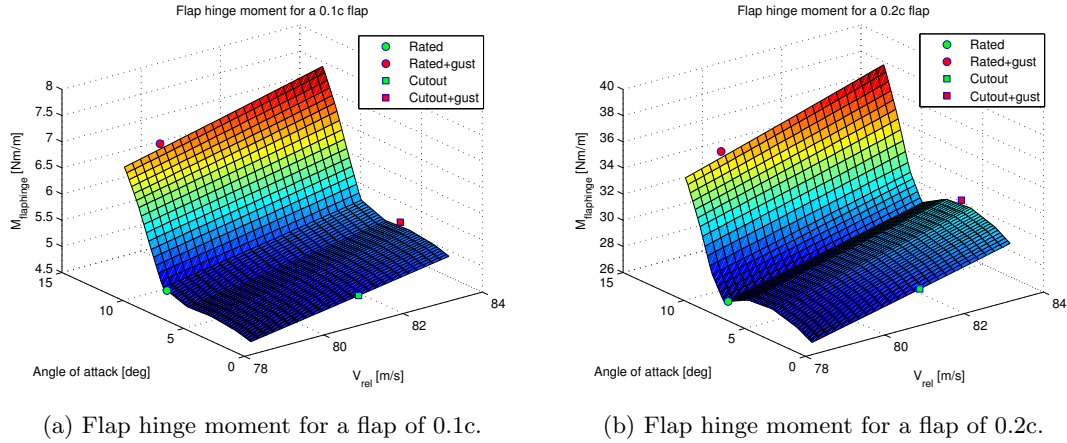


Figure 8.5: Flap hinge moment in function of relative velocity and AOA.

10% or 20% of the chord. The flap angle was either 5° or 10° . This results in four combinations which are presented in Figure 8.6.

It must be noted that the routine to generate the profile with flap is idealized since it adds a ramp to the profile instead of rotating a part of the trailing edge. Hence the actual length of the flap is slightly larger compared to the rotated case. However, the deviation in flap length $(\frac{1}{\cos(\delta)} - 1)$ remained under 1.6% in all cases.

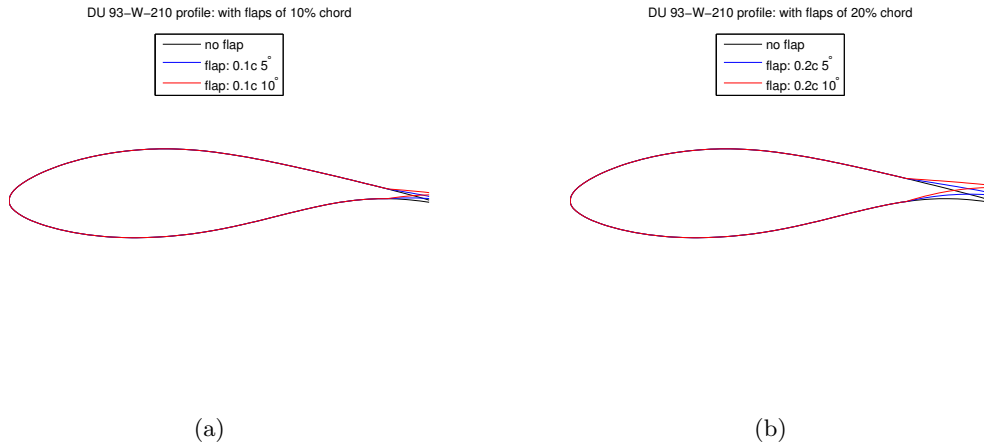


Figure 8.6: Reference airfoil with various trailing edge flaps.

In order for the RFOIL results to match the wind tunnel results which were used previously, see Figure 8.8 on page 51, two correction (scaling) factors were applied. This factor for lift and drag coefficient is presented in Figure 8.7 in function of AOA. The lift correction factor was set to 1 at angles below -2° since the correction factor becomes very large when the lift coefficient is close to zero.

It is important to note that this scaling does not have an impact on the relative behaviour of lift and drag curves with respect to each other, it only changes their absolute value so they can be directly compared with wind tunnel test results. Also, since RFOIL over predicts lift at high AOA as can be seen in Figure 5.3 on page 25, the reductions in lift would be smaller and less realistic if uncorrected RFOIL data was used. It must be noted that this is a very crude

way of matching wind tunnel and simulation results. For example, the zero-lift AOA changes with airfoil camber (and thus flap deflection) and induces an angular mismatch between the correction coefficients. However, the results are only used for indicative purposes and thus this approach is deemed acceptable.

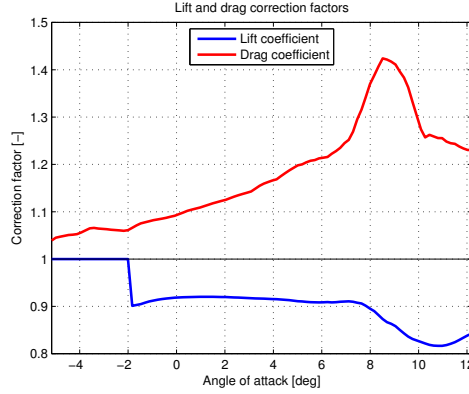


Figure 8.7: Lift and drag coefficient correction factors

Figure 8.8 presents the weighted averaged lift and drag polars from RFOIL for the four parametric flaps which were presented earlier. The results were scaled with the correction factors presented in Figure 8.7.

It can be observed that the lift coefficient, see Figure 8.8a reduces drastically in the linear region since the zero-lift AOA increases as a result of the flaps. Furthermore, stall becomes less abrupt due to the flaps.

It can be conclude that the flap angle is dominant when it comes to a reduction in lift, especially at high AOA. This is illustrated by a small flap with a 10° flap angle having a larger lift reduction compared to a large flap with a 5° flap angle.

The drag coefficient, see Figure 8.8b, reduces due to the flaps. However, the impact of this drag reduction on the blade loading is minimal.

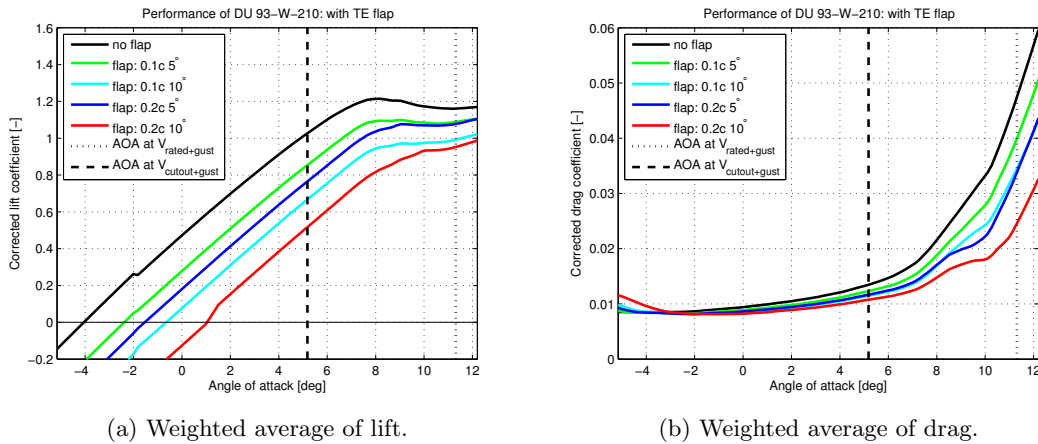
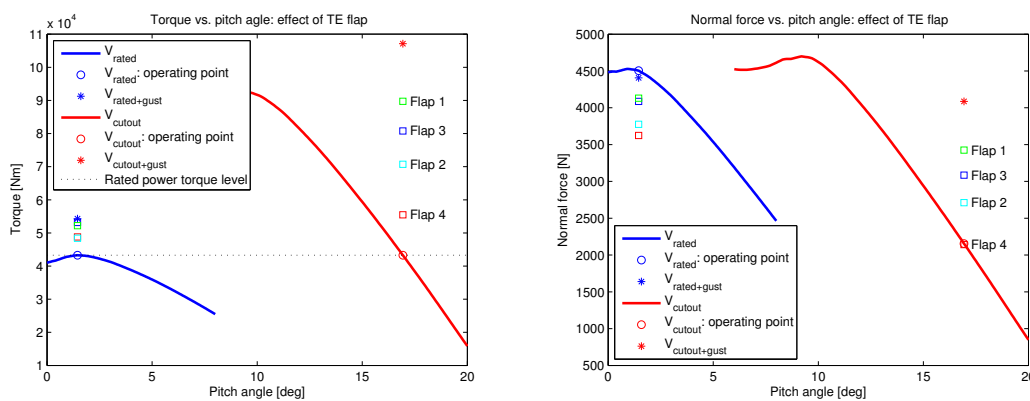


Figure 8.8: Effect of flaps on lift and drag polars.

The potential impact of these flaps on torque and normal force generation is visualised in Figure 8.9. It must be noted that the presented results do not include dynamic effects and

are based on the static loads as presented in Figure 7.8 on page 43. It is apparent that a significant amount of load can be alleviated with flaps and that they have the potential to offset the increase in loads due to a gust to a large degree.

Furthermore, the potential impact is presented numerically in terms of lift and drag coefficient in Table 8.2 as well as in terms of normal force and torque generation in Table 8.3. It can be observed that the load alleviation potential is higher at low AOA (cutout+gust conditions). Again, the flap angle is dominant for the amount of load alleviation at high AOA (rated+gust conditions).



(a) Effect of TE flap on torque generation.

(b) Effect of TE flap on normal force generation.

Figure 8.9: Effect of TE flap on loads generation of a blade tip section.

#	l_f [c]	δ [°]	ΔC_l $V_{rated+gust}$ [%]	ΔC_l $V_{cutout+gust}$ [%]	ΔC_d $V_{rated+gust}$ [%]	ΔC_d $V_{cutout+gust}$ [%]
1	0.1	5	-6.28	-16.81	-15.77	-8.60
2	0.1	10	-14.57	-35.03	-27.33	-14.85
3	0.2	5	-7.21	-25.47	-28.73	-13.41
4	0.2	10	-17.98	-49.63	-48.19	-20.20

Table 8.2: Effect of flaps on lift and drag coefficients in gust conditions.

#	l_f [c]	δ [°]	ΔF_N $V_{rated+gust}$ [%]	ΔF_N $V_{cutout+gust}$ [%]	ΔT $V_{rated+gust}$ [%]	ΔT $V_{cutout+gust}$ [%]
1	0.1	5	-6.26	-16.19	-3.86	-16.24
2	0.1	10	-14.33	-33.65	-10.85	-33.98
3	0.2	5	-7.27	-24.50	-2.08	-24.60
4	0.2	10	-17.78	-47.61	-10.16	-48.23

Table 8.3: Effect of flaps on the normal force and torque generated by a blade section in gust conditions.

8.4 Dynamic stall

Please note that dynamic effects were not planned to be considered during this study and hence a steady BEM method was used instead of an unsteady BEM method. There is however a dynamic effect called dynamic stall which can have a significant impact on the blade gust loads

at high AOA. Therefore, this Section deals with dynamic stall in order to get an insight of the effect of dynamic stall. Just as Section 8.3, this small study is for indicative purposes only. According to Burton et al. [55, p. 189] dynamic stall is a phenomenon caused by a change in AOA. In case of wind turbines, this change in AOA can be caused by a gust. As the AOA changes and exceeds the static stall angle, a separated vortex travels downstream from the leading edge. While the vortex passes over the profile, the lift is increased. When the vortex has passed the trailing edge, the lift drops suddenly. These events are presented in Figure 8.10.

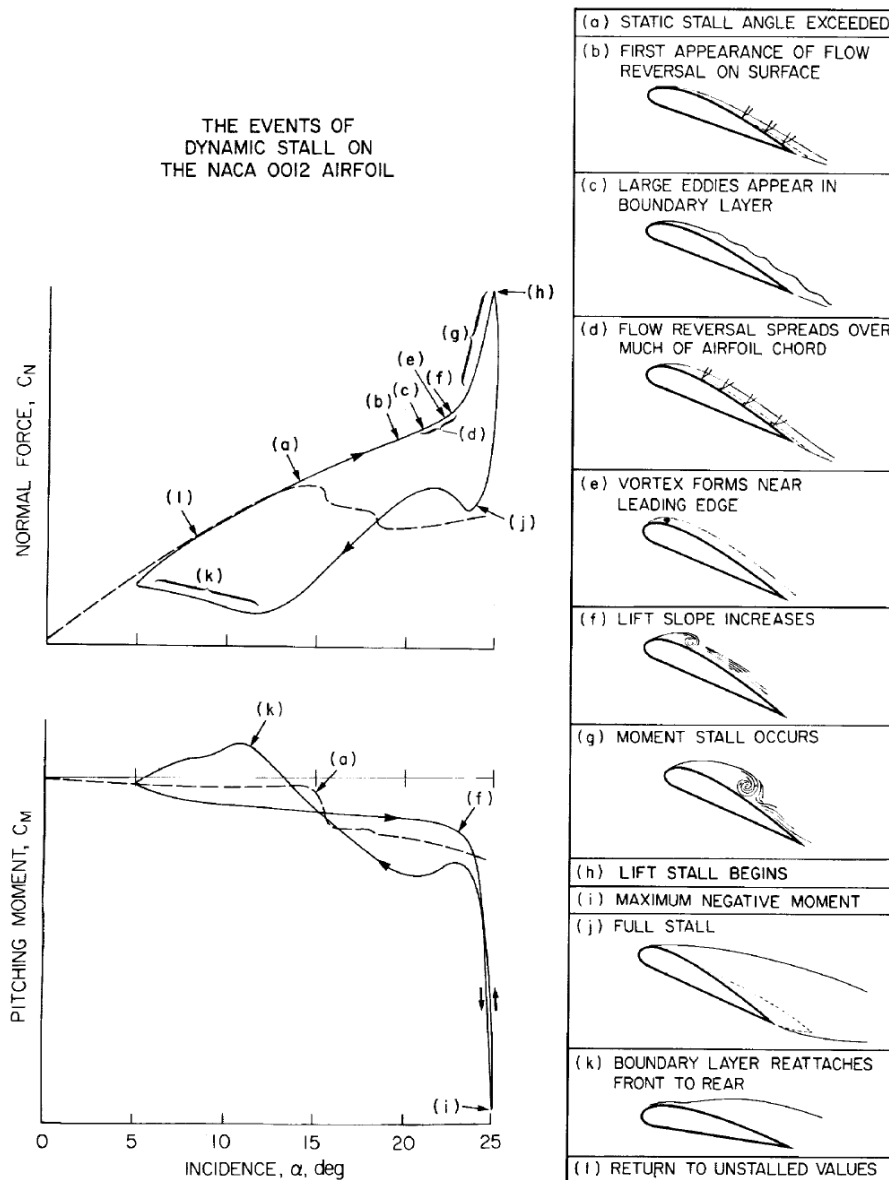


Figure 8.10: Dynamic stall. [10, p. 63]

According to Hansen [37, p. 96], the effect of a change in AOA does not appear instantaneously when the blade loads are considered. The change in loads occurs with a time delay which is proportional to the quotient of the chord c and the relative velocity V_{rel} . This change in loads is dependant on whether the boundary layer is attached or partly separated. Hansen [37]

presented a method for approximating the effect of dynamic stall on the lift coefficient based on the Beddoes-Leishman model. Hansen et al. [56, p. 11] state that the basic assumption of the Beddoes-Leishman model with respect to trailing edge separation is that the static lift curve can be expressed as follows; [56, p. 11]

$$C_L^{st}(\alpha) = C_{L,\alpha} \left(\frac{1 + \sqrt{f^{st}(\alpha)}}{2} \right)^2 (\alpha - \alpha_0) \quad (8.2)$$

Where α_0 is the AOA at which C_L^{st} is zero. $C_{L,\alpha}$ is the slope of the lift curve in the linear region which is determined as follows; [56, p. 12]

$$C_{L,\alpha} = \max \left\{ \frac{C_L^{st}(\alpha)}{\alpha - \alpha_0} \right\} \quad (8.3)$$

Furthermore, the function $f^{st}(\alpha)$ determines the separation point for trailing edge separation and can be obtained by inversion of Equation 8.4 when the static lift curve is known; [56, p. 11-12]

$$f^{st}(\alpha) = \left(2 \sqrt{\frac{C_L^{st}(\alpha)}{(\alpha - \alpha_0) C_{L,\alpha}} - 1} \right)^2 \quad (8.4)$$

The weighted averaged wind tunnel data as presented in Figure 7.5a on page 40 was used for the static lift curve.

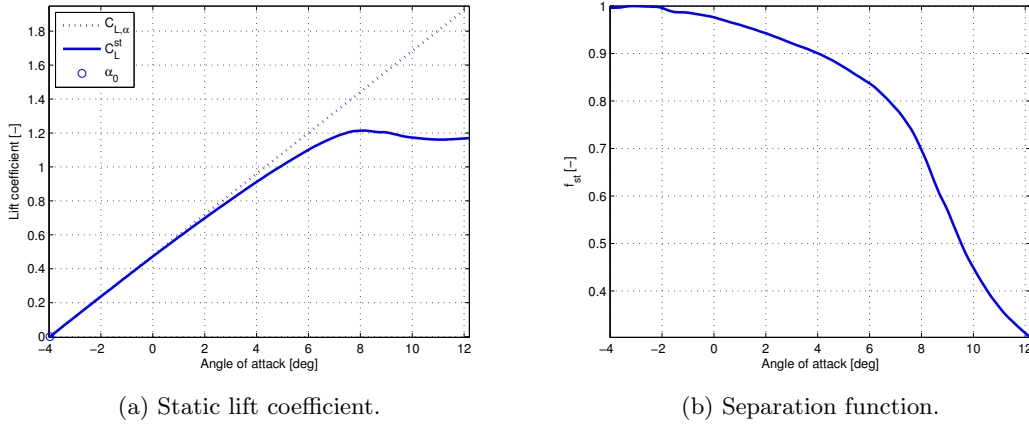


Figure 8.11: Static lift coefficient and separation function

The static lift coefficient and separation function in function of AOA are presented in Figure 8.11.

The dynamic lift coefficient which takes dynamic stall into account is obtained with the following expression; [37, p. 96]

$$C_L(\alpha) = f_s(\alpha - \alpha_0) C_{L,\alpha} + (1 - f_s) C_L^{fs}(\alpha) \quad (8.5)$$

Where the lift coefficient for fully separated flow $C_L^{fs}(\alpha)$ is obtained with; [56, p. 12]

$$C_L^{fs}(\alpha) = \frac{C_L^{st}(\alpha) - (\alpha - \alpha_0)C_{L,\alpha}f^{st}(\alpha)}{1 - f^{st}(\alpha)} \quad (8.6)$$

And the separation function f_s is expressed as follows; [37, p. 96]

$$f_s(t + \Delta t) = f_s^{st}(\alpha) + (f_s(t) - f_s^{st}(\alpha))\exp\left(-\frac{\Delta t}{\tau(t)}\right) \quad (8.7)$$

Where $\tau(t)$ is a time constant which is approximately equal to; [37, p. 96]

$$\tau(t) = \frac{Ac}{V_{rel}(t)} \quad (8.8)$$

Where A is a constant that typically takes a value of 4 according to Hansen [37, p. 96].

The presented Equations were modified to include a changing velocity V_{rel} with time.

The static and dynamic lift coefficient during a gust are compared in Figure 8.12. It can be observed that the impact of dynamic stall is much more profound at high AOA (rated+gust conditions). The maximum static lift coefficient is 1.2149 whereas the maximum dynamic lift coefficient during a gust at rated wind speed is 1.2890, this is a relative increase of 6.10% due to dynamic effects. At low AOA (cutout+gust conditions) the dynamic effect is negligible.

A crude approximation with the BEM method where the static lift coefficient is substituted with the dynamic lift coefficient reveals the approximate change in normal force and torque generation. Please note that the induction factors and Prandtl correction factor correspond to the static lift and drag values. Furthermore, since the presented model does not take drag into account, the static drag coefficients are maintained. Figure 8.13 presents the generated torque and normal force during a gust when the dynamic lift coefficient is adopted. Here, a similar observation can be made; the impact of dynamic stall is large at high AOA and negligible at low AOA.

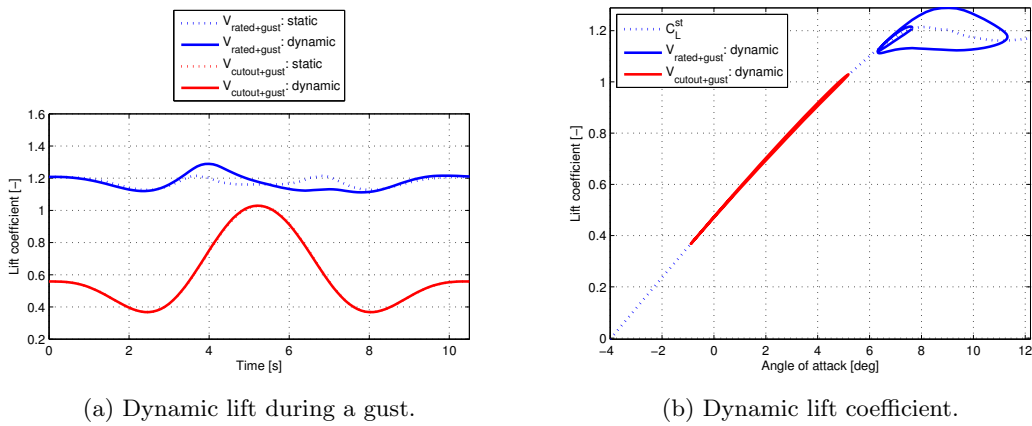


Figure 8.12: Dynamic lift coefficient.

Table 8.4 presents the changes in loads when dynamic effects are taken into account as presented in this Section, the values between brackets are the static values from Table 7.4 on page 42.

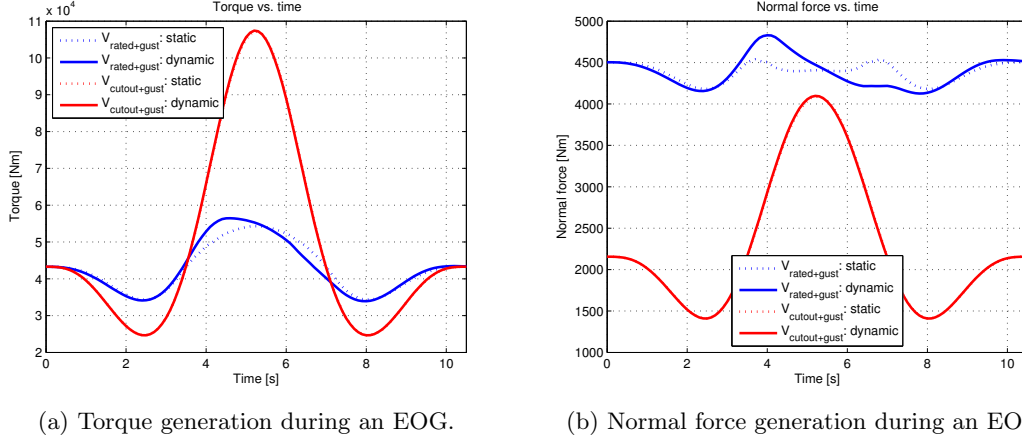


Figure 8.13: Loads generation during an EOG of a blade tip section for various conditions.

From these results it is clear that dynamic stall has an impact when a wind turbine operates at rated conditions. During a gust at rated wind speed, a significant overshoot in the dynamic lift coefficient can be observed. The effects of dynamic stall in cutout conditions are negligible. Unfortunately, this also means that the triggering parameter for morphing, see Table 8.1 on page 50 is not expected to be affected for cutout+gust conditions and hence the triggering parameter is relatively small. The already large triggering parameter for rated+gust conditions is expected to increase when dynamic effects are taken into account.

ΔV_0 [m/s]	ΔT [%]	ΔF_N [%]
4.60 (32.84 %) ($V_{rated+gust}$)	30.50 (25.49)	7.23 (0.71)
6.95 (27.81 %) ($V_{cutout+gust}$)	148.22 (147.58)	90.11 (89.64)

Table 8.4: Change in loads as a result of an EOG (rounded values).

8.5 Control mechanism

After snap-through and morphing has occurred because of a gust, the bi-stable plate has to be restored to its stiff state in order not to compromise power generation. Several actuator types and actuation strategies are found to be suitable to achieve this restoring. Some potential candidates are introduced here.

Conventional electromechanical actuators as used by Kota et al. [22] might be an option, however, it is deemed that they induce a significant weight penalty.

Daynes et al. [21] presented a full-scale helicopter rotor blade section with a bi-stable trailing edge flap which is actuated with electromagnetic actuators.

Barbarino et al. [20] presented a morphing trailing edge concept with SMA actuators. These SMA wires have two phases; an austenite and a martensite phase with different stiffness properties. Upon thermal activation (SMAs contract as the temperature increases), the phase can be changed and an actuation force is exerted as a result of strain recovery. It must be noted that Bilgen et al. [23] found that SMAs are difficult to integrate with bi-stable composites.

Bilgen et al. [23] presented a bi-stable plate with surface bonded PZT actuators. A dynamic control method which makes use of bending resonance induces snap-through of the bi-stable

plate.

Arrieta et al. [24] used surface bonded MFC actuators to restore a bi-stable plate to another state by making use of a dynamic morphing strategy. Bilgen et al. [23] note that snap-through can also be achieved through static excitation.

It is deemed that surface bonded PZT actuators and surface bonded MFC actuators are the best candidates to restore the bi-stable plate to its stiff state

If further research indicates that for example, blade-tower interaction induces unwanted snap-through, it might be possible to use actuators to stiffen the bi-stable plate at the blade-tower-passing instances. Hereby actuation power is only required in a small part of the rotor blade revolution.

Design of morphing airfoil

This Chapter addresses the design of the morphing airfoil.

The bi-stable element is treated in Section 9.1 and corrugated composite laminates are introduced in Section 9.2. The key part of this study, the morphing potential study, is presented in Section 9.3. This Section presents the final flap designs and addresses the steady aerodynamic response of the morphing trailing edge flap. Furthermore, it gives an impression of the unsteady aerodynamic response of a morphing trailing edge.

9.1 Bi-stable element

Bi-stable elements were introduced in Section 2.3.

Kuder et al. [2] designed four distinct embeddable bi-stable laminate configurations, see Figure 9.1. These laminates have a partially non-symmetrical lay-up of unidirectional carbon fibre composite. Bi-stable properties of the laminate were obtained through a curing process with a total temperature difference of 59 K. A high level of stiffness variability of the laminates was achieved. Furthermore, the capability of the short edges of the laminate to be constrained without comprising the bi-stability was ensured.

Kuder et al. [2] found design #3, a laminate with four plies, to be most promising for integration into a profile. This was mainly determined by the edge angle of the plate in the stiff state. Ideally, this angle is close to zero in order for the plate to perform its function optimally when it is integrated in a profile. Therefore, plate design #3 was carried over for this project. This limits the design freedom, however, the goal of this project is not the design of a bi-stable element. The geometric parameters as depicted in Figure 9.1 are specified in Table 9.1.

Kuder et al. [2] noted that a bi-stability loss can be associated with excessive laminate thickness relative to the edge length when the multi-stable behaviour originates from thermally induced stress. Therefore, a thin prepreg material (M40J/739 from North Thin Ply Technology) was used with a nominal ply thickness of 30 μm .

Dr. Arrieta and Kuder reckon that these bi-stable elements are scalable if certain dimension ratio's for length, width and thickness are respected.

For more information on these bi-stable laminates, please refer to the work of Kuder et al. [2].

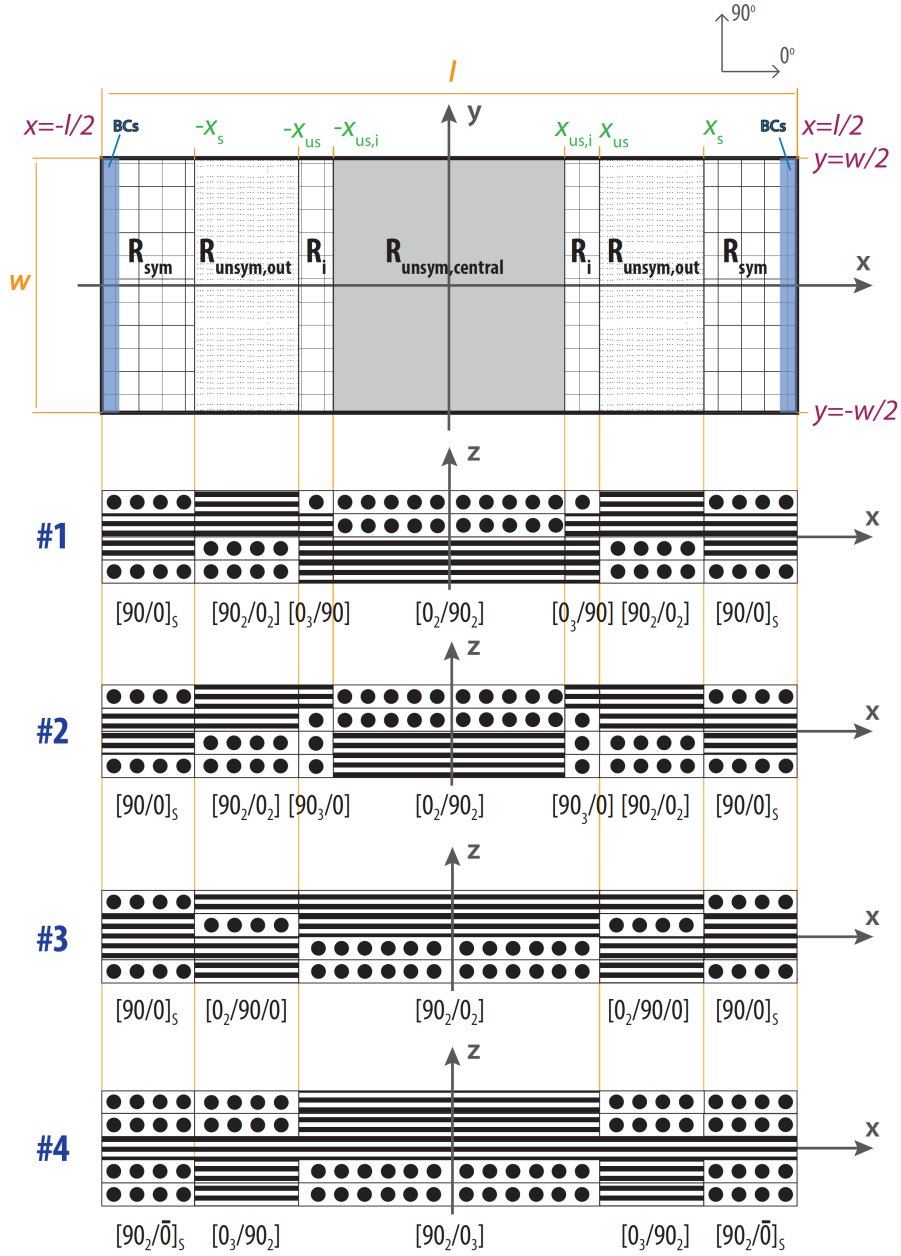


Figure 9.1: Bi-stable plate designs by Kuder et al. [2, p. 3]

Design	w [mm]	l [mm]	x_s [mm]	x_{us} [mm]	$x_{us,i}$ [mm]
#1	50.0	110.0	40.0	30.5	27.5
#2	50.0	110.0	40.0	33.5	30.5
#3	50.0	95.0	34.0	20.0	-
#4	50.0	95.0	37.0	22.0	-

Table 9.1: Geometric parameters of bi-stable plate designs. [2, p. 3]

9.2 Corrugated composite laminates

One of the major obstacles encountered during the design of the morphing airfoil, which is presented in the next Section, arises from the compressive stiffness of the skin of the profile. This resistance to compression of the airfoil skin induces the tendency for the trailing edge to move down when the trailing edge experiences lift when the bi-stable plate is in the flexible state. This behaviour was also experienced by Kuder et al. [2], see Figure 2.5a on page 9. This results in a minimized lift coefficient reduction or even an increase in lift coefficient as can be seen in Figure 2.5b.

It is obvious that this behaviour heavily compromises the effectiveness of the morphing flap. An apparent solution for this problem is the local reduction of the skin (compressive) stiffness to allow for a local skin compression which in turn allows the trailing edge to deflect upwards. Corrugated skins (briefly mentioned in Section 8.2) are good candidates to full fill the purpose of a compressible skin since they are stiff longitudinal to the direction of corrugation and compliant in the transverse direction according to Thill et al. [12, p. 2]. Figure 9.2 presents a corrugated composite skin test specimen. For more general information on corrugated composite laminates please refer to the work of Winkler [11] and Etches et al. [57].

In the scope of this project, an additional benefit of corrugated skins is the potential to achieve higher trailing edge stiffness variability due to a reduction in trailing edge stiffness contribution of the airfoil skin. Furthermore, corrugation overcomes the constraint of keeping the trailing edge deflection small to reduce strain on the structure, see Section 8.1.

Section 9.2.1 deals with the representation of corrugated composite laminates in Abaqus, Section 9.2.2 presents the corrugated skin that is used in the morphing airfoil design and Section 9.2.3 addresses important considerations which originate from the use of corrugated composite laminates.



Figure 9.2: Corrugated composite skin test specimen. [11, p. 119]

9.2.1 Substitute stiffness matrix

Winkler [11] presented a method which represents corrugated composite skins by means of a substitute stiffness matrix. This substitute stiffness matrix is an **ABD** matrix from the Classical Theory of Laminated Plates (CTLTP) which has been adapted to include the effects of corrugation. This **ABD** matrix allows for an easy and effective implementation in Abaqus since loads are directly translated to strains. For more information on the Abaqus script, see Chapter 6.

First, the **ABD** matrix of the laminate is determined after which it can be modified to include the effects of corrugation. The following CTLP Equations from Kress [58] are used to obtain the **ABD** matrix.

The reduced stiffness matrix **Q** is specified as follows;

$$\mathbf{Q} = \begin{bmatrix} Q_{11} & Q_{12} & 0 \\ Q_{12} & Q_{22} & 0 \\ 0 & 0 & Q_{66} \end{bmatrix} \quad (9.1)$$

Where the elements are defined as follows;

$$Q_{11} = \frac{E_1}{1 - \nu_{12}\nu_{21}} \quad (9.2)$$

$$Q_{12} = \frac{\nu_{12}E_2}{1 - \nu_{12}\nu_{21}} = \frac{\nu_{21}E_1}{1 - \nu_{12}\nu_{21}} \quad (9.3)$$

$$Q_{22} = \frac{E_2}{1 - \nu_{12}\nu_{21}} \quad (9.4)$$

$$Q_{66} = G_{12} \quad (9.5)$$

Where E is the materials Young's modulus, G the shear modulus and ν the Poisson's ratio. The transformation matrix **T** is then created;

$$\mathbf{T} = \begin{bmatrix} \cos^2\theta & \sin^2\theta & 2\sin\theta\cos\theta \\ \sin^2\theta & \cos^2\theta & -2\sin\theta\cos\theta \\ -\sin\theta\cos\theta & \sin\theta\cos\theta & \cos^2\theta - \sin^2\theta \end{bmatrix} \quad (9.6)$$

Where θ is the fibre orientation angle.

The reduced stiffness matrix $\tilde{\mathbf{Q}}$ is obtained with the following Equation;

$$\tilde{\mathbf{Q}} = \mathbf{T}^{-1}\mathbf{Q}\mathbf{T}^{-T} \quad (9.7)$$

The **A** matrix is determined with the following Equation;

$$\mathbf{A} = \sum_{k=1}^n \tilde{\mathbf{Q}}(z_k - z_{k-1}) \quad (9.8)$$

Where z_k is the distance from the laminate mid-plane to the bounding plane of the k^{th} layer.

The **B** matrix is zero since only symmetrical laminates are considered.

The **D** matrix is calculated with the following Equation;

$$\mathbf{D} = \frac{1}{3} \sum_{k=1}^n \tilde{\mathbf{Q}}(z_k^3 - z_{k-1}^3) \quad (9.9)$$

The relation between the loads and deformations on a laminated plate is represented by the following Equation;

$$\begin{Bmatrix} \mathbf{N} \\ \mathbf{M} \end{Bmatrix} = \begin{bmatrix} \mathbf{A} & \mathbf{B} \\ \mathbf{B} & \mathbf{D} \end{bmatrix} \begin{Bmatrix} \epsilon^0 \\ \kappa \end{Bmatrix} \quad (9.10)$$

Where $\textit{textbfN}$ and $\textit{textbfM}$ are line loads and are plate deformations. Where the $\textit{textbfA}$ matrix looks as follows;

$$\mathbf{A} = \begin{bmatrix} A_{11} & A_{12} & A_{16} \\ A_{12} & A_{22} & A_{26} \\ A_{16} & A_{26} & A_{66} \end{bmatrix} \quad (9.11)$$

The indices of the $\textit{textbfB}$ and $\textit{textbfD}$ matrix follow the same indices.

These Equations were used to create a code which generates the **ABD** matrix for a given laminate. This **ABD** calculator was validated with several given **ABD** matrices and their corresponding laminate properties.

Now the **ABD** matrix for a given laminate is known, it can be modified with Winkler's [11] method. Winkler [11] defines a unit cell, see Figure 9.3 which depicts the governing parameters of the corrugation. The following Equations and their derivations can be found in Winkler's [11] work, only the required Equations are presented in this Section.

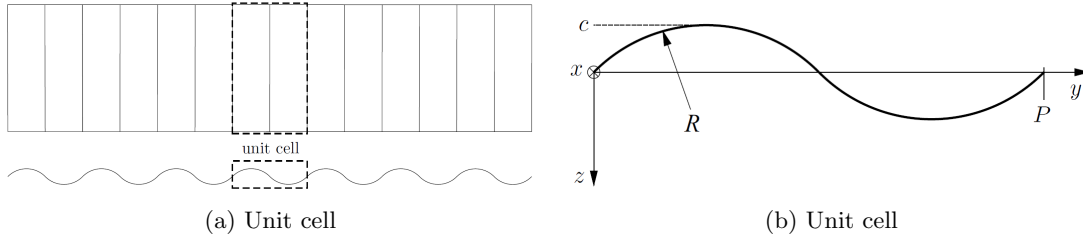


Figure 9.3: Unit cell definition. [11, p. 10-11]

The radius R as defined in Figure 9.3b is determined with the following Equation;

$$R = \frac{16c^2 + P^2}{32c} \quad (9.12)$$

Where c is the half-amplitude and P the period length, see Figure 9.3b. The curvature κ is obtained as follows;

$$\kappa = \frac{1}{R} \quad (9.13)$$

If $c \leq \frac{P}{4}$ then the angle ψ_0 follows from;

$$\psi_0 = \text{asin}\left(\frac{P}{4R}\right) \quad (9.14)$$

The following parameters are required in order to determine the substitute stiffness matrix;

$$K_{22} = 2\psi_0(A_{22}(2 + C^{(2)}) + \kappa^2 D_{22}) + (-3A_{22} + \kappa^2 D_{22})S^{(2)} \quad (9.15)$$

Where $S^{(n)}$ is defined as;

$$S^{(n)} = \sin(n\psi_0) \quad (9.16)$$

And $C^{(n)}$ is defined as;

$$C^{(n)} = \cos(n\psi_0) \quad (9.17)$$

Then the elements of the substitute stiffness matrix $\tilde{\mathbf{A}}\tilde{\mathbf{B}}\tilde{\mathbf{D}}$ can be found with the following Equations;

$$\tilde{A}_{11} = \frac{(A_{11}A_{22} - A_{12}^2)K_{22}\psi_0 + 4\kappa^2 A_{12}^2 D_{22}(S^{(1)})^2}{A_{22}K_{22}S^{(1)}} \quad (9.18)$$

$$\tilde{A}_{12} = \frac{4\kappa^2 D_{22}S^{(1)}}{K_{22}} A_{12} \quad (9.19)$$

$$\tilde{A}_{22} = \frac{4\kappa^2 D_{22}S^{(1)}}{K_{22}} A_{22} \quad (9.20)$$

$$\tilde{A}_{66} = \frac{S^{(1)}}{\psi_0} A_{66} \quad (9.21)$$

$$\begin{aligned} \tilde{D}_{11} = & \frac{2(A_{11}A_{22} - A_{12}^2) \left(\psi_0 + 2\psi_0(C^{(1)})^2 - 3C^{(1)}S^{(1)} \right)}{4\kappa^2 A_{22}S^{(1)}} + \frac{D_{11}(2\psi_0 + S^{(2)})}{4S^{(1)}} \\ & - \frac{D_{12}^2 \left(-4(S^{(1)})^2 + \psi_0(2\psi_0 + S^{(2)}) \right)}{4\psi_0 D_{22}S^{(1)}} \end{aligned} \quad (9.22)$$

$$\tilde{D}_{12} = \frac{S^{(1)}}{\psi_0} D_{12} \quad (9.23)$$

$$\tilde{D}_{22} = \frac{S^{(1)}}{\psi_0} D_{22} \quad (9.24)$$

$$\tilde{D}_{66} = \frac{\psi_0}{S^{(1)}} D_{66} \quad (9.25)$$

The presented Equations were included in the **ABD** calculator. The code was validated with example substitute stiffness matrices given by Winkler [11].

9.2.2 Implementation

The Equations presented in the previous Section are used in this Section to determine the substitute stiffness matrix ($\tilde{\mathbf{A}}\tilde{\mathbf{B}}\tilde{\mathbf{D}}$) of the corrugated skin that is used for the morphing airfoil. In the scope of manufacturability, it is desirable to use the same skin material for the corrugation as for the airfoil skin. Therefore, the airfoil skin material presented by Kuder et al. [2] was examined. The material properties for this glass fibre composite laminate are given in Table 9.2. The layup of the airfoil skin is given in Table 9.3. This layup can be expressed as $[45/-45/0/90]_S$. Daniel and Ishai [59, p. 181] recommend to select a symmetric and balanced layup with fine ply interdispersion whenever possible. This in order to eliminate extension/bending coupling and shear coupling and in order to minimise torsion coupling. Hereby, warping and unexpected distortions are avoided and interlaminar stresses are reduced. Since the laminate by Kuder et al. [2] is symmetric and balanced, the layup was carried over for the corrugated skin.

E_1 [GPa]	E_2 [GPa]	ν_{12} [-]	G_{12} [GPa]	G_{13} [GPa]	G_{23} [GPa]
35	10	0.29	4	4	4.5

Table 9.2: Laminate properties.

Ply	t_{ply} [mm]	θ [deg]
1	0.1	45
2	0.1	-45
3	0.05	90
4	0.05	0
5	0.05	0
6	0.05	90
7	0.1	-45
8	0.1	45

Table 9.3: Layup of airfoil skin.

Winkler [11, p. 69+93] states that the thickness-to-radius ratio should be small (0.01-0.04) in order to allow the use of analytical thin-shell models. This imposes a constraint on the minimum radius of the corrugation for a given laminate. The material by Kuder et al. [2] has an overall thickness of 0.6 mm. With a half-amplitude c of 20 mm and a period P of 100 mm, the radius R is determined to be 25.63 mm with Equation 9.12. This results in a thickness-to-radius ratio of 0.023 which is satisfactory. This constraint however imposes the minimum corrugation size which, for aerodynamic and structural reasons, is preferably as low as possible. The aerodynamic and structural impact of corrugation is addressed in Section 9.2.3.

It must be stated that, in the scope of this project, the response of the corrugated skin was of key importance and the aerodynamic and structural implications were considered less vital. Hence that it may not be technically feasible to manufacture the presented design.

The \mathbf{A} [MPa·mm] and \mathbf{D} [MPa·mm³] matrix for the material by Kuder et al. [2] and $\tilde{\mathbf{A}}$ and $\tilde{\mathbf{D}}$ matrix for the same material with corrugation as defined in this Section are as follows;

$$\mathbf{A} = \begin{bmatrix} 11.4159e3 & 4.1994e3 & 0 \\ 4.1994e3 & 11.4159e3 & 0 \\ 0 & 0 & 4.8165e3 \end{bmatrix} \quad (9.26)$$

$$\tilde{\mathbf{A}} = \begin{bmatrix} 13.6541e3 & 413.4799e-3 & 0 \\ 413.4799e-3 & 1.1240 & 0 \\ 0 & 0 & 3.4821e3 \end{bmatrix} \quad (9.27)$$

$$\mathbf{D} = \begin{bmatrix} 316.6596 & 158.2006 & 51.2310 \\ 158.2006 & 303.8518 & 51.2310 \\ 51.2310 & 51.2310 & 176.7155 \end{bmatrix} \quad (9.28)$$

$$\tilde{\mathbf{D}} = \begin{bmatrix} 2.7809e6 & 114.3714 & 0 \\ 114.3714 & 228.9295 & 0 \\ 0 & 0 & 244.4362 \end{bmatrix} \quad (9.29)$$

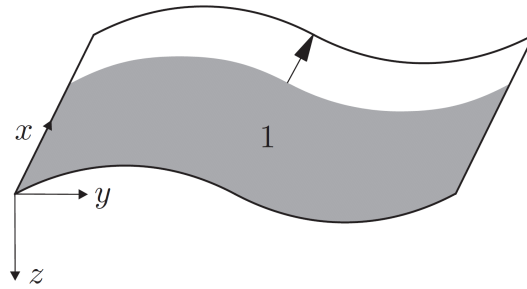


Figure 9.4: Axis system for corrugation according to Winkler. [11, p. 13]

Figure 9.4 depicts the axis system with respect to the corrugation. The following observations can be made from the \mathbf{A} and \mathbf{D} matrices;

- Increase in A_{11} since more material per length due to the corrugation, hence more force required to compress a given length of material. This means that the corrugation increases the stiffness in the x direction.
- Reduction in A_{22} , this means that the corrugation reduces the stiffness in the y direction.
- Increase in D_{11} , analogy with area moment of inertia since the height is increased.

In order for the corrugated skin and laminate to be oriented as desired in the Abaqus model, three steps were required. First, the \mathbf{ABD} matrix of the laminate with a 90° counter-clockwise rotation of the layup is created. Next, the \mathbf{ABD} matrix is modified to include the effects of corrugation. Then, the obtained $\tilde{\mathbf{A}}\tilde{\mathbf{B}}\tilde{\mathbf{D}}$ matrix is specified in Abaqus. Finally, the material direction in Abaqus is rotated 90° clockwise to obtain the desired laminate as well as corrugation orientation. Hence the stiffness of the airfoil skin is locally reduced in chord-wise direction.

The \mathbf{ABD} procedure and the impact of corrugation was tested in Abaqus with a simple compression test. Three cases were considered. In all cases, a flat plate was created which measured 100 mm by 50 mm. One short side was clamped and at the other short side, a load of 1 N in compressive direction was applied.

For case 1, the material defined by Kuder et al. [2], see Table 9.2 and 9.3 was defined as a laminate with the given properties in Abaqus. For case 2, the material properties in Abaqus were specified by means of an \mathbf{ABD} matrix. The \mathbf{A} (9.26) and \mathbf{D} (9.28) matrix which correspond to the same laminate as case 1 were specified in Abaqus. Similarly for case 3, the $\tilde{\mathbf{A}}$ (9.27)

Case	Displacement [mm]
Case 1: Composite lay-up	1.00700e-2
Case 2: Composite ABD	1.00729e-2
Case 3: Corrugated composite ABD	2.22422e2

Table 9.4: Corrugation compression test results.

and $\tilde{\mathbf{D}}$ (9.29) matrix which correspond to the same laminate as case 1 in corrugated state were specified in order to assess the impact of corrugation.

The results of the compression test in terms of compressive displacement for all three cases are summarized in Table 9.4. The displacements for case 1 and case 2 are nearly identical. These results validate the usage of an **ABD** matrix to represent a laminate in Abaqus. The response of case 3 illustrates the drastic decrease in compressive stiffness of a corrugated laminate compared to a flat laminate. It must be noted that an **ABD** matrix does not take into account any non-linearities and thus caution must be taken when interpreting results. In this case, the compressive displacement of the corrugated skin exceeds the length of the panel. This indicates that the compressive force of 1 N is too high for the corrugated skin panel response to be in the linear region.

9.2.3 Design considerations

Certain aspects need to be taken into account when using corrugated skins for airfoil. The most important aspects are treated in this Section.

According to Winkler [11, p. 5-6], corrugations are generally disadvantageous for aerodynamic performance. However, by using a low height and low period length the disadvantages can be mitigated to a large degree. Furthermore, recessed corrugations show promise at high Reynolds numbers through a minimal aerodynamic impact.

Thill et al. [12] concluded that corrugations result in an increase in friction drag. However, they believe that especially for thicker airfoils, where the pressure drag dominates, this becomes less important.

Xia et al. [60] investigated the two-dimensional aerodynamic effect of corrugation on an airfoil. They found that the slope of the lift curve ($dC_l/d\alpha$) decreased and the minimum drag coefficient (C_{d0}) increased with increasing size of corrugation. Furthermore, they found that eddies fill the troughs of the corrugation and 'smooth' the airfoil profile making the flow outside the corrugation similar to that of an airfoil without corrugation.

Since turbulent flow remains attached for longer compared to laminar flow ([61, p. 719]) and the corrugated skin is located near the trailing edge, a region where normally a turbulent boundary layer is present, the chance of flow separation due to corrugation and hence the impact on the aerodynamic performance, is minimised.

Thill et al. [12] presented a corrugated panel with a segmented skin to reduce the aerodynamic impact, see Figure 9.5.

Another option could be to fill the corrugation with a compressible foam to reduce the surface roughness and thus the impact of the corrugated skin on the aerodynamic performance.

The corrugation on the top skin of the trailing edge flap has an impact on the local pressure distribution and thus on the flap hinge moment. This impact is not taken into account in this project. However, it is expected that this impact is minimal since the main contribution to the flap hinge moment is generated by the high pressure area which acts on the pressure side of the

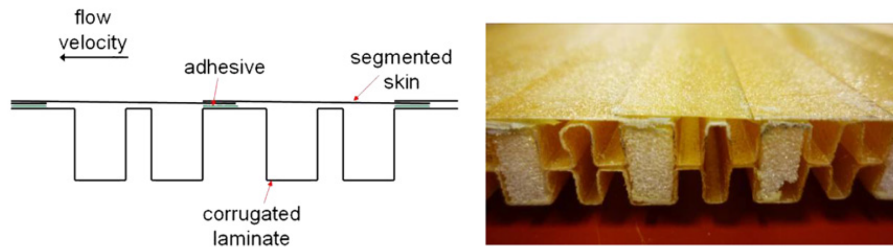


Figure 9.5: Segmented skin by Thill et al. [12, p. 6]

profile, see the pressure distributions in Figure 5.2 on page 24. Thus it is assumed that the flap hinge moment remains relatively unaffected by adding corrugation on the suction side of the profile. Note that this might be different for other airfoils which have another camber profile (e.g. symmetric airfoils).

Since the substitute stiffness ($\tilde{\mathbf{A}}\tilde{\mathbf{B}}\tilde{\mathbf{D}}$) matrix is a representation of the corrugated skin and does only represent the corrugated skin in terms of linear structural response, some considerations need to be taken into account.

The maximum compression/strain of the corrugated skin must be watched carefully in order for the response to be in the linear region. This because non-linear effects are not taken into account and hence the $\tilde{\mathbf{A}}\tilde{\mathbf{B}}\tilde{\mathbf{D}}$ matrix response is only valid in the linear region. Dr. Arrieta recommends using a maximum strain constraint of 20% on the corrugated skin in order to avoid a highly non-linear structural response.

Furthermore, the thickness-to-radius ratio must be watched as mentioned in the previous Section since Winkler's [11, p. 69+93] model is based on the assumption of thin walled structures.

An important manufacturability aspect is the clearance between the corrugated skin and the bi-stable plate, it must be ensured that they do not clash. It is therefore desirable to locate the corrugated skin as much aft as possible since the bi-stable plate proximity to the top skin of the profile increases with increasing distance from the trailing edge. This statement is only valid when the trailing edge flap region is considered with a geometry based on that presented in Figure 8.2 on page 48. Since the bi-stable plate deflects downwards in the flexible state, the clearance between the corrugated skin and the bi-stable element increases during morphing.

Another aspect that must not be disregarded is the bending stiffness distribution along the airfoil in order not to attract too much stress in flapwise and edgewise bending. Therefore, it is desirable for the corrugated skin not to have an increased bending stiffness compared to the regular airfoil skin in edgewise and flapwise bending.

It must be noted that the corrugated skin used in this project is not optimal in terms of sizing and laminate properties. However, in the scope of this project, the structural response of the corrugated skin was the dominant driver for this initial study and hence it is accepted that the corrugated skin is not optimal in terms of aerodynamic performance and manufacturability.

9.3 Morphing potential study

In this Section, the load alleviation potential of a bi-stable morphing trailing edge flap is addressed.

The design restrictions and approach are outlined in Section 9.3.1. The final designs for a small and a large flap are presented in Section 9.3.2. The steady response of the morphing flaps is presented in Section 9.3.3. In the same Section, the effectiveness of the bi-stable mechanism is

evaluated by comparing the response of a bi-stable flap with an identical flap without bi-stable element. The aerodynamic response of an instantaneously morphing flap is briefly presented in Section 9.3.4.

9.3.1 Design restrictions and approach

The purpose of the design of a bi-stable morphing flap is to address the load alleviation potential of this novel morphing method. In order to get a better impression of this load alleviation potential, a small and large flap are designed. The small and large flap lengths are set at approximately 10% and 20% of the chord since it is shown in Figure 8.4 on page 49 that flaps of these lengths have a desirable flap hinge moment or 'triggering parameter' response and can potentially alleviate a significant amount of load as is presented in Section 8.3.

Again, two flow conditions were considered, expressed as V_1 and V_2 . V_1 means that the AOA, Mach number and Reynolds number are those corresponding to $V_{rated+gust}$, V_2 means that the aforementioned parameters are corresponding to $V_{cutout+gust}$. The relative velocity is variable in order to identify the velocity response of the morphing flaps.

The most important design restriction originates from the bi-stable plate which is fixed, see Section 9.1. This results in a challenge with respect to designing two flaps of different size with the same bi-stable element. Different flap lengths are investigated by changing the chord length whilst the absolute flap length is kept roughly the same. When only the flap is considered, this means that there is a change in shape and pressure distribution. The material properties and thickness are kept the same as well as the flow conditions. This makes that the flow conditions are equal whilst the material loading and stresses are roughly the same although two flaps of different length are considered. This 'flap-only' approach is justified since the part in front of the flap is clamped, see Section 6.1.3, and hence does not deform under loading.

The design approach consists of an iterative design process in which one reasoned design change is made at a time with the focus of improving one specific aspect of the design. Hence the design process was time consuming, however, trial-and-error was avoided.

9.3.2 Final morphing flap designs

After over 20 design iterations, two satisfactory flap designs were obtained. The first designs did not feature a corrugated skin and exhibited an increase in lift coefficient after snap-through. Kuder et al. [2] experienced a similar response. This response is explained in more detail in the next Section and illustrates the necessity of a compressible skin.

It must be noted that these flap designs are not fully optimised for maximal load alleviation since each design iteration requires a computationally expensive simulation. Hence there is room for improvement in terms of alleviated load.

The chord length c , corrugation length $l_{corrugation}$, pressure/lower side flap length l_{flap_lower} , suction/upper side flap length l_{flap_upper} and averaged flap length $l_{flap_average}$ of the final flap designs are presented in Table 9.5. The reason behind the difference in lower side flap length and upper side flap length is addressed in Section 9.3.3. Furthermore it must be mentioned that the design freedom is limited since webs can only be defined from a discrete number of panel edges along the airfoil. Similarly, the corrugated skin can only be assigned to one or more panel(s) which are defined by the airfoil coordinates. Hence why the percentages given in Table 9.5 are not round numbers.

The final, undeformed flap designs can be seen in Figure 9.6 and 9.7. The green and red area

are composed of the laminate by Kuder et al. [2] as described in Table 9.2 and 9.3. The flanges to which the bi-stable plate is attached are represented by the red panels, the light grey area represents the corrugated skin and the dark grey area represents the bi-stable plate.

Flap	c [mm]	$l_{corrugation}$ [%c]	l_{flap_lower} [%c]	l_{flap_upper} [%c]	$l_{flap_average}$ [%c]
Small	1000	7.08	12.28	14.10	13.19
Large	500	11.11	17.05	24.14	20.59

Table 9.5: Morphing flap properties.

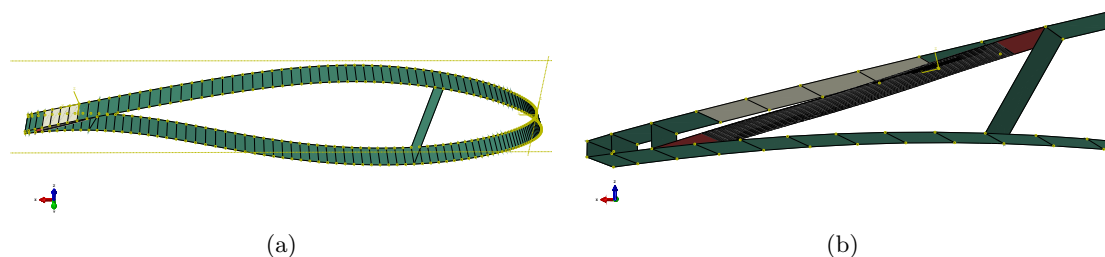


Figure 9.6: Small flap design.

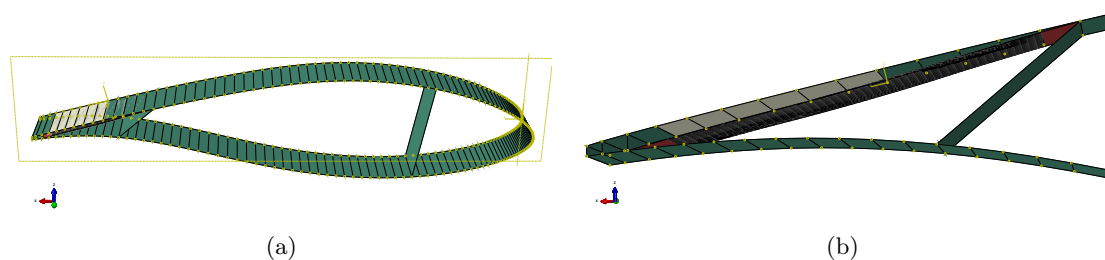


Figure 9.7: Large flap design.

9.3.3 Steady response of morphing flap

The steady response of both flap designs is examined for conditions V_1 and V_2 . The presented aerodynamic results in this Section are from XFOIL and for forced boundary layer transition at 5% chord at the suction side. This to assure consistency between the data which is used during the aeroelastic calculations and the data that is presented in this Section.

Morphing behaviour

Figure 9.8 and 9.9 present Abaqus results of respectively the small and large flap before and after snap-through for conditions at V_1 .

Figures (a) and (c) display the Von Mises stresses, please note that the grey area corresponds to the corrugated skin represented by an $\tilde{\mathbf{A}}\tilde{\mathbf{B}}\tilde{\mathbf{D}}$ matrix which makes that only strain and no stress data is known. Notice the stress field in the bi-stable plate with stress concentrations near the edges. These stresses arise during curing of the (non-symmetrical) laminate and induce the

bi-stable properties.

Figures (b) and (d) display the vertical displacement. Observe that the trailing edge deflects downward before snap-through occurs, this behaviour is discussed in more detail later in this Section.

These Figures are only given for V_1 conditions, however, the results at V_2 conditions were found to be very similar.

The velocities at which snap-through and morphing occur are summarized in Table 9.6 on page 71. The velocities in brackets correspond to the morphing velocities when rated (V_{01}) and cutout (V_{02}) conditions (Reynolds number, Mach number and AOA) are considered. It must be stressed that these values do not fall in the range of velocities as presented in Table 7.2 on page 39. This because the design freedom (bi-stable plate, airfoil skin material, chord length) was limited. However, it is deemed that with more design freedom, the morphing velocity can be altered easily. Furthermore it must be noted that the relative differences between the morphing velocities are very important. A higher difference between the normal (V_{0x}) and gust (V_x) values indicates a robust system which is less likely to experience unintended snap-through. Unintended snap-through means that snap-through occurs during normal operating conditions, which is not desired. It must be noted that for cutout+gust (V_2) conditions, the triggering of the small flap mostly results from an increase in relative velocity rather than a change in AOA. However, as shown in Table 7.4 on page 42 the relative velocity increase due to an EOG is significant in the aforementioned case. Hence, unintended snap-through is not expected.

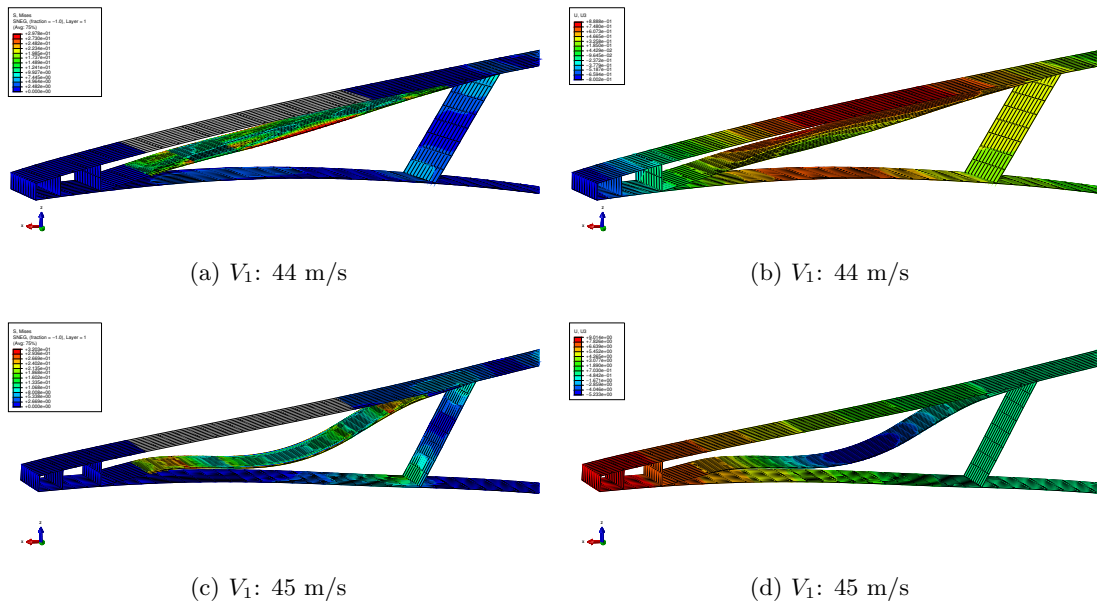


Figure 9.8: Small flap before and after snap-through.

Flap	V_1 (V_{01}) [m/s]	V_2 (V_{02}) [m/s]
Small	44-45 (47-48)	47-48 (47-48)
Large	50-51 (53-54)	53-54 (54-55)

Table 9.6: Morphing velocity.

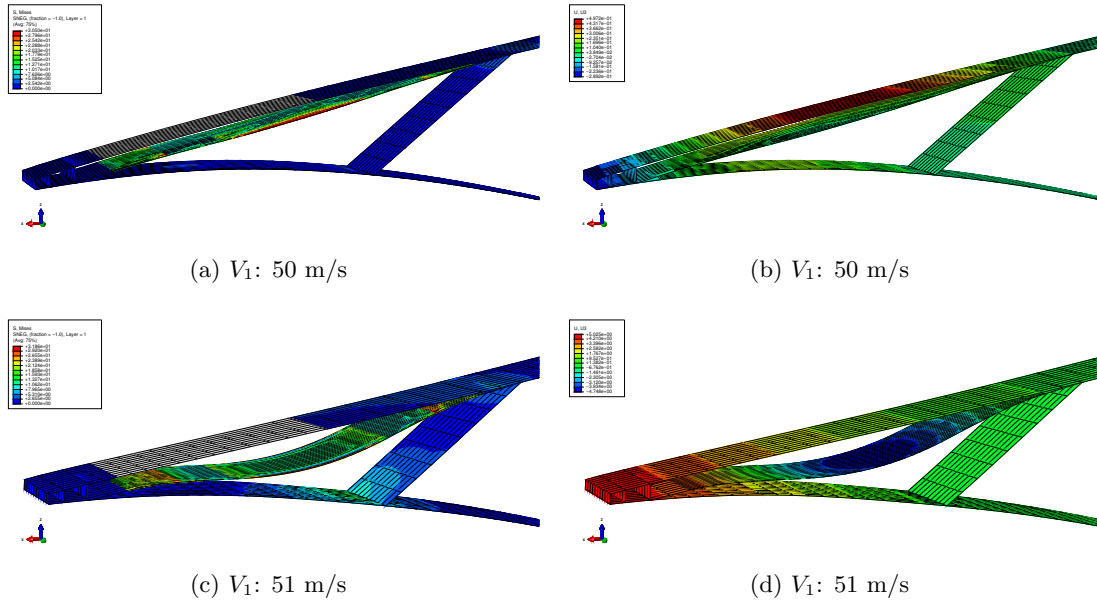


Figure 9.9: Large flap before and after snap-through.

The trailing edge flap contours for the small and large flap are plotted for V_1 and V_2 conditions in Figure 9.10 and 9.11 respectively. The velocities correspond to the upper limit of the morphing velocity interval as presented in Table 9.6. The undeformed reference airfoil (black) as well as a parametric flap (red) as presented in Section 8.3 are plotted as well for comparative purposes. If the small morphing flap is compared with the parametric flap of $0.1c$ and 5° , it can be observed that the flap angle of the morphing flap is close to 5° . However, if the large morphing flap is compared with the parametric flap of $0.2c$ and 5° , it can be observed that the flap angle is much less than 5° .

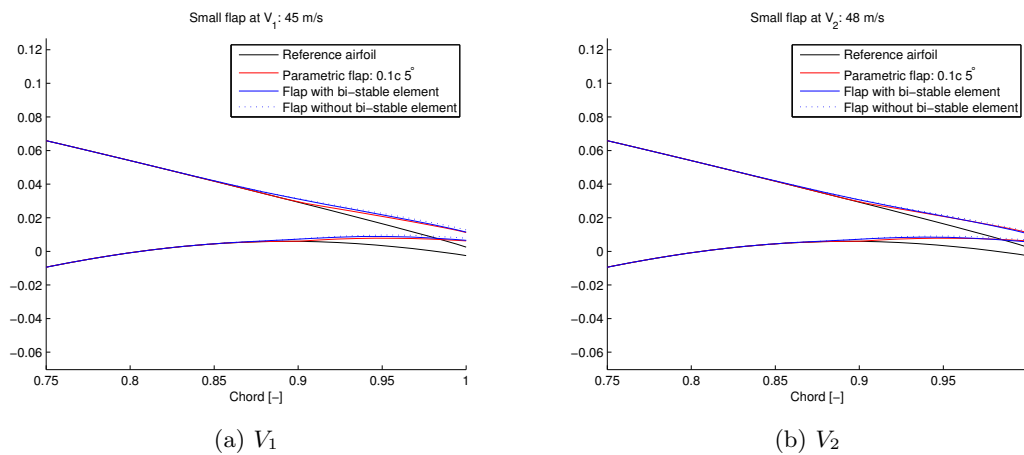


Figure 9.10: Small flap deflection.

Figure 9.12 reveals the impact of a morphing trailing edge flap on the pressure distribution. It can be observed that the local pressure coefficient is reduced marginally over the entire chord at V_1 conditions (high AOA). Minor differences between the small and large flap pressure dis-

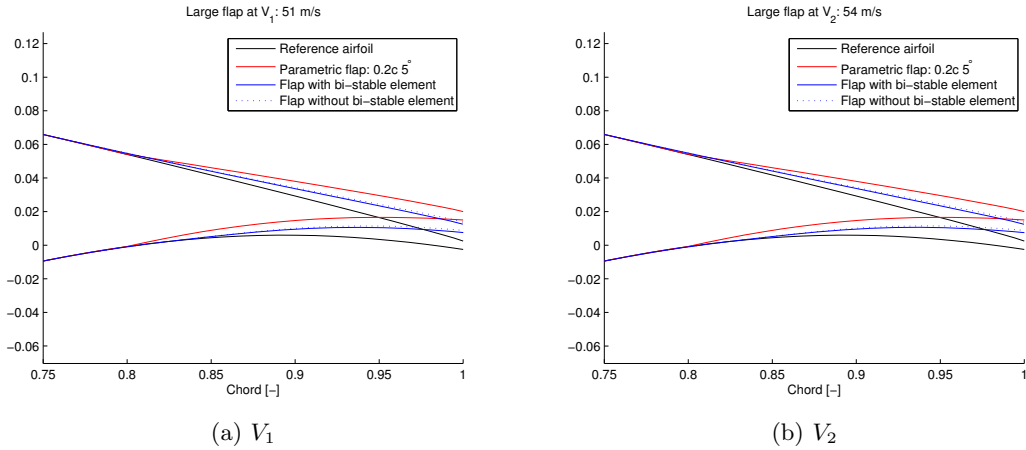


Figure 9.11: Large flap deflection.

tribution are present near the trailing edge.

At V_2 conditions (low AOA), the reduction is more significant and relatively constant along the chord. Again, the pressure distributions for the small and large flap are very similar. However, the small flap alleviates more load near the trailing edge compared to the small flap.

García [62, p. 110] made a similar observation; trailing edge flaps influence the pressure distribution across the entire airfoil and not only locally in the trailing edge region.

It must be stressed that the flap angle is determined only by the structure and its interaction with the flow. The small flap achieves a higher deflection angle and alleviates a similar amount of load compared to the large flap. This indicates that the small flap is more effective for passive load alleviation. Similarly, Troldborg [44] found that small flaps are more effective compared to large flaps.

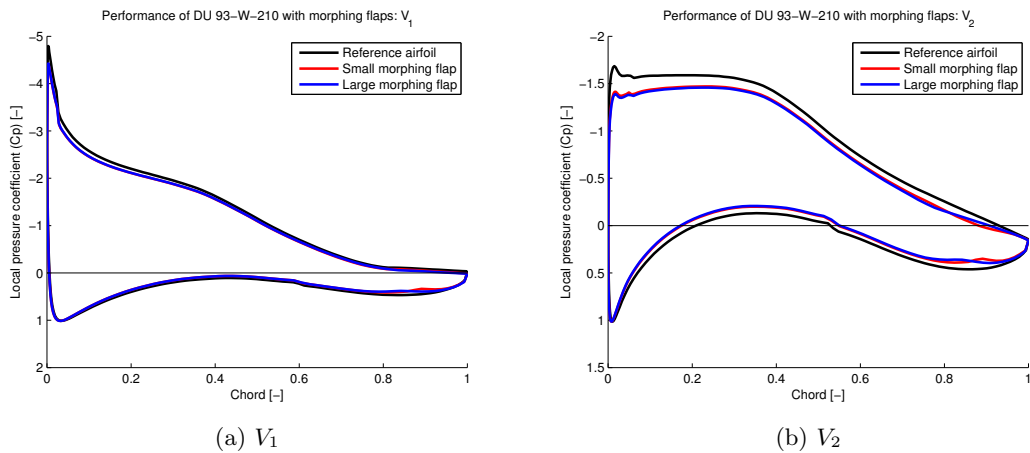


Figure 9.12: Pressure distributions of morphed airfoils.

Table 9.7 summarises the reduction in lift and drag coefficient compared to the reference airfoil as well as the compression of the corrugated skin. The presented values hold for the upper limits of the morphing velocity intervals presented in Table 9.6. Furthermore, this Table presents a comparison between a passive morphing flap and a passive bi-stable morphing flap in order to show the efficiency of the bi-stable mechanism. The flaps labelled as 'small' and 'large' have the

same designs as presented earlier with the only modification being the removal of the bi-stable plate. It can be observed that the differences between the flaps with and without bi-stable plate is small. This indicates that the bi-stable 'restraining mechanism' provides little resistance to flap rotation when the bi-stable plate is in the flexible state and thus is very efficient.

Furthermore, it can be observed that the compression of the corrugated skin remains under 3% for the final design. This indicates that the total length of implemented corrugation can be drastically reduced since the corrugation can be compressed up to 20% as stated in Section 9.2.3.

Flap	$\Delta C_l V_1$ [%]	$\Delta C_l V_2$ [%]	$\Delta C_d V_1$ [%]	$\Delta C_d V_2$ [%]	$\Delta l_{corr} V_1$ [%]	$\Delta l_{corr} V_2$ [%]
Small bi-stable	-6.60	-14.47	-13.47	-7.36	-2.95	-2.66
Small	-7.58	-16.54	-15.06	-7.81	-3.37	-3.04
Large bi-stable	-6.28	-15.51	-16.74	-7.90	-2.25	-2.24
Large	-7.08	-17.57	-18.63	-8.72	-2.55	-2.55

Table 9.7: *Effect of morphing flaps on lift and drag coefficients and corrugation in gust conditions.*

Finally, an overlay of the deformed and undeformed shape of both flap designs is presented in Figure 9.13 and 9.14.

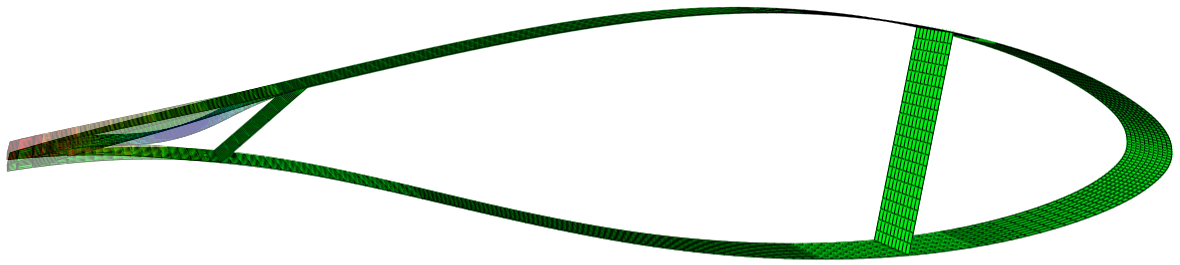


Figure 9.13: Overlay of morphed and undeformed airfoil with large flap.

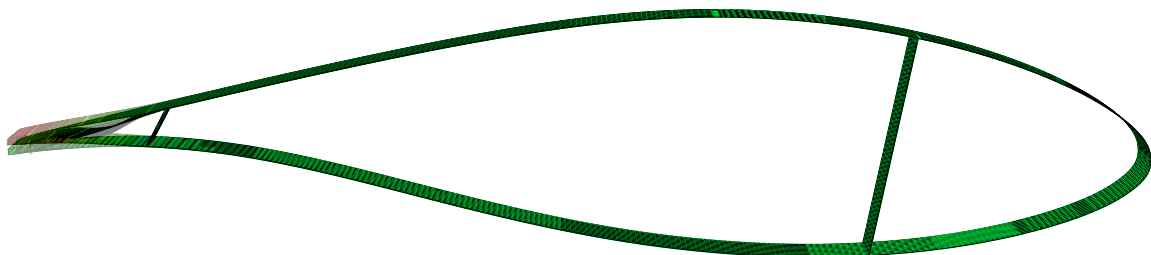


Figure 9.14: Overlay of morphed and undeformed airfoil with small flap.

Velocity response

Since the morphing trailing edge flap responds passively to the flow, it is important to get an insight in its behaviour by examining the response across a wide range of operating conditions. This so-called 'velocity response' is assessed at V_1 and V_2 conditions for a wide range of relative velocities by four parameters; trailing edge deflection, approximate flap angle, lift coefficient and drag coefficient.

The trailing edge deflection in function of velocity is presented in Figure 9.15 on page 78. It can be observed that the trailing edge deflects downward in the pre-snap-through region, this behaviour is explained later on in this Section. During snap-through, there is an instantaneous upward deflection of the trailing edge. In the post-snap-through region, the trailing edge deflection increases as the velocity increases.

The trailing edge deflection as a result of a velocity change dz_{TE}/dV can be regarded to be a measure for the morphing flap deflection behaviour in pre-snap-through as well as post-snap-through conditions. From Figure 9.15, it can be observed that the trailing edge deflection behaves relatively linear with velocity in the pre-snap-through and post-snap-through region. This justifies the approach of taking the first derivative of trailing edge deflection in function of velocity as a measure of expressing the deflection behaviour. The pre- and post-snap-through derivatives are summarised in Table 9.8. It can be observed that both flap designs have a relatively similar behaviour. The large flap deflects less (downward) in the pre-snap-through region compared to the small flap and hence behaves more rigid. In the post-snap-through region, the derivative is significantly larger in absolute terms compared to the pre-snap-through region which indicates a more compliant behaviour.

Flap	Condition	Pre-snap-through dz_{TE}/dV [%c/(m/s)]	Post-snap-through dz_{TE}/dV [%c/(m/s)]
Small	V_1	-0.0020	0.0356
Small	V_2	-0.0021	0.0275
Large	V_1	-0.0012	0.0352
Large	V_2	-0.0015	0.0313

Table 9.8: Trailing edge deflection as a result of velocity change.

The approximate flap angle in function of velocity is directly related to the trailing edge displacement and is presented in Figure 9.16 on page 78. Unsurprisingly, the response of the flap angle is very similar to that of the trailing edge deflection. It can be observed that the flap angle of the small flap is significantly larger compared to the large flap. This difference originates from the trailing edge displacement's being relatively similar for both flap designs whilst their flap lengths are significantly different. In turn, this results from a difference in flap hinge moment as explained in Section 8.2. This because a higher flap hinge moment difference during snap-through leads to a large flap rotation angle.

As was found in Section 8.3, the flap angle is a dominant factor when lift reduction is considered. The difference in flap angle manifests itself in the lift coefficient, which is presented in function of velocity in Figure 9.17 on page 79. It can be observed that the lift coefficient increases in the pre-snap-through region, drops instantly during snap-through and continues to drop post-snap-through.

Table 9.9 presents the relative change in lift coefficient before and during snap-through. The change before snap-through is determined by the increase in lift coefficient from a velocity of 5 m/s up to the lower limit of the snap-through velocity, see Table 9.6 on page 71. It can be observed that when the lift coefficient change is considered before snap-through, there is a

small difference between the small and the large flap. The airfoil with a small flap experiences a higher increase in lift coefficient in the region before snap-through. During snap-through, the lift reduction of both flaps is very similar. At V_2 conditions the lift reduction is significantly higher compared to at V_1 conditions, hence the load alleviation potential is higher at low AOA and hence the influence of a flap is smaller in separated flow conditions. The relative reduction in lift coefficient in Table 9.9 is the instantaneous drop, so the difference between the lift coefficient right before and right after snap-through. It is believed that this instantaneous drop expresses the load alleviation potential together with the lift reduction in the post-snap-through region. The instantaneous drop is used since pitch regulated wind turbines regulate power by pitching the blades and hence accommodate for the increase in lift coefficient in the pre-snap-through region. This makes that the instantaneous load reduction in case of a gust, under the assumption that the blade pitch does not change, is determined by the difference between the pre- and post-snap-through lift coefficient.

The instantaneous lift reduction values of both flap designs are very similar, although slightly higher, compared to those of the parametric flap of $0.1c$ with a flap angle of 5° , see Table 8.2 on page 52. Therefore, the instantaneous reduction in loads is expected to be very similar and slightly higher compared to the reduction in loads by the aforementioned parametric flap, see Table 8.3 on page 52.

The post-snap-through reduction in lift coefficient with increasing velocity is similar for both flaps. Hence as the relative velocity increases further, the lift coefficient is reduced even more. This implies that the exact load alleviation potential depends on the difference in relative velocity in normal and load alleviating conditions. However, the minimum load alleviation potential corresponds to the instantaneous reduction in lift coefficient during snap-through as presented in Table 9.9.

Flap	Condition	Pre-snap-through dCl [%]	Snap-through dCl [%]
Small	V_1	1.41	-7.92
Small	V_2	3.33	-17.26
Large	V_1	0.93	-7.15
Large	V_2	2.70	-17.74

Table 9.9: Lift coefficient change before and during snap-through. (rounded values)

Since the lift coefficient increases in the pre-snap-through region, it is important to assess the aerodynamic efficiency of the airfoil as an increase in lift coefficient might come at the cost of increased drag and hence might reduce the rotor efficiency and thus power generation. The profile drag coefficient and pressure drag coefficient are presented in Figure 9.18 on page 79 in function of velocity. According to Anderson [61, p. 718] there are two types of drag which are produced by viscosity effects; skin friction drag and pressure drag. Skin friction drag originates from the integral of the shear stress over the body in the drag direction. Pressure drag originates from the integral of the pressure distribution over the body in the drag direction. The physical reason behind pressure drag is flow separation. The sum of pressure drag and skin friction drag is called profile drag.

From Figure 9.18 it is apparent that the drag coefficient increases slightly in the pre-snap-through region, instantaneously drops during snap-through and decreases further in the post-snap-through region. Furthermore, it can be observed that the changes in profile drag are due to a change in pressure drag and hence due to flow separation.

In general, it is believed that the increase in lift coefficient and the minor increase in drag coefficient do not negatively impact the rotor efficiency and hence power production is not

compromised.

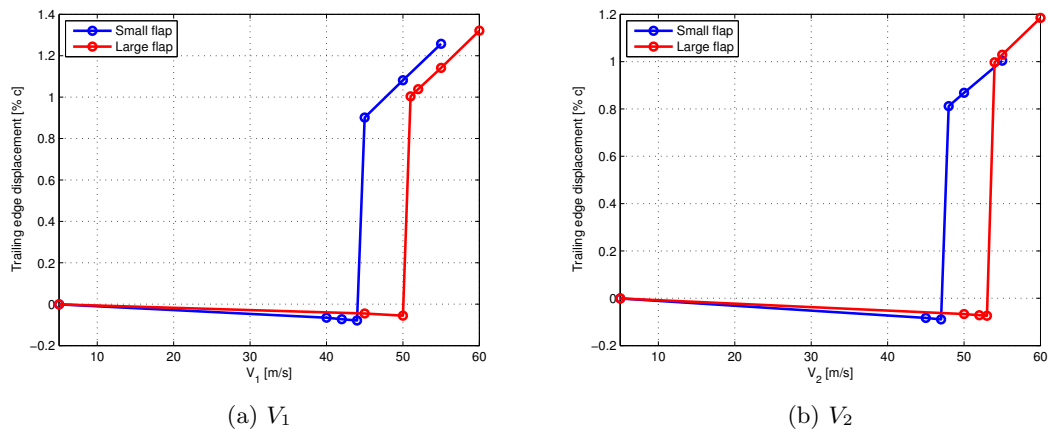


Figure 9.15: Trailing edge displacement in function of velocity.

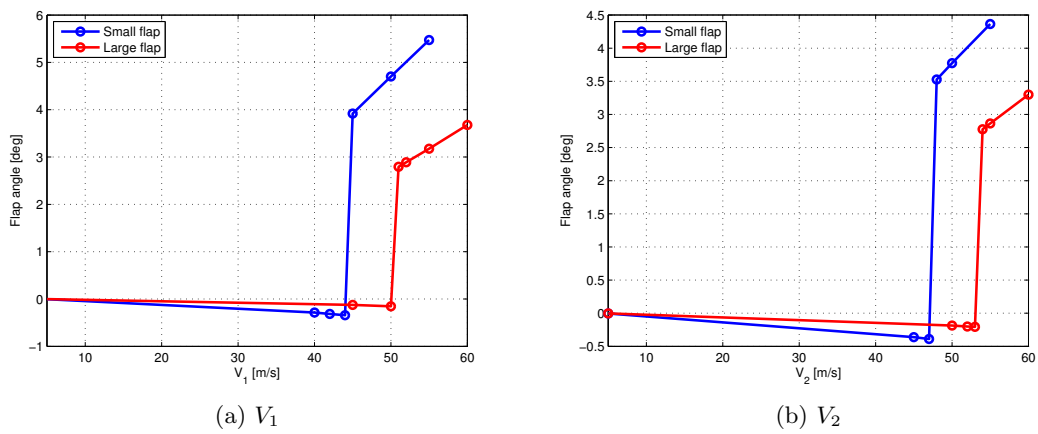


Figure 9.16: Approximate flap angle in function of velocity.

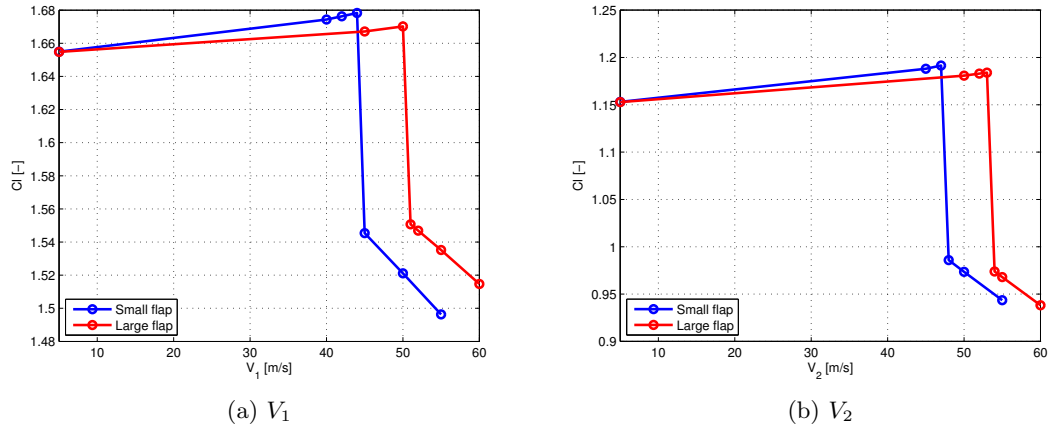


Figure 9.17: Lift coefficient in function of velocity.

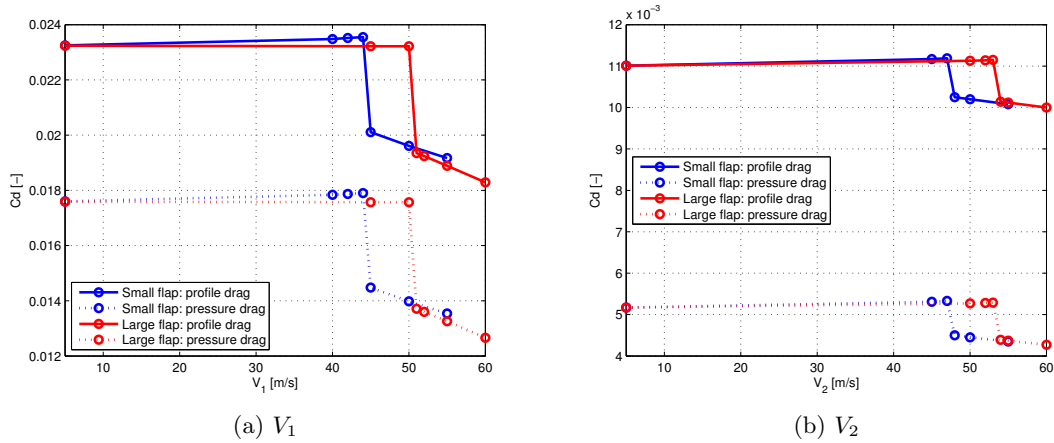


Figure 9.18: Drag coefficient in function of velocity.

Particularities

Two particularities in the behaviour of a morphing bi-stable flap are discussed.

As can be observed in Figure 9.15, the trailing edge has a tendency to deflect downwards in the pre-snap-through region. Observing Figure 9.8b and Figure 9.9b, where the blue areas indicate a downward deflection, it can be concluded that only the aft area of the trailing edge flap deflects downward whilst the middle area deflects upward. Figure 9.19 shows a simplified representation of the trailing edge deflection in the pre-snap-through region. The bi-stable plate and vertical web (dotted lines) are assumed to be infinitely stiff and the pressure side of the trailing edge flap, which is assumed to be flexible, is supported by both of them at the bending points (black dots). The pressure distribution is simplified to a discrete lift force L_{TE} which acts in between the bending points on the pressure side of the flap. Observe that there is an analogy with a three point bending beam. The discrete force induces an upward deflection of the trailing edge skin in between the two bending points. This induces a downward deflection of the skin aft of the most rearward bending point. The part aft of this rearward point is short compared to the flap length and this explains why the trailing edge is not forced upwards by

the aerodynamic load on the aft part. Hence the trailing edge deflection results from a loaded skin which is supported at two points and has an extending part.

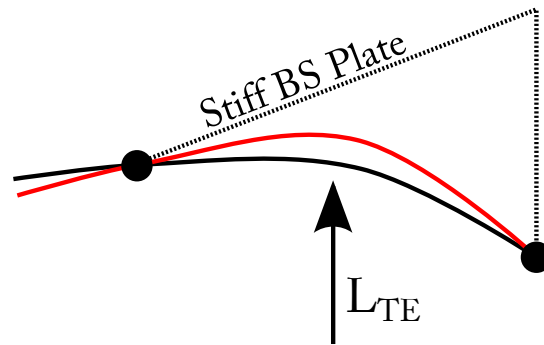


Figure 9.19: Simplified representation of trailing edge deflection.

From the final designs as shown in Figure 9.6 and 9.6 on page 70, it can be observed that the web forward of the bi-stable plate is not vertical. The lower part of this web is located more aft than the upper part. With a vertical web, it was found that the bi-stable plate could go into a buckling mode instead of into the flexible state. Figure 9.20, which is based on Figure 9.19, illustrates this behaviour. Again, a discrete lift force L_{TE} acts on a supported skin which causes it to deflect upward in between both bending points. The pressure side of the trailing edge skin is assumed flexible but inextensible. Hence the upward deflection of the skin must induce a reduction in length dx between both bending points. Another phenomenon that can be observed is that the skin rotates forward of the aft bending point. This rotation together with the lateral compression induces a moment M_{BS} to the bi-stable plate. It is found that bi-stable plates of the type used are sensitive to moment introduction. A moment introduction like presented in Figure 9.20 can force the bi-stable plate into a buckling mode. This behaviour was experienced in several design iteration and was mitigated by reducing the distance between both bending points, hence the angle from vertical of the web forward of the bi-stable plate. This resulted in less upward deflection and less lateral shortening of the skin which in turn resulted in a smaller moment introduced to the bi-stable plate. Finally, the moment was not sufficient to force the bi-stable plate to buckle and normal snap-through was experienced. One possible way to reduce this behaviour is to locally increase the bending stiffness of the pressure side of the flap in order to reduce the deflection and thus the moment introduced to the bi-stable plate.

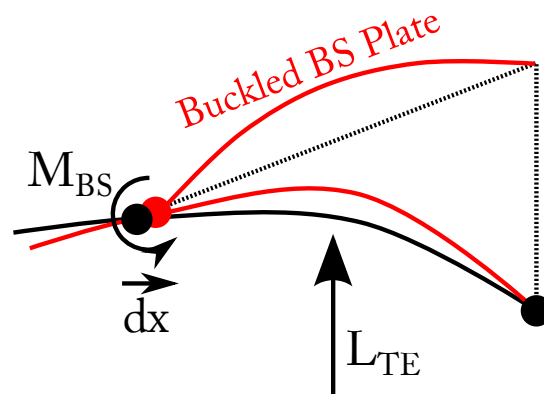


Figure 9.20: Buckling of bi-stable element due to TE geometry and stiffness.

9.3.4 Unsteady response of morphing flap

Although initially stated that dynamic effects are not taken into account in this project, the aerodynamic response of an instantaneous morphing trailing edge was deemed to be important to consider since a rapid airfoil shape change can induce significant unsteady loads.

Dr. García kindly provided a modified version of Q³UIC, called Q³UIC_AERO, which was specifically modified to simulate the aerodynamic response of a morphing flap. This time-dependent capability of Q³UIC_AERO presents a significant benefit for dynamic simulations compared to the steady solvers XFOIL and RFOIL.

A small and large flap were considered both for rated+gust as cutout+gust conditions. The AOA was selected based on the flow conditions during a gust at rated as well as at cutout wind speed, see Table 7.3 on page 42. Hence a value of 5.18° for the low AOA (cutout+gust) case and a value of 11.31° for the high AOA (rated+gust) case were used. The small and large flap presented in the previous Section were approximated with a rigid flap with a length of approximately 13% and 19% of the chord. The flap lengths are not exactly the same as those of the final flap designs since the trailing edge was specified from the discrete points which represent the airfoil profile. Based on the results presented in Figure 9.16 on page 78, a flap angle of 4° and 3° were selected for the small and large flap respectively.

Boundary layer transition was forced at 5% chord at the suction side and a Reynolds number of 5.5e6 was used for all cases.

The following results are presented for the sole purpose to get an impression of the dynamic lift response of an instantaneously morphing flap.

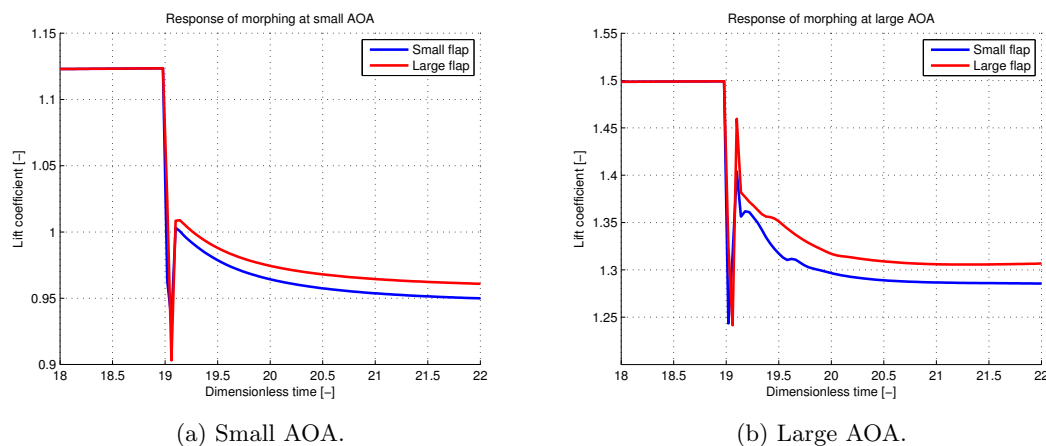


Figure 9.21: Lift response of morphing flap.

Figure 9.21 presents the time response of the lift coefficient of the reference airfoil with a morphing flap which deflects instantaneously. The response is expressed in function of a dimensionless time. The dimensional response can be obtained by dividing the dimensionless time by the relative velocity and multiplying with the chord length. Hence with a chord length of 1 m and a relative velocity of around 80 m/s, one dimensionless time unit can be related to approximately 12.5 ms.

It can be observed from Figure 9.21, that the instantaneous morphing of the trailing edge flap induces a sudden decrease in lift coefficient. After this sudden drop, the lift coefficient increases rapidly for a short while after which it decays to a constant value. The increase after the lift drop appears to be more significant for the large AOA case. This sudden drop, or undershoot,

is most likely the result of the morphing flap which exerts work on the flow and thereby lowers the lift coefficient for a small time.

It can be concluded that there is an unsteady response for a short while when the morphing occurs. The lift drops drastically after which it increases and then decays to a constant value. Since the lift values don't exceed their initial value, the unsteady response is deemed to be not detrimental for the structure when the absolute lift coefficient values are considered. However, the rapid change in lift coefficient could induce unwanted vibrations. Ideally, this aspect is addressed in more detail during further research.

Chapter 10

Conclusion

The main objective of this MSc thesis project was to investigate the load alleviation potential under extreme gusts of a variable stiffness bi-stable morphing blade section by designing such a blade section.

The following list presents the most important findings of this MSc thesis project;

- It was found that an EOG has a considerable impact on the loads generated by a wind turbine blade section. Especially at cutout conditions, the increase in loads as a result of an EOG was found to be substantial.
- A morphing mechanism was presented. This mechanism consists of a morphing trailing edge flap which is restrained from rotation by a bi-stable plate in the stiff state and allowed to rotate in the post-snap-through region. The flap hinge moment is the triggering parameter for snap-through and thus morphing and load alleviation.
- An EOG was found to induce an increase in flap hinge moment of 10% to 50% which indicates that there is a potential for a morphing flap which alleviates load upon reaching a threshold flap hinge moment.
- The effect of an EOG on the triggering parameter was mapped which allows for the selection of a suitable snap-through threshold flap hinge moment which is as low as possible and as high as necessary.
- The flap hinge moment behaviour for passive morphing was found to be more desirable for small flaps compared to large flaps.
- With a parametric study, it was found that small flaps are more efficient compared to large flaps in terms of lift reduction. Furthermore, it was found that the flap angle is dominant when lift reduction is considered. Moreover, it was found that a significant part of the load increase due to an EOG can be alleviated with trailing edge flaps.

- The impact of dynamic stall during an EOG was found to be significant at cutout conditions and negligible at rated conditions.
- Surface bonded PZT and MFC actuators were found to be most promising for restoring the bi-stable plate to its stiff state.
- A locally compressible profile skin was found to be required in order to achieve load alleviation. Therefore, a corrugated skin was implemented on the suction side near the trailing edge.
- It was found that the aerodynamic impact of a corrugated skin can be minimised by using recessed corrugation or by using a segmented skin.
- The presented flap designs show a small increase in lift before snap-through, an instantaneous reduction during snap-through and a further, gradual reduction after snap-through.
- At rated conditions, snap-through is triggered mostly by an increase in AOA whereas at cutout conditions, snap-through is triggered mostly by an increase in relative velocity. Furthermore, it was found that an EOG at rated conditions induces a larger flap hinge moment increase compared to an EOG at cutout conditions. Hence the triggering mechanism is more robust at rated conditions compared to cutout conditions since it is deemed less prone to exhibit unintended snap-through.
- The small flap features a higher flap deflection angle during snap-through compared to the large flap and both flaps exhibit relatively similar amounts of lift reduction. This originates from a more desirable flap hinge moment behaviour and indicates that small flaps have a better efficiency in terms of passive load alleviation.
- The bi-stable restraining mechanism was found to be very efficient since the flap experiences little resistance to rotation when the bi-stable plate is in the flexible state.
- The instantaneous lift reduction of the presented designs is around 7% at rated and 17% at cutout conditions. This indicates that load alleviation potential is higher at low AOA since flaps become less effective with increasing boundary layer separation. However, the amount of alleviated load increases after snap-through with increasing wind speed.
- A downward trailing edge deflection in the pre-snap-through region was found to originate from the layout of the flap and flexibility of the trailing edge pressure side skin.
- Similarly, bi-stable plate buckling was found to originate from moment introductions due the layout of the flap and flexibility of the trailing edge pressure side skin.
- Finally, the dynamic lift response upon morphing was found to show a short oscillation and a fast decline. This response was deemed not to be detrimental for the structure.

It can be concluded that passive load alleviation was achieved. One of the critical elements for this load alleviation was the implementation of a corrugated skin. One vital observation is that the triggering parameter behaves more desirable for passive morphing at high AOA whereas the effectiveness of trailing edge flaps is reduced at high AOA.

This project can be regarded as a step in the desirable direction starting from the work by Arrieta et al. [1] and Kuder et al. [2] since passive load alleviation was achieved. An indication of the load alleviation potential is given. However, the presented designs are not fully optimised

and further research is required to fully assess the load alleviation potential and establish a detailed design procedure of the presented morphing trailing edge flaps. Recommendations for further research are presented in Chapter 11.

Recommendations

Some recommendations for future research regarding the presented load alleviating morphing blade concept are listed here;

- Include a more realistic blade structure for simulations.
- Use a full blade model in the BEM code, this overcomes the assumption made in Section 7.5 which states that the power generated by an outboard blade section is linearly dependent on the total power output.
- Adopt an unsteady BEM code which takes dynamic stall into account.
- Validate the aeroelastic model with wind tunnel tests. Ensure that the clamped part of the airfoil in the simulation is sufficiently stiff so it does not deform significantly in the wind tunnel.
- Validate the dynamic response of an instantaneously morphing flap with wind tunnel tests.
- Investigate the aerodynamic impact of corrugated skins with wind tunnel tests.
- Optimize the trailing edge flap design for maximal flap angle in order to alleviate more load.
- With more design freedom, design a blade section which alleviates load at specified conditions.

References

- [1] Andres F. Arrieta, Izabela K. Kuder, Mathias Rist, Tobias Waeber, and Paolo Ermanni. Passive load alleviation aerofoil concept with variable stiffness multi-stable composites. *Composite Structures*, 116:235–241, 2014.
- [2] Izabela K. Kuder, Andres F. Arrieta, Mathias Rist, and Paolo Ermanni. Static design of a selective compliance morphing wing profile based on integrated variable stiffness bi-stable components. In *ASME 2014 Smart Materials, Adaptive Structures and Intelligent Systems*. ASME, 2014.
- [3] L.F. Campanile. *Adaptive structures: Engineering applications*. Wiley, 2007.
- [4] Stephen Daynes, Paul. M. Weaver, and K.D. Potter. Aeroelastic Study of Bistable Composite Airfoils. *Journal of Aircraft*, 46(6):2169–2174, 2009.
- [5] Nando W. A. Timmer and Ruud van Rooij. AIAA-2003-0352 Summary of the Delft University Wind Turbine Dedicated Airfoils. *ASME*, 2003.
- [6] Franck Bertagnolio, Niels N. Sørensen, and Jeppe Johansen. Profile Catalogue for Airfoil Sections Based on 3D Computations. Technical report, RisøNational Laboratory, December 2006.
- [7] Siemens AG. Siemens D6 platform 6.0-MW direct drive wind turbine. Online, 2014. Accessed December 2014.
- [8] Martin O.L. Hansen. 46300 Wind Turbine Technology and Aerodynamics, 2012. DTU MSc course.
- [9] Knowledge Centre WMC. *LR-AE4645 Focus6 Workshop - Structural blade design day 1*, 01 edition, March 2011. Report no.: WMC-2011-27.
- [10] Lawrence W. Carr, Kenneth W. Mc Alister, and William J. McCroskey. Analysis of the development of dynamic stall based on oscillating airfoil experiments. NASA Technical Note D-8382, National Aeronautics and Space Administration, January 1977.
- [11] Michael Christian Winkler. *Analysis of Corrugated Laminates*. PhD thesis, ETH Zurich, 2012.

- 90
- References
- [12] C. Thill, J. A. Etches, I. P. Bond, K. D. Potter, and P. M. Weaver. Composite structures for morphing wing skin applications. *Smart Materials and Structures*, 19(12), November 2010.
- [13] Mark Drela. XFOIL: An Analysis and Design System for Low Reynolds Number Airfoils. *MIT Dept. of Aeronautics and Astronautics, Cambridge, Massachusetts*, 1989.
- [14] Néstor Ramos García, Wen Zhong Shen, and Jens Nørkær Sørensen. A strong viscous-inviscid interaction model for rotating airfoils. *Wind Energy*, 17(12):1957–1984, October 2013.
- [15] R.P.J.O.M. van Rooij. Modification of the boundary layer calculation in RFOIL for improved airfoil stall prediction. Technical Report Rapport IW-96087R, TU Delft, 1996.
- [16] Xavier Lachenal, Stephen Daynes, and Paul M. Weaver. Review of morphing concepts and materials for wind turbine blade applications. *Wind Energy*, 16:283–307, February 2012.
- [17] Marc R. Schultz and Michael W. Hyer. A morphing concept based on unsymmetric composite laminates and piezoceramic MFC actuators. *Collection of Technical Papers - AIAA/ASME/ASCE/AHS/ASC Structures, Structural Dynamics and Materials Conference*, 4:3192–3204, 2004.
- [18] Silvestro Barbarino, Onur Bilgen, Rafic M. Ajaja, Michael I. Friswell, and Daniel J. Inman. A Review of Morphing Aircraft. *Journal of Intelligent Material Systems and Structures*, 22:823–877, June 2011.
- [19] C. Thill, J. Etches, K. Potter, and P. Weaver. Morphing Skins. *Aeronautical Journal*, 112(1129):117–139, March 2008.
- [20] Silvestro Barbarino, R. Pecora, L. Lecce, A. Concilio, S. Ameduri, and E. Calvi. A Novel SMA-based Concept for Airfoil Structural Morphing. *Journal of Materials Engineering and Performance*, 18(5-6):696–705, August 2009.
- [21] Stephen Daynes, S.J. Nall, Paul M. Weaver, K.D. Potter, P. Margaritis, and P.H. Mellor. On a bistable flap for an airfoil. *Collection of Technical Papers - AIAA/ASME/ASCE/AHS/ASC Structures, Structural Dynamics and Materials Conference*, pages 2009–2103, 2009.
- [22] S. Kota, J. Hetrick, R. Osborn, D. Paul, E. Pendleton, P. Flick, and C. Tilmann. Design and application of compliant mechanisms for morphing aircraft structures. *SMART STRUCTURES AND MATERIALS 2003: INDUSTRIAL AND COMMERCIAL APPLICATIONS OF SMART STRUCTURES TECHNOLOGIES*, 5054:24–33, 2003.
- [23] Onur Bilgen, Andres F. Arrieta, Michael I. Friswell, and Peter Hagedorn. Dynamic control of a bistable wing under aerodynamic loading. *Smart Materials and Structures*, 22(2):1–15, January 2013.
- [24] Andres F. Arrieta, Peter Hagedorn, Onur Bilgen, and Michael I. Friswell. Passive load alleviation bi-stable morphing concept. *AIP Advances*, 2(3):–, 2012.
- [25] NASA. RELEASE 14-308, NASA Tests Revolutionary Shape Changing Aircraft Flap for the First Time. Online, November 2014.

- [26] Wolfram Raither, Emian Furger, Manuel Zündel, Andrea Bergamini, and Paolo Ermanni. Variable-stiffness skin concept for camber-morphing airfoils. *Journal of Intelligent Material Systems and Structures*, 2014. Special Issue Article.
- [27] I. Kade Wiratama. *Aerodynamic Design of Wind Turbine Blades Utilising Nonconventional Control Systems*. PhD thesis, Northumbria University, November 2012.
- [28] Peter B. Andersen. Load Alleviation on Wind Turbine Blades using Variable Airfoil Geometry (2D and 3D study). Master’s thesis, Technical University of Denmark, June 2005.
- [29] Damien Castaignet, Thanasis K. Barlas, Thomas Buhl, Niels K. Poulsen, Jens Jakob Wedel-Heinen, Niels A. Olesen, Christian Bak, and Kim Taeseong. Full-scale test of trailing edge flaps on a Vestas V27 wind turbine: active load reduction and system identification. *Wind Energy*, 17(4):549–564, 2014.
- [30] C. L. Bottasso, F. Campagnolo, A. Croce, and C. Tibaldi. Optimization-based study of bend-twist coupled rotor blades for passive and integrated passive/active load alleviation. *Wind Energy*, 16(8):1149–1166, 2013.
- [31] Benjamin Lambie. *Aeroelastic Investigation of a Wind Turbine Airfoil with Self-Adaptive Camber*. PhD thesis, Technischen Universität Darmstadt, 2011.
- [32] Michael Selig, Eric Loth, and Patrick Moriarty. Morphing segmented wind turbine concept. *28th AIAA Applied Aerodynamics Conference*, 2010.
- [33] Cezar G. Diaconu, Paul M. Weaver, and Filippo Mattioni. Concepts for morphing airfoil sections using bi-stable laminated composite structures. *Thin-Walled Structures*, 46(6):689–701, 2008.
- [34] Dassault Systèmes. Abaqus FEA.
- [35] Python Software Foundation. Python.
- [36] Wei Jun Zhu, Wen Zhong Shen, and Jens Nørkær Sørensen. Integrated airfoil and blade design method for large wind turbines. *Renewable Energy*, 70:172–183, 2014.
- [37] Martin O.L. Hansen. *Aerodynamics of Wind Turbines*. Earthscan, 2nd edition, 2008.
- [38] MathWorks. MATLAB.
- [39] Leonardo Bergami. *Adaptive Trailing Edge Flaps for Active Load Alleviation in a Smart Rotor Configuration*. PhD thesis, Technical University of Denmark, August 2013.
- [40] T. Wolff, B. Ernst, and J. R. Seume. Aerodynamic behavior of an airfoil with morphing trailing edge for wind turbine applications. *Journal of Physics: Conference Series*, 524(1):012018, 2014.
- [41] Ruud van Rooij and Nando W. A. Timmer. Design of Airfoils for Wind Turbine Blades. Presentation, May 2004.
- [42] J. Jonkman, S. Butterfield, W. Musial, and G. Scott. Definition of a 5-MW Reference Wind Turbine for Offshore System Development. Technical Report NREL/TP-500-38060, National Renewable Energy Laboratory, February 2009.

- [43] F. Grasso and O. Ceyhan. Usage of advanced thick airfoils for the outer part of very large offshore turbines. *Journal of Physics: Conference Series*, 524(1):012030, 2014.
- [44] Niels Troldborg. Computational study of the Risø-B1-18 airfoil with a hinged flap providing variable trailing edge geometry. *Wind Engineering*, 29(2):89–113, 2005.
- [45] Peter Hauge Madsen, Morten Hartvig Hansen, and Niels Leergaard Pedersen. DTU International Energy Report 2014 Wind energy Chapter 6. Technical report, Technical University of Denmark, November 2014.
- [46] Nando W. A. Timmer. DU 93 W-210 airfoil measurements. Unpublished.
- [47] E. Llorente, A. Gorostidi, M. Jacobs, Nando W. A. Timmer, X. Munduate, and O. Pires. Wind Tunnel Tests of Wind Turbine Airfoils at High Reynolds Numbers. *Journal of Physics: Conference Series*, 524(1):012012, 2014.
- [48] Joseph Katz and Allen Plotkin. *Low-speed aerodynamics*. Cambridge aerospace series. Cambridge University Press, 2nd edition, 2001.
- [49] Siemens AG. Wind Turbine SWT-6.0-154. Online. Accessed December 2014.
- [50] Green Investment Bank. In pictures: The construction of Westernmost Rough. Online, March 2014. Accessed December 2014.
- [51] DANSK STANDARD. Wind turbines - Part 1: Design requirements, August 2006.
- [52] Wikipedia.org. Viscosity. Online. Accessed February 2015.
- [53] Doug McLean. *Understanding aerodynamics: arguing from the real physics*. John Wiley & Sons, Ltd., 2013.
- [54] Wikipedia.org. Mach number. Online. Accessed February 2015.
- [55] Tony Burton, Nick Jenkins, David Sharpe, and Ervin Bossanyi. *Wind Energy Handbook*. John Wiley & Sons, Ltd., 2nd edition, 2011.
- [56] Morten Hartvig Hansen, Mac Gaunnaa, and Helge Aagaard Madsen. A Beddoes-Leishman type dynamic stall model in state-space and indicial formulations. Technical Report Risø-R-1354(EN), Risø National Laboratory, Roskilde, Denmark, 2004.
- [57] J. A. Etches, K. D. Potter, P. M. Weaver, I. P. Bond, and C. Thill. Composite corrugated structures for morphing wing skin applications. *Smart Materials and Structures*, 19(12):10, November 2010.
- [58] Gerald Kress. Mechanics of Composite Materials, November 2014. ETH Zürich MSc course.
- [59] Isaac M. Daniel and Ori Ishai. *Engineering mechanics of composite materials*. Oxford University Press, Inc., 2006.
- [60] Yuying Xia, Onur Bilgen, and Michael I. Friswell. The effect of corrugated skins on aerodynamic performance. *Journal of Intelligent Material Systems and Structures*, 25(7):786–794, 2014.
- [61] John. D. Anderson. *Fundamentals of Aerodynamics*. McGraw-Hill, 2001.

- [62] Néstor Ramos García. *Unsteady Viscous-Inviscid Interaction Technique for Wind Turbine Airfoils*. PhD thesis, Technical University of Denmark, April 2011. DCAMM Special Report no. S127.

Appendix A

Reference airfoil coordinates

The coordinates of the reference, DU-93-W-210 airfoil are given in Table A.1. These coordinates were kindly provided by Timmer [46]. Please note that the trailing edge is open when these coordinates are plotted.

96		Reference airfoil coordinates					
X	Y	X	Y	X	Y	X	Y
100	0.2502	38.071297	12.4608	0.0138	-0.2577	42.523102	-7.8975
99.453995	0.4239	36.900799	12.4659	0.0491	-0.4675	43.733299	-7.741
98.765396	0.6252	35.732498	12.4537	0.1072	-0.6777	44.9445	-7.5707
97.8881	0.8702	34.562901	12.4243	0.1876	-0.8887	46.1562	-7.3868
96.832001	1.1579	33.392502	12.3779	0.2908	-1.1007	47.373001	-7.1885
95.649803	1.4729	32.2187	12.3147	0.4192	-1.3137	48.5966	-6.9765
94.395294	1.8019	31.046501	12.2351	0.5749	-1.5295	49.822502	-6.7521
93.106499	2.1353	29.8755	12.139	0.7607	-1.7499	51.055401	-6.5144
91.796097	2.471	28.7076	12.026401	0.9803	-1.9785	52.296196	-6.2643
90.477798	2.8065	27.539501	11.8969	1.2381	-2.2185	53.544201	-6.0024
89.1576	3.1397	26.3736	11.7511	1.5402	-2.4733	54.799198	-5.7297
87.830101	3.4722	25.210199	11.5888	1.8923	-2.7448	56.061501	-5.4464
86.498199	3.8043	24.051498	11.410501	2.2998	-3.0327	57.332497	-5.1532
85.164299	4.1354	22.8964	11.2156	2.7672	-3.334	58.6115	-4.8509
83.832504	4.4648	21.745399	11.0044	3.299	-3.646	59.9002	-4.5399
82.505104	4.7909	20.601501	10.7774	3.8986	-3.9653	61.200203	-4.2209
81.177101	5.1152	19.464401	10.5342	4.5697	-4.2901	62.512501	-3.8947
79.854797	5.4354	18.3361	10.2751	5.3124	-4.6179	63.8367	-3.5631
78.5298	5.7535	17.216801	9.9998	6.1251	-4.9459	65.164001	-3.2297
77.207497	6.0685	16.1092	9.709	7.0026	-5.2714	66.4804	-2.9006
75.887802	6.3798	15.015	9.4025	7.9352	-5.5905	67.7827	-2.5785
74.567101	6.6879	13.9347	9.080299	8.9144	-5.9003	69.067696	-2.2656
73.243103	6.9936	12.871901	8.7429	9.927199	-6.1971	70.334	-1.9642
71.916595	7.2974	11.8278	8.3903	10.965301	-6.4784	71.585999	-1.6745
70.591599	7.5982	10.8049	8.023	12.0242	-6.7429	72.818604	-1.3991
69.272202	7.8948	9.8069	7.6417	13.102099	-6.9906	74.036201	-1.1386
67.957001	8.186601	8.8363	7.247	14.196099	-7.2214	75.240204	-0.8935
66.6455	8.4734	7.8978	6.8404	15.3035	-7.4349	76.425598	-0.6661
65.3358	8.7554	6.9954	6.4233	16.423801	-7.6314	77.600502	-0.4563
64.030197	9.0319	6.1344	5.998	17.554399	-7.811	78.763199	-0.2646
62.7328	9.3015	5.3215	5.5683	18.6919	-7.9732	79.916	-0.0917
61.440598	9.5637	4.5642	5.1388	19.839201	-8.1182	81.0606	0.062
60.152401	9.818501	3.8681	4.7147	20.996901	-8.2471	82.201996	0.197
58.869499	10.0652	3.2412	4.3039	22.1605	-8.3594	83.337898	0.3129
57.5886	10.304	2.6881	3.9144	23.3318	-8.4555	84.469902	0.4094
56.314098	10.533999	2.2114	3.5528	24.508301	-8.5359	85.597801	0.4864
55.0471	10.754	1.8068	3.2186	25.686401	-8.6	86.721298	0.5436
53.783901	10.9641	1.4637	2.906	26.868999	-8.6479	87.842201	0.5807
52.5275	11.1637	1.1719	2.6104	28.0557	-8.68	88.962105	0.5979
51.279598	11.3517	0.9234	2.3292	29.245701	-8.6966	90.078094	0.5952
50.043499	11.527	0.7124	2.0608	30.436998	-8.6975	91.193596	0.5717
48.819199	11.6883	0.5342	1.8029	31.632	-8.6828	92.314301	0.5279
47.604298	11.8352	0.3855	1.5546	32.8312	-8.652801	93.439796	0.4641
46.3969	11.9672	0.2649	1.313	34.0354	-8.6076	94.571297	0.381
45.192902	12.0843	0.1715	1.0757	35.245201	-8.547999	95.6978	0.2812
43.992199	12.186601	0.1034	0.8409	36.4557	-8.4741	96.793098	0.1684
42.797398	12.2738	0.0559	0.609	37.670002	-8.386001	97.8116	0.05
41.609497	12.3448	0.0237	0.3822	38.8853	-8.284101	98.699699	-0.0643
40.423798	12.3999	0.0047	0.1628	40.100399	-8.1687	99.426102	-0.1658
39.244602	12.4388	0.0005	-0.0488	41.312901	-8.0399	100	-0.2498

Table A.1: DU-93-W-210 airfoil coordinates.